Deliverable 3.3: Report on the baseband design, D-band antenna designs and metasurfaces

Editor:	Aris Tsolis, NCSRD Antonis Alexandridis, NCSRD	
Deliverable nature:	Document, report (R)	
Dissemination level:	Public (PU)	
Date: planned | actual	30 April 2022	30 May 2022
Version | No. of pages	1.0	115
Keywords:	D-band radios, directional links, cross-polarization interference cancellation, feed horn antennas, reflector antennas, dielectric lens antennas , reflectarray antennas, metasurfaces	

Abstract

This deliverable summarizes the research on D-band radio concepts of ARIADNE, as an output of the first 30 months of work in Tasks 3.1 - 3.4.

Deliverable D3.3 reinforces, generalizes and expands the results of the research activities conducted and settled as plan in Deliverable D3.1 on “Report on baseband and antenna concepts” and Deliverable D3.2 “Report on simulations of first RFIC implementations”. In this direction the present deliverable focuses on baseband design and prototypes, on antennas design and prototypes for short and long range scenarios (outdoor and indoor) and on metasurfaces/RIS design and manufacture to assist mainly indoor communications.

Coordinator of this deliverable is NCSRD. Technical contributors are all partners of the work package. The technical quality is assured by the technical management UPRC Prof. Angela Alexiou, the WP Leader IAF and the Task Leaders ICOM (Task 3.1), IAF (Task 3.2), NCSRD (Task 3.3), and AALTO (Task 3.4).

Disclaimer

This project has received funding from the European Union's Horizon 2020 research and innovation programme under grant agreement No 871464. This publication reflects only the author's view and the European Commission is not responsible for any use that may be made of the information it contains.

Impressum

Full project title: Artificial Intelligence Aided D-band Network for 5G Long Term Evolution

Short project title: ARIADNE

Number and title of work-package: WP3 - Energy-efficient D-band radio concepts

Number and title of task(s): Task 3.1, 3.3, and 3.4

Document title: Report on baseband and antenna concepts

Editors: Aris Tsolis, Antonis Alexandridis, NCSRD

Work-package leader: IAF

Executive summary

Deliverable D3.3 reinforces, generalizes and expands the research activities conducted in Deliverable 3.1 (“Report on baseband and antenna concepts”) and Deliverable 3.2 (“Report on simulations of first RFIC implementations”). In this context, the present deliverable focusses on the design of baseband and antennas, spectrally efficient and reliable D-band radio prototypes for short and long-range scenarios (from 100 m to more than 1000 m), and metasurfaces/RIS including their fabrication for the demonstrators in WP5.

The deliverable consists of three main technical chapters, which contributions are summarized as follows.

In Chapter 2, we have presented the baseband unit and the DAC/ADC boards supporting the PtP LOS demonstrator. This work investigated how the baseband receiver can be capable of mitigating the D-band specific depolarization effects through a specific designed and developed XPIC architecture. This was supported by experimental back-to-back tests of the BBU. Additionally, the practical implementation of frequency-switching at D-band has been discussed with respect to the generation of the carrier signal and the needed reference oscillators’ signal, e.g., for exploiting frequency diversity to enhance the reliability or security at the physical layer. Hardware prototypes were designed that test the functions that will be needed in the outdoor unit demonstrator.

In Chapter 3, firstly, we present in detail the design of the reflector HGAs (high gain antennas) appropriate for the outdoor long range scenario. Various horn antenna feeders have been designed. Next, the optimization of HGAs and detailed realistic designs have been presented that result in a model of a practically relevant antenna. Additionally, designs of lens MGAs (medium gain antennas), appropriate for an indoor scenario which includes NLOS propagation through RIS reflection, have been presented. Sensitivity of the antenna performance on the dielectric properties of the lens material has been conducted as well. Lastly, a confocal antenna has been fabricated as a proof-of-concept of the liquid crystal reflectarray antenna in the W-band. The optics of the antenna have been experimentally verified in an anechoic chamber using a passive sub-reflector as a calibration standard instead of the liquid crystal technology. Next, the reconfigurable reflectarray antenna using liquid crystal dielectric materials has been experimentally characterized, by testing the voltage dependence of the phase, which was extracted in a quasi-optical lab bench system. Different approaches of implementing the reflectarray element has been examined and compared. Finally, a novel dynamical model of LC transitions for different excitations beyond the known approximations has been proposed and validated.

In Chapter 4, firstly, we present the development of a design and implementation procedure for anomalous reflectors suitable for the planned indoor demonstration scenario. The design of anomalous reflectors for RIS has been proposed. We have considered different designs and discussed their benefits in view of various manufacturing challenges, from which we have derived an optimum way for manufacturing of this type of RIS. Secondly, we analyzed the performance of communications in the near field of a large phased array antenna. We further analysed the impact of the user position uncertainty on the link performance. Two beamsteering methods were compared, the Linear Phase Beam Steering (LPBS) and the Near Field Focusing (NFF) method. This comparison showed that the optimal beamforming method is dependent on the accuracy of the position information, and our analysis helps to select the appropriate beam-steering method for a given scenario.

List of authors

Organization/Company	Author	Contribution
NCRSD	Aris Tsolis	Editing of D3.3, writing 3.1, 3.2
NCSRD	Antonis Alexandridis	Editing of D3.3, writing 3.1, 3.2
NCSRD	Stefanos Lampiris	Writing 3.1, 3.2
NCSRD	Vasileios Vlachodimitropoulos	Writing 3.1, 3.2
ICOM	Evangelos Pikasis	Writing 2.2
IAF	Thomas Merkle	Editing of D3.3
IAF	Joachim Hoppe	Writing 2.1
UPM	Eduardo Carrasco	Writing 3.4
UPM	Robert Guirado	Writing 3.4
UPM	Gerardo Pérez-Palomino	Writing 3.4
Aalto	Sergei Kosulnikov	Writing 4.1
Aalto	Xuchen Wang	Writing 4.1
Aalto	Sergei Tretyakov	Writing 4.1
UOULU	Dinesh Acharya	Writing 4.2
UOULU	Joonas Kokkoniemi	Writing 4.2
UOULU	Markus Berg	Writing 4.2

Table of Contents

List of figures and tables

List of figures:

List of tables:

Abbreviations

A list of abbreviations is strongly recommended

2D	Two dimensional
3D	Three dimensional
5G	Fifth Generation mobile/cellular networks
A/D	Analog to Digital
AI	Artificial Intelligence
BBU	Baseband Unit
BER	Bit Error Rate
CFO	Carrier Frequency Offset
Co	Co-Polar Component
CP	Circular Polarization
Cx	Cross-Polar Component
D/A	Digital to Analog
DAC/ADC	Digital to Analog Converter / Analog to Digital Converter
DDS	Direct Digital Synthesis
DDS	Direct Digital Synthesis
DSP	Digital Signal Processing
EM	Electromagnetic
ET	Edge Taper
FF	Far Field
FPGA	Field Programmable Gate Arrays
FT	Feed Taper
GND	Ground
HGA	High Gain Antenna
I/Q	in-phase and quadrature
IRS	Intelligent Reflective Surface
LC	Liquid Crystal
LOS	Line Of Sight
LPBS	Linear Phase-shift beam steering

MGA	Medium Gain Antenna
NF	Near Field
NFF	Near Field Focusing
NLOS	Non-Line Of Sight
PC	Personal Computer
PCB	Printed Circuit Board
PDF	Probability density function
PEC	Perfect Electrical Conductor
PLL	Phased-Locked Loop
PtP	Point to Point
QAM	Quadrature amplitude modulation
RA	Reflectarray
RF	Radio Frequency
RFIC	Radio Frequency Integrated Circuit
RIS	Reconfigurable Intelligent Surfaces
RMS	Root Mean Square
Rx	Receiver
SLL	Side Lobe Level
SMA	Sub Miniature version A
SNR	Signal to Noise Ratio
SPI	Serial Peripheral Interface
Tx	Transmitter
UART	Universal Asynchronous Receiver/Transmitter
USB	Universal Serial Bus
VCO	Voltage Control Oscillator
WP	Work Package
XPI	cross-polarization interference
XPIC	Cross Polarization Interference Cancelling Technology
X-pol	Cross Polar

1 Introduction

The main objective of this deliverable is to report the research work of WP3 (designs and prototypes) on the key components of the baseband and radio front-end, D-band antennas and metasurfaces, as a continuation of work defined by deliverables D3.1 "Report on baseband and antenna concepts" and D3.2 "Report on simulations of first RFIC implementations" and as input to WP5 for the demonstration scenarios defined in deliverable D5.1 "Report on the demonstration scenarios and description of testbed implementation plan".

Moreover, apart from the input to demonstration tasks in WP5, this deliverable has targeted to satisfy the following objectives to evolve the research in the technical areas:

- Develop advanced real-time DSP algorithms for correction of the RF impairments induced by the RF front and increased spectral efficiency through polarization multiplexing. More specifically, the development of effective baseband designs and prototypes to efficiently receive and transmit signals at different sub-bands at D-band by developing a baseband unit, which is able to mitigate the D-band specific depolarization effects through a specific designed XPIC architecture.
- Implement broadband high-speed transceivers and explore the integration with CMOS control functions. Focusing on investigation of the practical implementation of frequency-switching at D-band with respect to the generation of the carrier signal and the needed reference oscillators' signal, for exploiting frequency diversity to achieve reliable and/or secure transmission at the physical layer.
- Explore concepts, design and test prototypes for novel low profile high gain D-band antenna solutions, which incorporate beamsteering capabilities. Focus on design of HGA (high gain reflector antennas) effective in terms of gain and X-pol performance with compact size. Use of dielectric lens antennas technology to achieve beam steering of MGAs (medium gain antennas) appropriate for indoor communications (LOS/NLOS) or feeding HGAs.
- Investigate static and reconfigurable reflect-array solutions and develop prototype solutions. More specifically, design of liquid crystal material based reflectarrays capable of beam steering by control of a voltage across the individual liquid crystal array elements
- Design, manufacture and characterize metasurface concepts for D-band frequencies that transforms pico-cell networks into adaptive, reconfigurable, sensing environments. Focus on development of effective and frequency selective RIS for indoor NLOS links. Consider propagation aspects of extremely large antenna arrays from theoretical viewpoint and, especially, concentrate on the near field behavior. Focus on the investigation of the effect of a user position uncertainty on the communication link performance, when physically positioned in the near field of a large phased array (similar to metasurfaces).

2 Baseband design and prototypes

2.1 Baseband unit design

This section presents the main building blocks for the generation of the baseband signals that will be used in the PtP LOS demonstrator. These baseband sub-systems consist of the baseband unit (BBU) with the FPGA-based modem and the digital-to-analog (D/A) and analog-to-digital (A/D) converters board as depicted in the simplified block diagram of Figure 1.

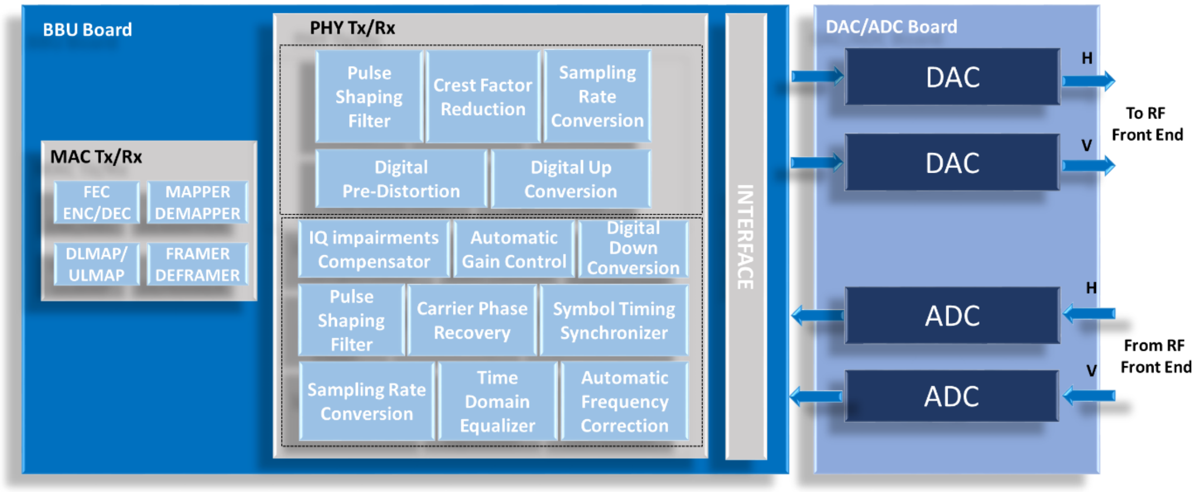

Figure 1: The basic baseband components (BBU & DAC/ADC modules)

In the following subsections, we report on the designs and functionalities of the different sub-systems in more detail.

2.1.1 Description of Baseband unit – Prototypes

The block diagram of the BBU is depicted in the left part of the block diagram of Figure 1. A dedicated FPGA board has been utilized to support the demanding digital signal processing (DSP) algorithms. Based on the existing know-how and already implemented techniques, ICOM has evolved its DSP methods (related to impairment cancellation as phase noise, carrier frequency offset, non-linearities) to combat the anticipated D-Band specific impairments induced by the RF Front end. In addition, this baseband unit offers increased spectral efficiency through the use of the polarization multiplexing technique. Towards this end, the receiver part of the baseband module was designed so that it would be capable of mitigating the depolarization effects in D-Band through the developed XPIC architecture [1]. The implemented BBU board inside its housing is depicted in Figure 2.

Figure 2: Baseband unit inside its housing

2.1.2 Description of DAC/ADC board - Prototypes

ICOM designed and implemented the board with the required DA/AD converters to generate/acquire the in-phase and quadrature (I-Q) data streams, satisfying the requirements of the polarization multiplexing technique for the PtP LOS demonstrator. This board hosts two DAC and two ADC modules supporting the two transmit (Tx) and the two receive (Rx) parts of the modems as depicted in Figure 1. The implemented DAC/ADC board can be seen in Figure 3, in which eight SubMiniature version A (SMA) type connectors are used, corresponding to the in-phase and quadrature (I/Q) paths of each DAC (or ADC), which are fed separately to (or by) the specific D-Band frontend.

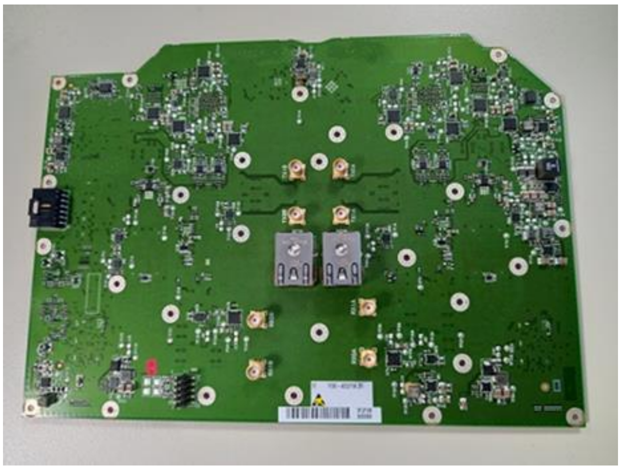

Figure 3: DA/AD converters board

The DA/AD converter board is interconnected with the BBU via high-speed digital interfaces.

Table 1 summarizes the main parameters of the converter board.

Table 1: Main parameters of the converter board

Parameter	Value
DAC resolution	12-bit
ADC resolution	12-bit
Sampling rate	2.5 Gsps
Input/Output Z_0	50 ohm

2.1.3 Digital loopback results

After completion of the baseband unit development process, the necessary hardware checks were followed and the system was tested in a digital loopback mode, verifying the DSP design functionality. In the case of the digital loopback, the transmit path of each modem (Modem-1 & Modem-2) is connected to the corresponding receive path on the PCB board. The achievable signal-to-noise ratio (SNR) at the receiver part of each modem had a value of about 58 dB. It should be pointed out that in a digital loopback process, there is no kind of impairments originating from analogue components that can affect the signal in the time and/or in the frequency domain.

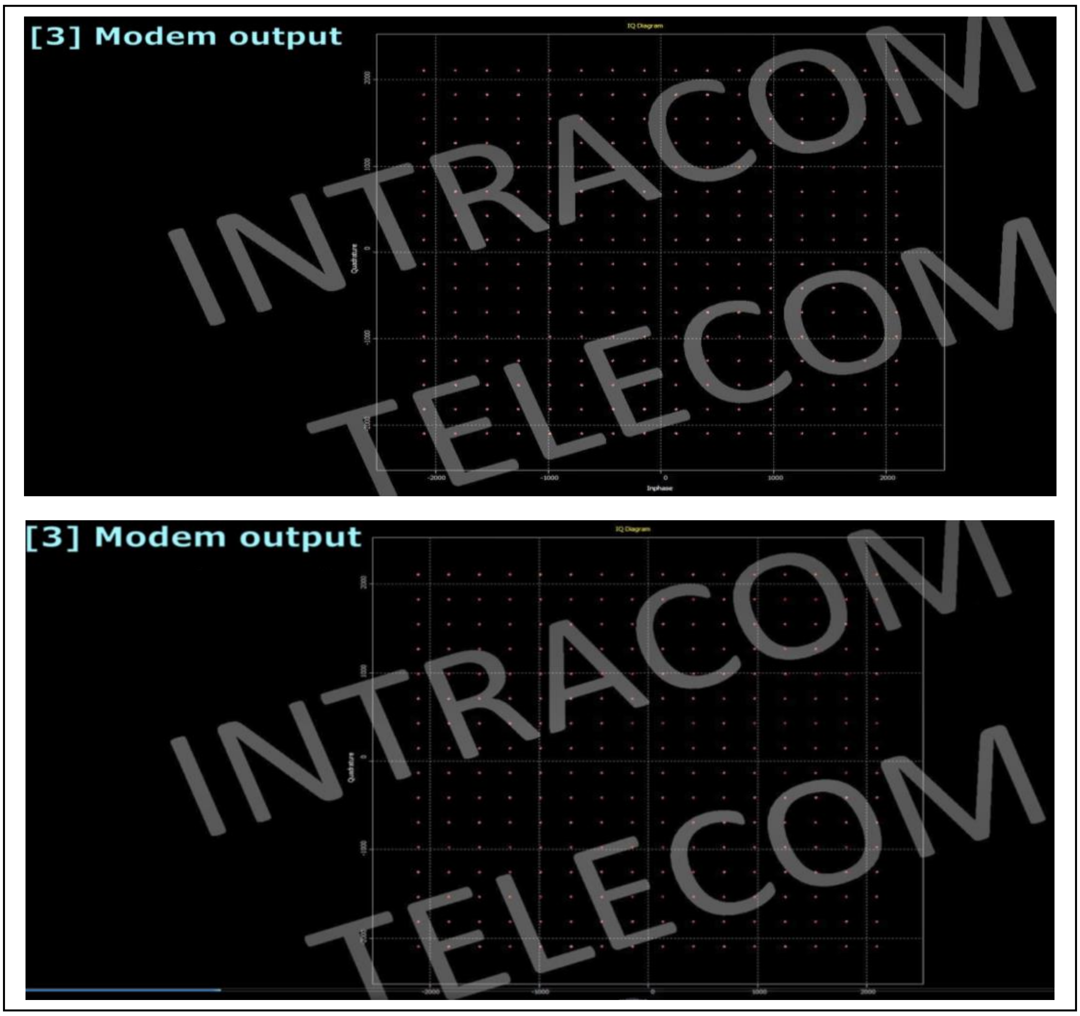

Figure 4: Constellation diagrams at the output of the two modems

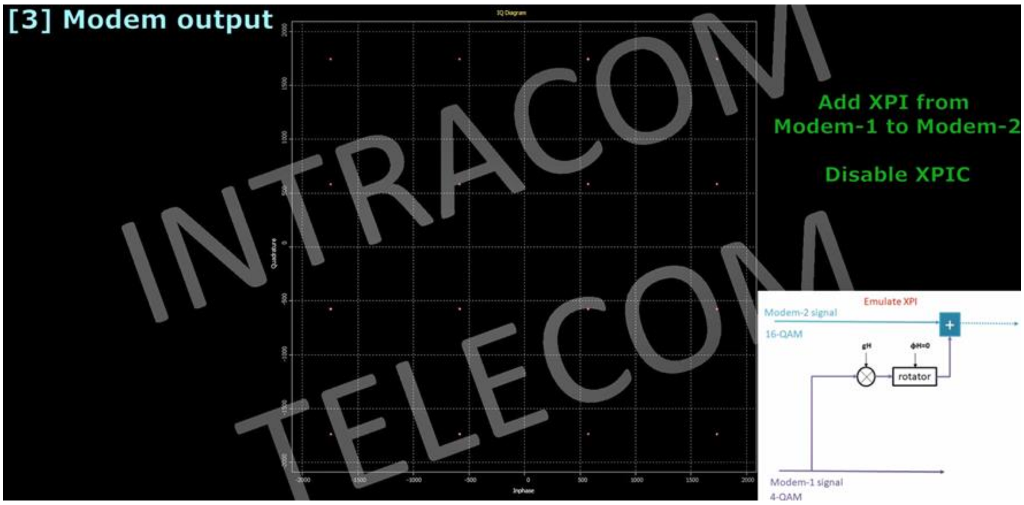

Figure 5: Constellation diagram at the output of the Modem without XPI
and the block diagram of XPI emulation

In Figure 4, the constellation diagrams at the output of the two modems in digital loopback mode for the case of 256 QAM are depicted. To emulate the cross-polarization interference (XPI), I/Q data from Modem-1 were added to Modem-2 I/Q streams with some attenuation and phase shift rotation [1] .

The QAM constellation size of Modem-1 and Modem-2 was 4-QAM and 16-QAM respectively. Initially, the phase rotation DSP block was disabled and its control phase had a value of zero. Figure 5 shows the constellation diagram at the Modem-2 output and the block diagram of the XPI emulation. Figure 6 shows the influence of XPI on the constellation diagram of QAM symbols at the Modem-2 output, in which the “superposition” of attenuated 4-QAM symbols of Modem-1 with the 16-QAM symbols of Modem-2 is depicted.

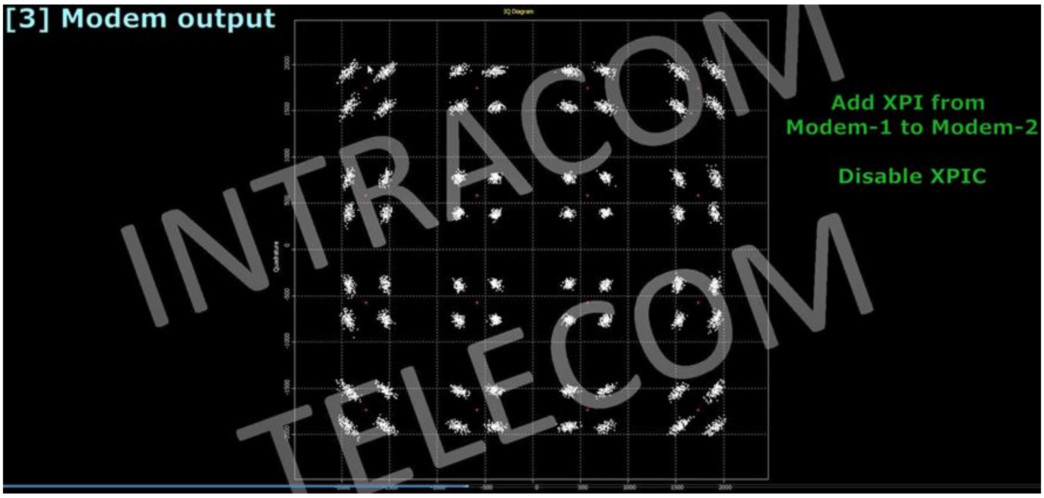

Figure 6: Influence on constellation diagram of cross-polarization interference from Modem-1 to Modem-2

Next, the XPIC algorithm [1], which cancels the cross-polarization interference, was enabled and corrected the distorted QAM symbols. The constellation diagram of these XPIC recovered QAM symbols is illustrated in Figure 7 and as can be seen, ICOM’s DSP-enhanced BBU could restore the QAM symbols with high reliability.

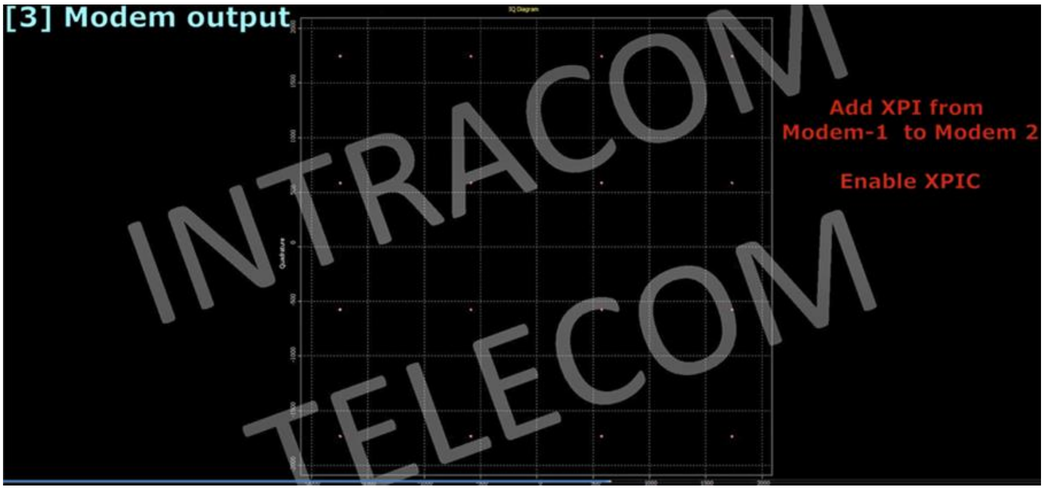

Figure 7: Constellation of corrected QAM symbols with XPIC algorithm

Following, the measurements were repeated enabling the phase rotator of XPI emulation with a nonzero phase, disabling the phase rotation-correction module at XPIC algorithm at the receiver side as described in [1]. In parallel, a carrier frequency offset (CFO) between the two modems was introduced. As a result, the QAM symbols at the output of Modem-2 were not recovered and their constellation diagram is presented in Figure 8. By enabling the XPIC phase rotator block and after the CFO correction, the QAM symbols were recovered as can be seen in Figure 9.

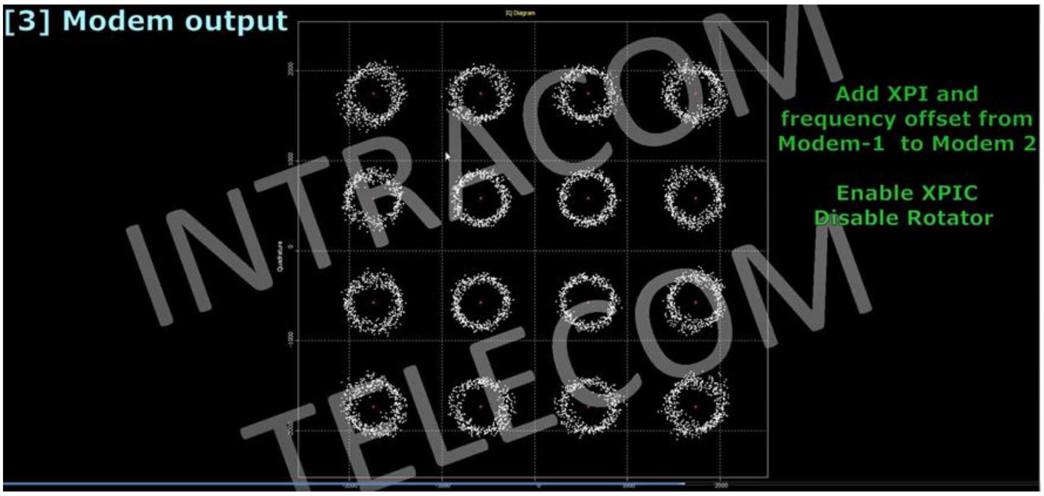

Figure 8: Constellation diagram of uncorrected QAM symbols using XPIC algorithm disabling its phase rotator block

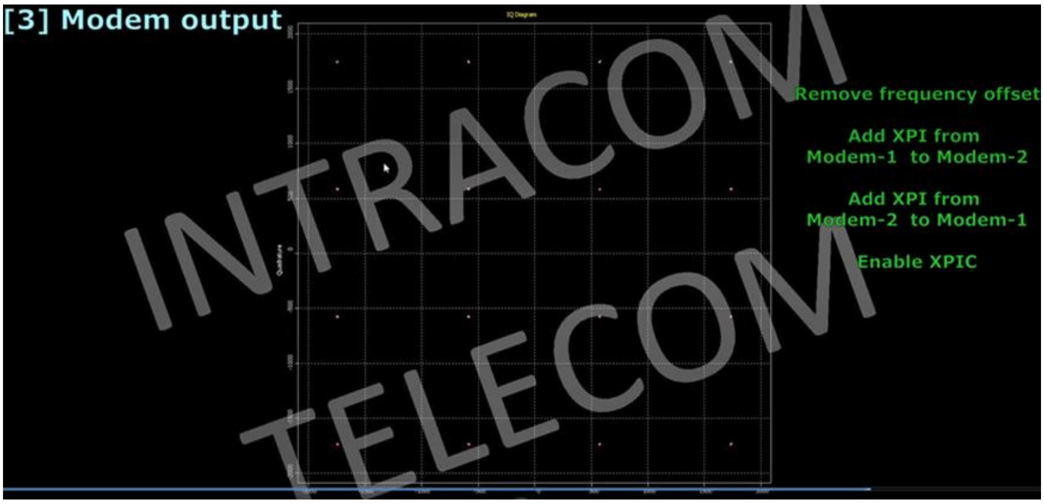

Figure 9: Constellation diagram of recovered QAM symbols at the output of Modem-2

As can be seen, the symbol recovery is almost perfect due to the digital loopback experimental implementation.

2.1.4 Conclusions

This section presented the baseband unit and the DAC/ADC boards supporting the PtP LOS demonstrator. The BBU was enhanced to compensate the specific D-band impairments and offers increased spectral efficiency through the introduced polarization multiplexing. Towards this, the baseband receiver unit was capable of mitigating the D-band specific depolarization effects through a developed XPIC architecture. The BBU was tested in a digital loopback mode and its performance was reported in presence of XPI, with and without the correction capability of the XPIC algorithm.

2.2 Radio design for exploiting frequency and spatial diversity

2.2.1 Local oscillator generation and proof-of-concept LO design

2.2.1.1 Motivation for this work and theoretical considerations

Frequency hopping in the D-band is an attractive approach which fully makes use of the broadband front-end solutions developed in ARIADNE. There are several key-applications for frequency hopping. Firstly, it can act as an enabling technology for beam steering in combination with frequency scanning antennas. In that context, it also allows the illumination of frequency selective metasurfaces. Secondly, frequency hopping helps to combat multipath fading in the channel as well as near-field reflections. Lastly, it can be used to encode the transmission for secure transmission at the physical layer, if the hopping protocol is only known to the transmitter and receiver. The requirements for a local oscillator, which should be used for frequency hopping in a communication system, are low phase noise, short hopping time and low spurious.

Most promising approaches for implementing a local oscillator for fast frequency hopping rely on direct digital synthesis (DDS) and phase locked loops (PLL). Although DDS has a fast hopping-time, its high phase noise, spurious and low output frequency are problematic for use as a reference oscillator signal that gets frequency multiplied to D-band. In contrast, PLLs can achieve low phase noise with minimal spurious, but the possible hopping time is slow [2]. To speed up the switching time, a “ping-pong” approach, which uses two PLLs and a fast switch between the outputs can be used, as for example demonstrated in [3]. In [3] the authors can achieve a switching time of 1 µs with a frequency resolution of 3 Hz, which is considerably (x20) faster than switching the frequency within the PLL. The authors use a combination of direct digital synthesis (DDS) and PLL to achieve a fine frequency resolution.

In the work presented here, a ping-pong PLL approach is also used. To approach optimal phase noise performance, a low phase noise reference oscillator is used at the input of the PLL. The frequency resolution can be achieved within the fractional-N PLL, which has 32-bit registers for setting the frequency dividers. A high frequency hopping speed is gained with a high bandwidth RF-switch at the output of the local oscillator.

The performance of a communication system can be indicated with the bit error rate (BER). The BER depends on the jitter of the data signal. The jitter in turn is related to the phase noise of the local oscillators at the transceiver [4]. To achieve a good system performance, the phase noise of the local oscillator should be as low as possible.

The relationship between jitter and phase noise can be stated as,

$$\sigma_a = \sqrt{\frac{2}{\omega_0^2}\int_0^{+\infty} L(f)df} \tag{1}$$

with σ_a= root mean square (RMS) absolute jitter, ω_0= carrier frequency and $L(f)$ = phase noise.

In [5] the relationship between BER and the RMS jitter is shown:

$$BER(t_s) = 0.5 \cdot erfc\left(\frac{t_s}{\sigma_a \sqrt{2}}\right) \tag{2}$$

Here t_s is the sampling instance and $erfc$ is the complementary error function.

The switching time of the investigated architecture consists of several factors, which are shown in Figure 10.

In a first step of the protocol, the registers of the frequency divider need to be programmed. Here the SPI speed is the limiting factor. Examples for the write time of the registers are given in Table 2. Two state-of-the-art commercial PLL chips with integrated VCO from Texas Instruments are compared. For the LMX2594 150 bits need to be written to the PLL with a maximum SPI speed of 12.25 MHz. It takes 12 µs to program the corresponding registers. The LMX2820 uses double buffering of the registers, which allows the programming of all registers at once. With a higher maximum SPI speed, the write time of the registers can be decreased to about 0.5 µs.

After setting a frequency with the divider registers, the voltage-controlled oscillator (VCO) needs to be calibrated in a next step. This takes 28 µs with the LMX2594 and can be as fast as 2.5 µs with the LMX2820, which is optimized for fast VCO calibration. When the VCO calibration is done, the loop needs to settle to the new frequency, which can take between 11 µs for the LMX2820 and 28 µs for the LMX2594. In total the switching time is limited to 68 µs for the LMX2594 and 14 µs for the LMX2820.

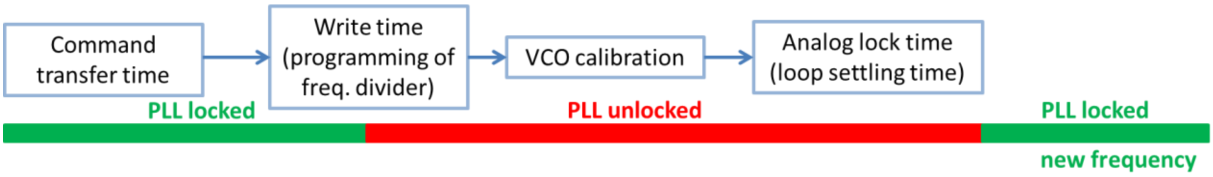

Figure 10: Decomposition of switching time in a fractional-N PLL

Table 2: Comparison of switching times between Texas Instruments PLLs

PLL Chip	LMX2594	LMX2820
Write time of freq. divider registers	6 registers, 25 bit each: 150 bit SPI speed: 12.25 MHz → 12 µs	Double buffering of registers SPI speed: 50 MHz → 0.5 µs
VCO calibration	28 µs	2.5 µs
Analog lock time	28 µs	11 µs
Estimated total switching time	**68 µs**	**14 µs**

In a communication system the aim is to lose as few symbols as possible while changing the carrier frequency. Converting the above-mentioned switching times into symbol rates gives only 14.7 kBaud and 71.4 kBaud.

2.2.1.2 Design and implementation of the dual-PLL solution

Figure 11 gives an overview over the complete radio frequency (RF) front-end with a control interface, as it will be implemented in the ARIADNE project. The local oscillator feeds the carrier signals, ranging from 7.8 - 11 GHz to the front-ends, where they are upconverted by a factor of 16 to the RF carrier frequency. The local oscillator has a controller that can receive commands from the front-end master controller. The master controller provides an access to the outside world, e. g., a modem or a network control plane manager.

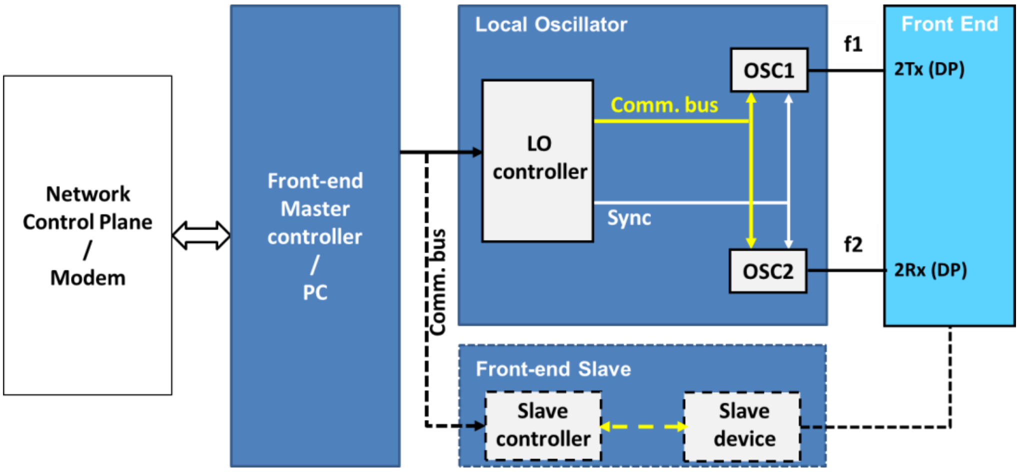

Figure 11: Overview over the ARIADNE D-band front-end with telemetry interface

The concept for the local oscillator slave device (compared to Figure 11) is shown in Figure 12. In this implementation, different local oscillators are used for the TX and RX side. Using a ping-pong approach for fast switching, each local oscillator consists of two PLLs and a switch to select one PLL output. A microcontroller or FPGA is used to parametrize the PLLs and to control the switching and muting of the PLLs. The local oscillator slave device can be controlled via a master controller, via UART bus.

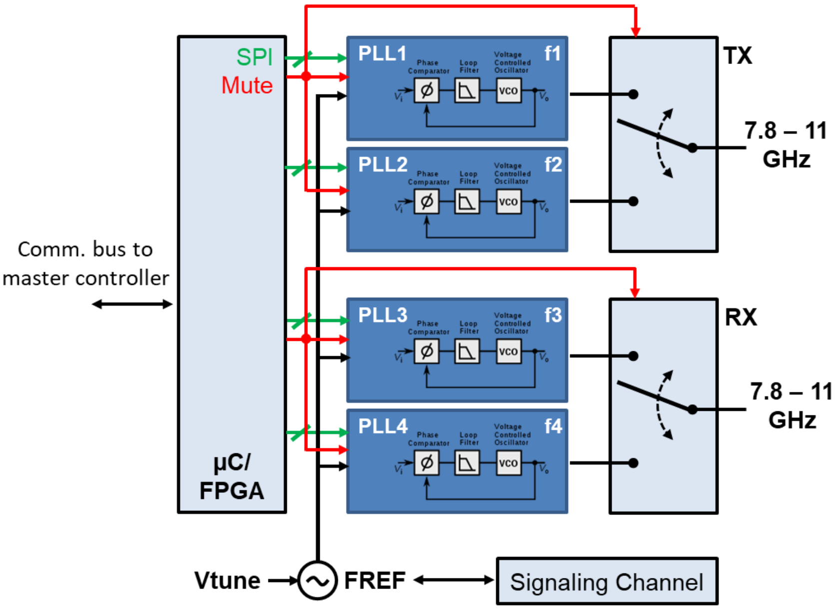

Figure 12: Block diagram of local oscillator

One channel of the proposed concept in Figure 12 is implemented for the proof-of-concept. Figure 13 shows a block diagram of the implementation of the local oscillator, highlighting the most important

RF and control signals. The frequency generation uses a 100 MHz reference oscillator, which is connected to the PLLs. The output of the PLLs is fed to a cascade of switches. The switch at the output is used for fast switching between the PLLs. The switches at the PLLs are used to increase the isolation between the PLL outputs. The microcontroller configures the PLLs and controls the mute signals, as well as the control signals of the RF switches. The microcontroller also takes care of the communication with the master controller.

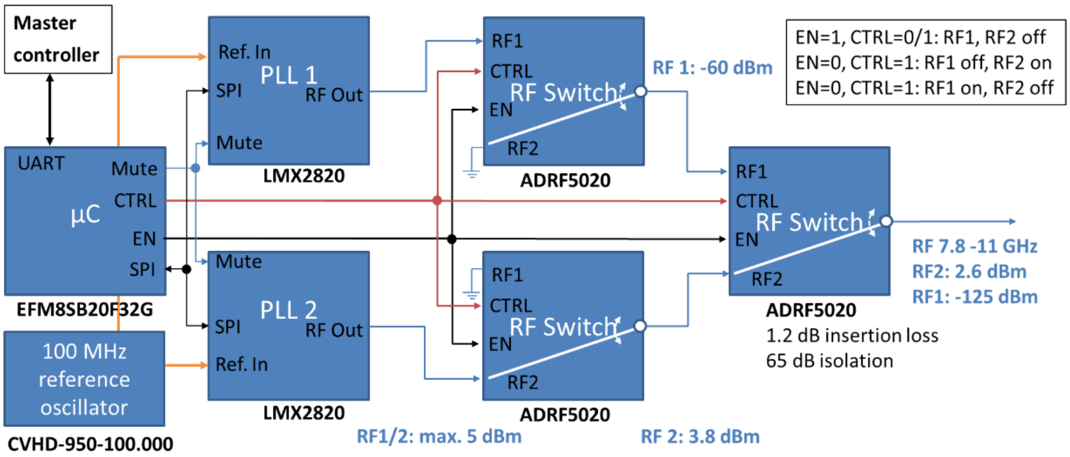

Figure 13: Implementation of one local oscillator channel, used for a proof of concept

In order to minimize the phase noise of the local oscillator output signal, a low phase noise reference oscillator was chosen. Since the phase noise of the reference oscillator has a strong influence on the phase noise of the output signal, especially at offset frequencies close to the carrier that are below the loop bandwidth, different reference oscillators were investigated. Table 3 provides a comparison of different reference oscillators with 100 MHz output frequency and with low phase noise. The oscillators are presented with decreasing phase noise and increasing temperature stability from top to bottom. The table reveals that, regrettably, the power consumption, price and size are increasing from the top to bottom of the table as well, which requires some compromise. For a first demonstrator design the Crystek CVHD-950-100.000 was chosen for that reason.

In order to select a PLL, commercially available PLL chips were surveyed as summarized in Table 4. Only PLLs with a fractional-N divider and an integrated VCO that cover at least the frequency range from 7.8 to 11 GHz, were included.

For the design of the demonstrator, the LMX2820 was chosen in the end for the following reasons: it has an output mute function that allows to disable the output driver, it features “phase sync”, which allows the synchronization of the phase difference between two PLLs, it has the lowest noise floor with -236 dBc/Hz (fractional channel and the lowest normalized 1/f noise with -134 dBc/Hz, and it has a high output power of up to 5 dBm. Due to the fact that the fractional denominator is 32-bit long, the frequency resolution can be better than 1 Hz.

Table 3: Comparison of 100 MHz reference oscillators

Part number	Manu-facturer	Type	Phase Noise @ 100 Hz (dBc)	Phase Noise @ 1 MHz (dBc)	Temp. stability (ppm)	Power consumption (W)	Price (€)	Size (mm x mm)
CVHD-950-100.000	Crystek	VCXO	-119	-169	20	0.05	22	19 x 14
AN-X3AUXXX5-X-100.000MHz	NEL	VCXO	-125	-172	10	0.132	405	17 x 14
501-04623	Wenzel	OCXO	-130	-176* @20 kHz, highest freq. in datasheet	0.2	2.5	2390	74 x 44

Table 4: Comparison of commercial PLL chips with integrated VCO

Part number	Manufacturer	RF output freq. range	Max. RF output power (dBm)	Typ. power dissipation (mW)	Price (€)	Misc.
ADF5610	Analog Devices	57 MHz – 14.6 GHz	10	815	82	3.3 V and 5 V supply needed, no phase sync
LMX2594	Texas Instruments	10 MHz – 15 GHz	5	1122	56	Single 3.3 V supply, phase sync possible
LMX2880	Texas Instruments	45 MHz – 22.6 GHz	5	1947	76	Single 3.3 V supply, phase sync possible, output mute possible

The ADRF5020 from Analog Devices was chosen as the switch, because it offers a very fast switching time of 2 ns (rise and fall time, 10 % / 90 % RF output), high isolation of up to 65 dB at 10 GHz and low insertion loss of 1.2 dB at 10 GHz. A block diagram of the ADRF5020 is shown in Figure 14.

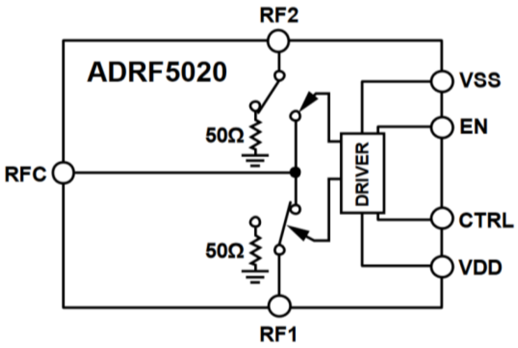

Figure 14: Block diagram of Analog Devices ADRF5020 high speed RF switch [6]

As shown in Figure 11 the front-end slave devices, like the local oscillator, are controlled by a front-end master controller. On the local oscillator PCB, a microcontroller is used to program the PLL and for communication with the master controller. For the communication between master and slave, the UART interface was chosen, because it is easy to implement and the data rates between master and slave are rather low. The communication with the PLL-chip is done via SPI in this implementation, which is the only interface available in the PLL chip. For testing the PCBs, a PC with a USB to UART interface was used as the master controller.

For the communication between the master and the slave devices, a protocol was defined according to Table 5. Communication can take place in both directions, but it needs to be always initiated by the master controller.

Table 5: Bus protocol for master/slave communication

Data Format		
Byte	**Value**	**Comment**
0	0xAA	Start byte
1	TX-ID	Message transmitter (device list)
2	RX-ID	Message receiver (device list)
3	Length = {N+1}	Message length (number of bytes)
4	Direction	0 : Transmitter to receiver only
		1 : Transmitter to receiver + response from receiver to transmitter
5	Command / Register	LSB Command / Register
6		MSB Command / Register
7	data word 0	LSB data word 0

8		MSB data word 0
::	data word 1	LSB data word 1
::		MSB data word 1
::	data word M	LSB data word M
::		MSB data word M
N – 1	CRC	Checksum: sum of all transmission bytes (excluding byte N-1!). Bit 7-0 of the sum is CRC.
N	0x55	Stop byte

The command and associated data are part of the bus protocol (byte 5 onwards) and are listed for the local oscillator slave device inTable 7. The master can read an ID string from the slave, which also includes the firmware version of the slave microcontroller. Several parameters can be read: the lock status of the PLL, the current frequency, the frequency limits, which can be varied depending on the frequency band definitions at D-band, the output power at the rms detector, the current output driver strength, the switch setting and the mute status of the PLL. The following parameters can be written to the local oscillator: the output frequency, the output driver strength, a value for the DAC, which fine tunes the frequency of the reference oscillator, the setting for the switches and the output mute for the PLL. Additionally, the PLL registers can be accessed for debugging purposes, a PLL reset can be performed and an error marker is available, in case a faulty command was sent.

Table 6: Command list of local oscillator slave device

Commands				
Description	Command	Dir 0: write 1: read	Transmitter sends **(UInt16)**	Receiver sends **(UInt16)**
			(Datum 0 / 0 - M)	(Datum 0 / 0 - M)
ID-String	0x0000	0	--	--
		1	0: 0x0000	0 (LSB): 1st Character (ASCII) 0 (MSB): 2nd Character (ASCII) 1 (LSB): 3rd Character (ASCII) 1 (MSB): 4th Character (ASCII) :: ::
Lock-Status	0x0001	0	--	--
		1	0: 0x0000	0: 0 → unlocked 1 → PLL 2 locked 2 → PLL 1 locked 3 → PLL 1 & 2 locked

Frequency	0x0002	0	0: PLL#(15:8), R(7:0) 1: N, uint, [14:0] 2: numerator, uint, [31:16] 3: numerator, uint, [15:0] 4: denominator, uint, [31:16] 5: denominator, uint, [15:0]	0: PLL#(15:8), R(7:0) 1: N, uint, [14:0] 2: numerator, uint, [31:16] 3: numerator, uint, [15:0] 4: denominator, uint, [31:16] 5: denominator, uint, [15:0]
		1	0: 0x0001 (PLL 1) 0x0002 (PLL 2)	0: R, uint 1: N, uint, [14:0] 2: numerator, uint, [31:16] 3: numerator, uint, [15:0] 4: denominator, uint, [31:16] 5: denominator, uint, [15:0]
Frequency Range	0x0003	0	--	--
		1	0: 0x0000	0: min freq (int, uint) 1: min freq (numerator, uint) 2: min freq (denominator, uint) 3: max freq (int, uint) 4: max freq (numerator, uint) 5: max freq (denominator, uint)
Measured Output Power	0x0004	0	--	--
		1	0: 0x0001 (PLL 1) 0x0002 (PLL 2)	0: power [mdBm] (2er)
Output Driver Strength (0 – 7)	0x0005	0	0: PLL(15:12), OUTx(11:8), Value (7:0) (PLL = 1 or 2) (OUTx = 1 (A) or 2 (B)) (Value: 0x00… 0x07)	0: PLL(15:12), OUTx(11:8), Value (7:0) (PLL = 1 or 2) (OUTx = 1 (A) or 2 (B)) (Value: 0x00… 0x07)
		1	0: PLL(15:8), OUTx(7:0) (PLL = 1 or 2) (OUTx = 1 (A) or 2 (B))	0: OUTA_PWR
Register (0 – 122)	0x0006	0	0: PLL(15:8), address (7:0) (PLL = 1 or 2), (address = 0-122) 1: data (15:0)	0: PLL(15:8), address (7:0) (PLL = 1 or 2), (address = 0-122) 1: data (15:0)
		1	0: PLL(15:8), address(7:0) (PLL = 1 or 2) (address = 0 – 122)	0: PLL(15:8), address (7:0) (PLL = 1 or 2), (address = 0-122) 1: data (15:0)
Reset PLL	0x0007	0	0: 0x0001 → PLL 1 0x0002 → PLL 2	0: 0xAAAA
		1	--	--
Reference Osc. Tuning	0x0008	0	0: data (12 bit, right-justified)	0: data (12 bit, right-justified)
		1	--	--
Switch PLL Output	0x0009	0	0: 0x0001 (PLL 1) 0x0002 (PLL 2)	0: 1 → PLL 1 at switch output 2 → PLL 2 at switch output
		1	0: 0x0000	0: 1 → PLL 1 at switch output 2 → PLL 2 at switch output
Mute PLL Output	0x000A	0	0: 0x0000 (unmuted) 0x0001 (PLL 1) 0x0002 (PLL 2) 0x0003 (PLL 1 & 2)	0: 0 → unmuted 1 → PLL 1 muted 2 → PLL 2 muted 3 → PLL 1 & 2 muted

		1	0: 0x0000	0: 0 → unmuted 1 → PLL 1 muted 2 → PLL 2 muted 3 → PLL 1 & 2 muted
Error-Marker	0xFFFF	--	--	--
		--	--	0: command-number causing error

The physical transfer of the commands takes place via the UART interface. For UART, three wires are needed between master and slave: UART_TX, UART_RX and GND. The bus can be implemented as a separate bus for each slave or as a common bus, as schematically shown in Figure 15.

Both bus structures were used in experiments with multiple slave devices. The main disadvantage of separate busses is that the master controller needs a separate UART interface for each slave and therefore the number of slaves is limited. In the future a common bus should be used to make the system expansion more convenient and less hardware dependent.

The used port configuration is listed in Table 7. The port voltage is 3.3 V.

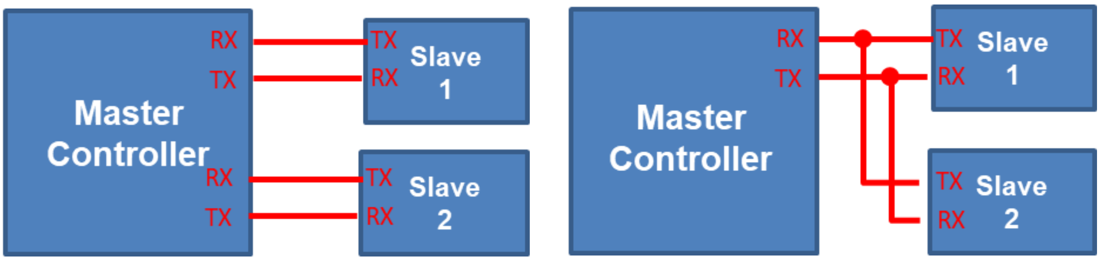

Figure 15: UART bus structure. Separate busses (left side), common bus (right side)

Table 7: UART port parameter configuration

UART port configuration	
Baud	9600
Data bits	8
Stop bit	1
Parity	none

For the experimental verification of the local oscillator, a PCB was designed and assembled that implements the block diagram in Figure 13, using the selected components. Several design iterations were carried out in order to reach the design shown in Figure 16, which was used for the experiments presented in the next chapter.

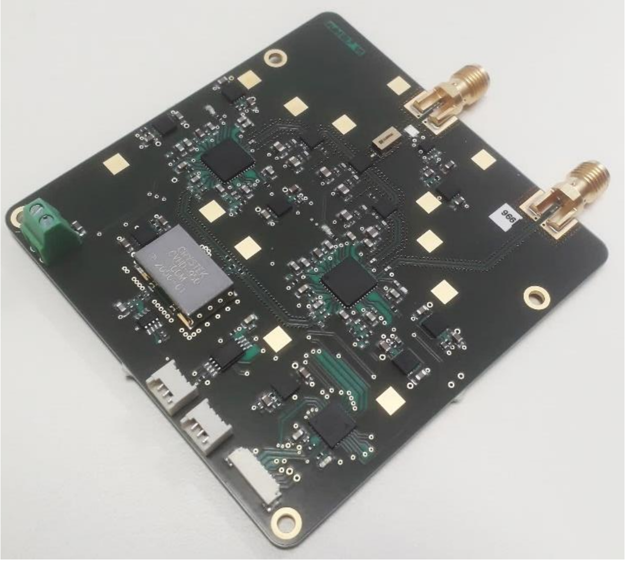

Figure 16: Dual PLL PCB for experimental proof of concept

2.2.1.3 Experimental verification

In a first step, the current consumption of the PCB was measured using a laboratory power supply unit set to 5 V and is 1.275 A with one PLL output muted and 1.36 A, with both outputs unmuted.

The phase noise of the local oscillator output was measured with a Keysight PXA N9030A spectrum analyser with phase noise option. The measurement result is shown in Table 8 and Figure 17 over a frequency offset range between 100 Hz and 10 GHz from the carrier. A spurious can be seen at 25 MHz offset from the carrier with an amplitude of -127 dBc. In the low phase noise region starting at around 10 MHz the measurement is limited by the dynamic range of the spectrum analyser.

Table 8: Measured phase noise values

Offset Frequency	Single Sideband Phase Noise (dBc(Hz)
100 Hz	-68
1 kHz	-98
10 kHz	-104
100 kHz	-106
1 MHz	-122
10 MHz	-141

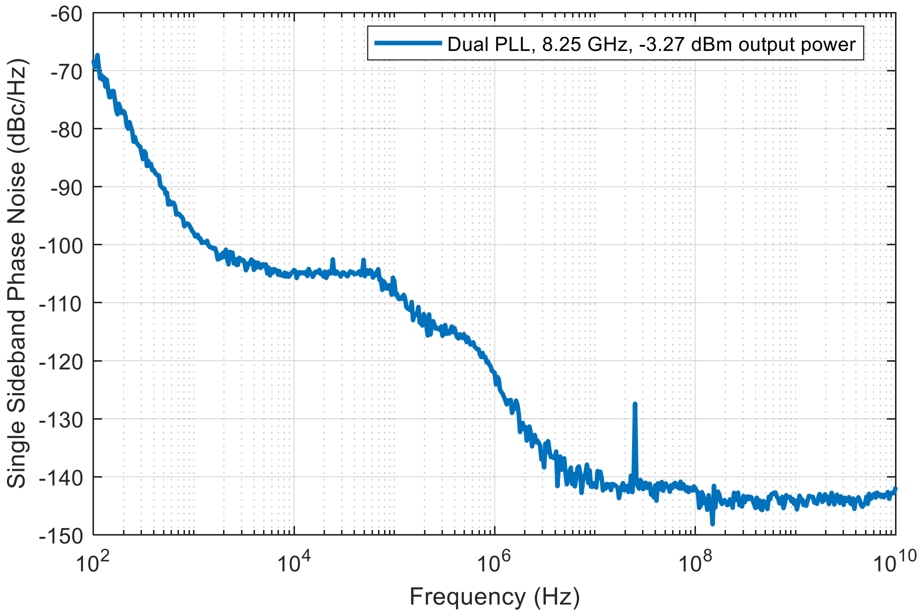

Figure 17: Measured SBB phase noise over offset frequency from carrier

The drift of the output frequency during warm-up of the local oscillator was measured over an interval of 30 minutes and is shown in Figure 18. It can be seen that the PLL output reaches a stable output after about only 5 minutes of warm-up time. The measurement was carried out using a Keysight PXA N9030A spectrum analyser.

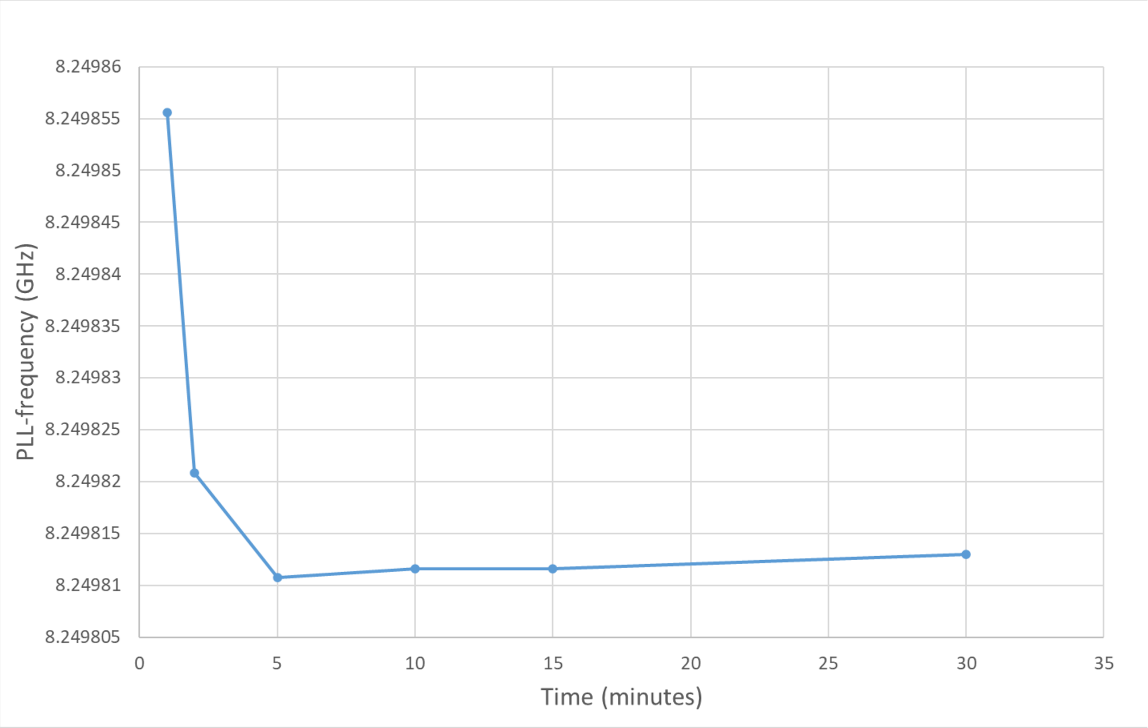

Figure 18: Warm-up behavior of the local oscillator

The isolation between the PLL outputs was measured using Keysight PXA N9030A spectrum analyzer. The isolation is greater than 49 dB, if the output of the unused PLL is not muted and greater than 62 dB using the mute function of the PLL for the unused output. The mute function of the LMX2820 allows to disable the output driver of the PLL.

The switching time of the local oscillator output was measured using a Lecroy LabMaster 10 Zi-A real time oscilloscope with 80 GS/s and is shown in Figure 19. With the real time oscilloscope, the waveform with the switching event could be sampled and shown in time domain. The switching time is in the range of 5.4 ns and magnitudes faster than what can be achieved with one PLL alone.

Verification of the functionality of the commands listed in Table 6 was successfully done. A PC with a USB to UART interface was used with a self-written program on the PC to create and execute the commands. The functionality of a common UART bus was also shown using to PLL devices.

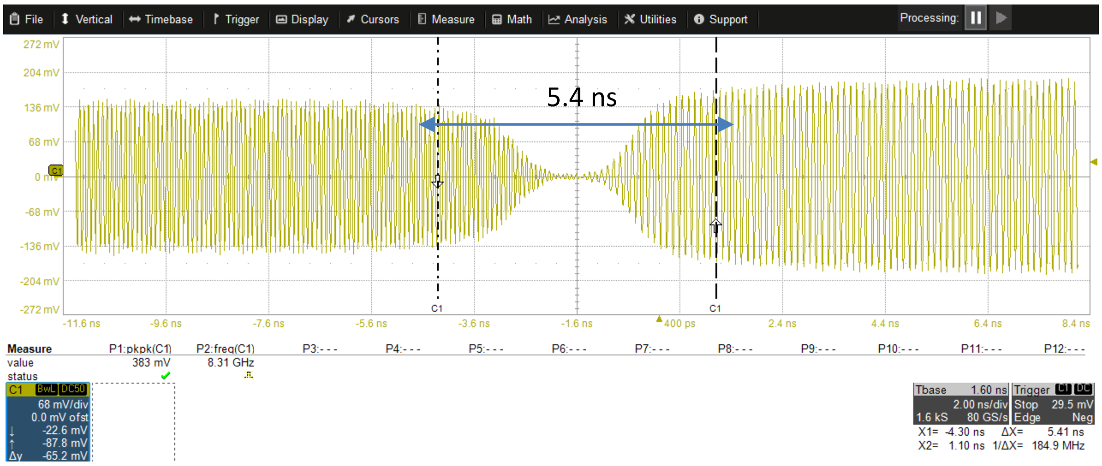

Measure	P1:pkpk(C1)	P2:freq(C1)	P3:- - -	P4:- - -	P5:- - -	P6:- - -	P7:- - -	P8:- - -	P9:- - -	P10:- - -	P11:- - -	P12:- - -
value	383 mV	8.31 GHz										
status	✓											

C1 BwL DC50
68 mV/div
0.0 mV ofst
↓ -22.6 mV
↑ -87.8 mV
Δy -65.2 mV

Tbase 1.60 ns
2.00 ns/div
1.6 kS 80 GS/s

Trigger C1 DC
Stop 29.5 mV
Edge Neg

X1= -4.30 ns ΔX= 5.41 ns
X2= 1.10 ns 1/ΔX= 184.9 MHz

Figure 19: Measured switching time of the local oscillator

2.2.1.4 Summary

The practical implementation of frequency-switching at D-band was discussed with respect to the generation of the carrier signal and the needed reference oscillators signal. The work must be considered in the context of the overall radio front-end design as report in D3.1 and D3.2. For proof-of-concept, the hardware was tested by prototype designs that will be employed and further modified for the use in the final outdoor unit of the point-2-point demonstrator. It was shown, that switching times as low as 5.4 ns can be achieved with the dual-PLL approach with an isolation of close to 50 dB between the individual carriers. All this can be achieved with high spectral purity, little phase noise degradation and low thermal drift after a warm-up time of 5 minutes without oven-control. The bus protocol of the control interface was defined and tested, which will be extended or embedded in the radio control unit of the outdoor unit as part of WP5.

3 Antenna designs and prototypes

In this section we will describe in detail the designs of the selected high gain reflector antennas (HGA) appropriate for the Long Range LOS scenario as described in D3.1 [1]. Two design concepts for reflector antennas have been investigated: a) single-reflector offset fed and b) dual-reflector Cassegrain. Details of the feed horn designs are presented as well. Additionally novel concept designs of ellipsoid dielectric lens antennas are presented to be used for NLOS and LOS indoor scenarios as a medium gain antenna (MGA).

3.1 High Gain Reflector Antennas and Feed Horns

This subsection presents the horn antennas designed to work as feeders of the reflector antennas and conclude to the final selected ones as optimum solutions. Additionally, the optimization procedure and the concept of the reflector antennas will be extensively presented in terms of topology (single reflector front fed and dual reflector Cassegrain) parametric analysis and performance evaluation. Finally the optimum designs in terms of performance, size and weight are selected.

3.1.1 Requirements, Reference and Design Concepts

Requirements and Concepts

According to deliverable D3.1 the HGA concepts selected to be used for long range scenario were the front fed offset reflector antenna and the Cassegrain antenna. The required gain should be above 45dBi for all 4 D-band channels. Therefore, in the theoretical initial design we must achieve, at least, 48dBi gain by adding a +3dB margin to take into account: surface losses, misalignment, imperfections, feed losses, etc.

Reference

For the HGAs design a reference reflector antenna from M3TERA project has been used as reference [7]. The reference antenna is a front fed offset reflector antenna which has been already successfully used for long range scenario which required Gain above 38dBi. It must be noted that the diameter of this reflector is 10cm. The reference antenna data are depicted in Table 9 (Gain, Edge Taper (Spill-Over)).

Table 9: Gain and Edge-Taper values of reference M3TERA HGA and of an ideal antenna

	Reference Antenna		Ideal antenna (aperture efficiency 81%)	
F (GHz)	**Gain (dBi)**	**Edge-Taper (dB)**	**Gain (dBi)**	**Edge-Taper (dB)**
110	39.57	-6.11	40.30	-11
145	42.56	-12.30	42.70	-11
170	43.54	-12.70	44.08	-11

Based on the reference antenna the spill-over edge tapers (ET) should be targeted between: -12dB to -13dB for all D-band channels. So according to theory, ET are approximately equal to feed taper (FT). FT is directly linked with radiation patterns of feed horns. After defining target value of FT we should define taper angle. Taper angle is defined in [8]. The values for all geometrical parameters of the reference HGA are shown in Table 10. Hence the derived value of the feed taper angle of the reference antenna is 42.3deg (***Ψ_B*, *Ψ_S*)**.

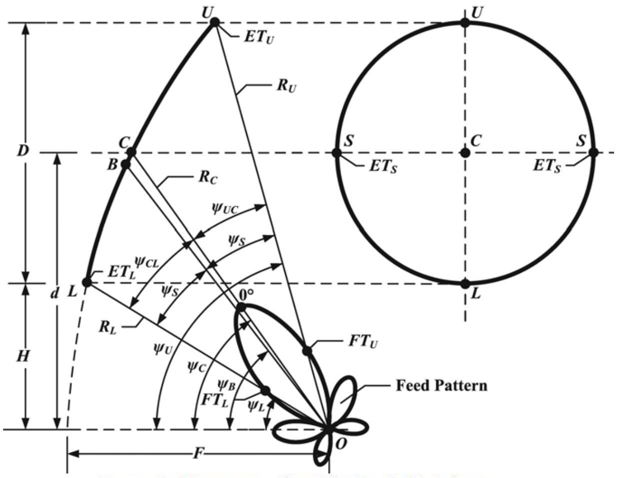

Geometrical Parameters of an Offset Parabolic Reflector

	Definition	Remarks
F	Focal length	—
D	Reflector diameter	Diameter of the circular projected aperture
H	Offset height	$H = -D/2$ for symmetric reflectors
d	Offset height of the projected aperture center	$d = D/2 + H$
D_p	Parent parabola diameter	$D_p = 2(D + H)$ for $H \geq -D/2$
ψ_U	Angle subtended to the upper tip of reflector	$\psi_U = 2\tan^{-1}[(D + H)/(2F)]$
ψ_C	Angle subtended to the projected aperture center	$\psi_C = 2\tan^{-1}[(D/2+ H)/(2F)]$
ψ_L	Angle subtended to the lower tip of reflector	$\psi_L = 2\tan^{-1}[H/(2F)]$
ψ_B	Angle subtended in the bisect direction	$\psi_B = (\psi_U + \psi_L)/2$
ψ_S	Half-angle subtended to the upper and lower tips	$\psi_S = (\psi_U - \psi_L)/2$
ψ_{SC}	Half-angle subtended to the left and right sides	

$$\psi_{SC} = \sin^{-1}\left\{\frac{D}{2}\Bigg/\sqrt{\left(H+\frac{D}{2}\right)^2+\left(\frac{D}{2}\right)^2+\left[\frac{(D/2)^2+(H+D/2)^2}{4F}-F\right]^2}\right\}$$

Figure 20: Design parameters of front fed offset reflector antenna (theoretical geometry equations)

Table 10: Reference antenna (front fed offset reflector) geometrical parameters

Parameter	Value
D (m)	*0.1*
F (m)	*0.055*
HH (m)	*0*
H (m)	*0*
D (m)	*0.05*
D_p (m)	*0.2*
Ψ_U (°)	*84.5*
Ψ_C (°)	*48.9*
Ψ_L (°)	*0*
Ψ_B (°)	*42.3*
Ψ_S (°)	*42.3*
Ψ_{SC} (°)	*40.0*
Ψ_{UC} (°)	*35.7*
Ψ_{CL} (°)	*48.9*

Concluding, in this subsection the general geometry of HGA has been defined and feed horn required characteristics (FT, FTangle) to achieve performance similar to the reference antenna are determined. According to theoretical calculations a feed horn with such specific characteristics should perform with gain from 12-14dBi [9].

It must be noted here that the feed horn in terms of a similar Cassegrain design, compared with a front fed, should be more directive (higher gain) to cover lower angles of feed taper to subreflector. However, the feed horn for both offset and Cassegrain should be the same to keep the size of feed horn more compact. Though there would be a trade-off with increased required subrflector size and blockage.

3.1.2 Theoretical analysis and basic design parameters

The selected two types of HGAs are the front fed offset and the Cassegrain. They both have similar (common) components such as: main reflector, feed horn and supporting structure or struts. The Cassegrain design has also a sub-reflector, the struts exist at both designs but in different shapes. In this subsection the electromagnetic effect of the above-mentioned design components are described and the selection of the values of their design parameters is explained. It must be noted that the initial antenna designs do not include struts and supporting structures. The struts analysis will be included in the final realistic designs of the antennas (in sub-section 3.1.8).

Main reflector

The reflector's dimensions define the level of the antenna gain according to equation:

$$\boldsymbol{Gain}\ [\boldsymbol{dBi}] = \mathbf{10log}\ (\mathbf{k}\left(\frac{\pi\ D}{\lambda}\right)^{2})$$

(3)

where k is the antenna aperture efficiency, D is the reflector diameter and λ is wavelength of the frequency of operation.

Based on goals settled in D3.1 and described in previous subsection Gain should be at least 48dBi for all four D-band channels in terms of final detailed realistic reflector antennas. As can be seen from eq. (3) reflector diameter is a critical parameter for Gain. Based on this equation a theoretical analysis calculations of gain is carried so as to find required diameter covering the target gain. In these calculations (in terms of initial design) k is assumed equal to 81% (the maximum ideal value). In Table 11a Gain vs Diameter is shown.

Table 11: Theoretical Calculated Gain vs. Diameter

a) for ideal reflector efficiency (81%) and b) for realistic reflector efficiency (50%)

a)

F (GHz)	10cm	20cm	30cm
132.00	41.89	47.91	51.43
144.75	42.69	48.71	52.23
157.75	43.44	49.46	52.98
170.90	44.13	50.15	53.67

b)

F (GHz)	10cm	20cm	30cm
132.00	39.79	45.81	49.33
144.75	40.59	46.61	50.14
157.75	41.34	47.36	50.88
170.90	42.04	48.06	51.58

From the Table 11a it can be easily said that a reflector diameter 20cm can cover the target of 48dBi Gain for all four D-band channels. But these results are for the best achievable (ideal) aperture efficiency of 81%. According to [8] and in terms of realistic implementations, typical reflector antennas efficiency is 50-70%. So the 50% efficiency is the worst case scenario. The respective results for 50% efficiency is shown in Table 11b.

So after these results and in terms of achieving a final realistic design, which will include all loss factor due to surface error, struts, implementation imperfections, illumination-spillover etc. and cover the required 48dBi gain we choose the 30cm reflector diameter.

Feed Horn

The conical horn type has been selected for feed horn design instead of pyramidal due to its symmetry in terms of radiation performance and compactness. The gain of conical horn as a target is settled between 12-14dBi. The equation (4) connects physical dimension which is the diameter (d) and aperture area (A) of the horn with gain and with aperture efficiency (*e*). Aperture efficiency is generally ranging from 0.4 up to 0.8. Also the diameter is linked with length (L) of the horn with eq. (5). The higher the diameter the higher the gain, but with respective increase of the horn length.

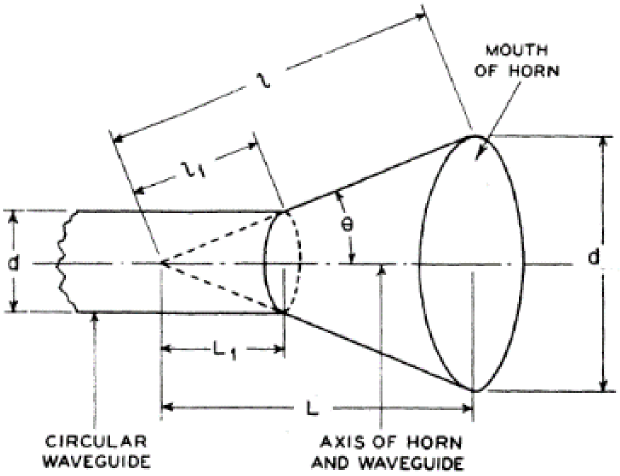

Figure 21: **Conical horn geometrical parameters**

$$\boldsymbol{Gain} = \left(\frac{\boldsymbol{\pi d}}{\boldsymbol{\lambda}}\right)^{2} \boldsymbol{eA} \qquad (4)$$

$$\boldsymbol{d} = (3\boldsymbol{\lambda L})^{\frac{1}{2}} \qquad (5)$$

The diagram in Figure 22 presents the theoretical curves to calculate horn antenna diameter and length so as to achieve a specific gain. It can be understood from this theoretical figure that various pairs of horn length and aperture diameter can result into Gain between 12-14dBi. In combination with theory and after various simulations in Table 12 various pairs of d and L are recorded leading to gain between 12-14dBi, for λ=2mm (average wavelength in D-band).

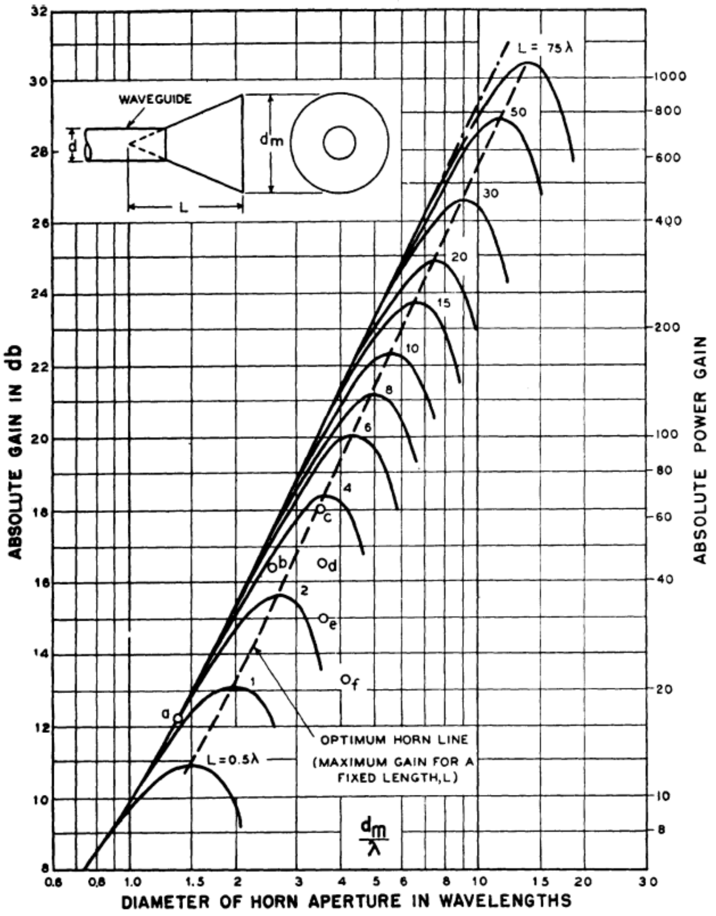

Figure 22. The absolute Gain of a conical horn as a function of aperture physical diameter (d/λ), for a series of horn lengths, L [10]

Table 12: Length and diameter of horn antennas with gain 12-14dBi

case	L-L1 (mm)	d (mm)
1	2.5	3.182
2	3	3.538
3	3.35	3.787
4	3.5	3.894
5	4	4.25

From Table 12 we select case 2 as it yields more smooth radiation characteristics and better feed taper results, closer to the ideal Gaussian one.

Subreflector

To minimize loss from diffraction and illumination spillover, the subreflector should be electrically large, greater than 10 wavelengths in diameter (Ds). Moreover the subreflector diameter should be less than 20% of the main reflector diameter (D) to minimize blockage by the subreflector, so the dish diameter of the main reflector should be larger than 50 wavelengths.

Though in our case Ds/D could be larger due to wider feed taper (due to lower feed horn gain)

Supporting structure or struts

The supporting structure or struts in both cases of HGAs will have effect in terms of blockage, gain degradation and cross-pol increase (Related analysis is presented in sub-section 3.1.8).

3.1.3 Feed Horn Antenna Designs

Procedure of finding initial conical feed horn satisfying the performance requirements

After theoretical analysis described in previous subsection we have concluded to case 2 horn dimensions (Table 12) that have been have been selected as initial feed horn design (C0). After optimization procedure through HFSS we have found a more compact design maintaining d=3.538mm and L-L1=2.407mm. The comparison between horn no.2 (C0) and new optimized horn (C1) is depicted in Table 13. Both horns are compared with an ideal Gaussian horn. They both yield acceptable Gain. C0 is better in terms of feed taper (FT) but C1 is superior in terms of X-pol. Which is assumed a critical parameter. Though, C1 is selected and due to this deviation from expected FT an optimization in terms of HGA dimensions and parameters is required.

Table 13: Performance comparison of Gaussian horn, initial (C0) and selected (C1)

F (GHz)	Gain (dBi)			X-pol. (-dB/MAX)			FT @ -42.27deg (dB)/ FT @ +42.27deg (dB)		
	Gauss.	C0	C1	Gauss.	C0	C1	Gauss.	C0	C1
132.00	13.41	13.74	12.73	300	15.95	18.38	-12.43/ -12.43	-12.11/ -12.06	-11.51/ -11.51
144.75	13.43	13.22	12.78	300	14.21	18.20	-12.47/ -12.47	-11.20/ -11.20	-11.84/ -11.82
157.75	13.51	13.51	13.77	300	15.52	19.61	-12.70/ -12.70	-10.54/ -10.57	-14.35/ -14.17
170.90	13.56	13.28	14.55	300	13.75	17.96	-12.85/ -12.85	-10.71/ -10.47	-14.98/ -15.06

Performance analysis of all feed horn designs

In previous subsection the approximate gain of the horn for achieving respective feed tapers are defined. Based on the results of previous analysis the feed horns that have been designed are the following:

- Conical-1 (C1): First conical horn, improved version of C0.
- Conical-2 (C2): Increased dimensions of C1, being marginally between conical and Picket Potter
- Conical-3 (C3): Increased C1 horn length by λ/2
- Picket Potter (PP): Picket Potter version of C3 by appropriate adjustment of "Picket step"
- Flare Potter (FP): Picket Potter version of C1 maintaining the radiating aperture dimensions

The geometry of the -above feed horn antennas can be seen in Figure 23.

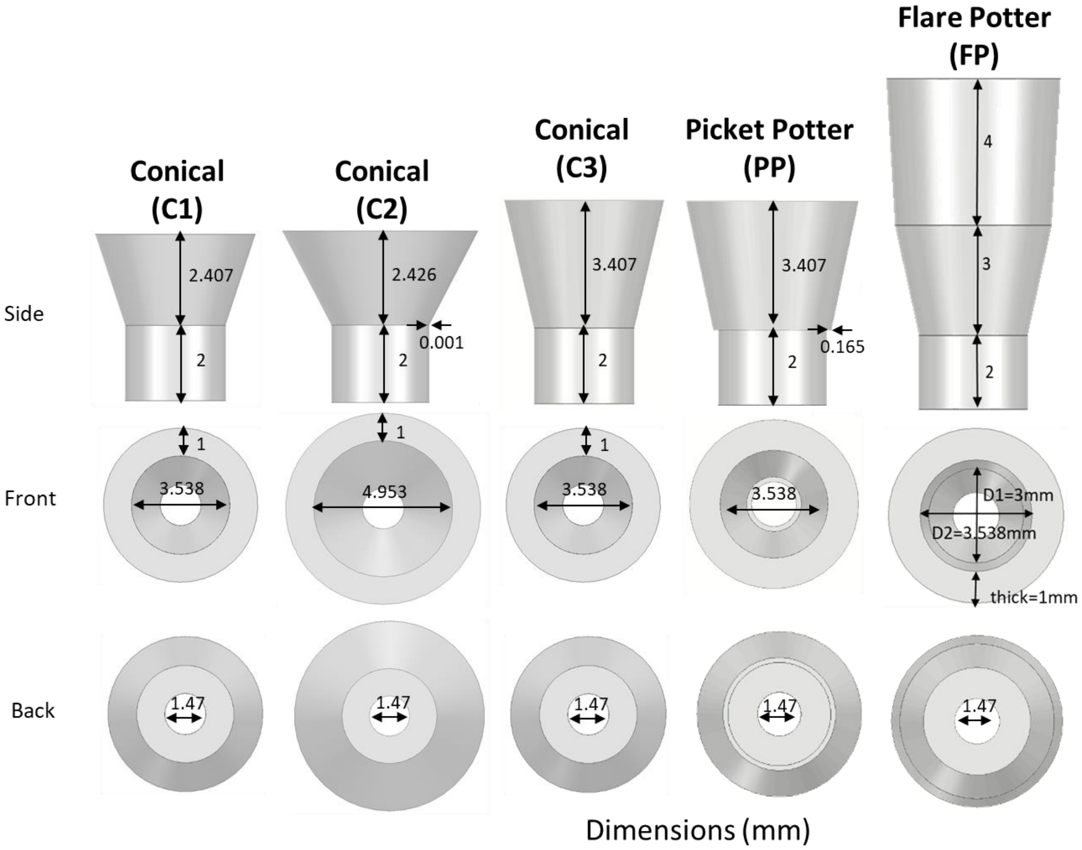

Figure 23: Feed horn antennas proposed designs

The Reflection coefficient S11 of all feed horn is shown in Figure 24. The HFSS simulation models are using PEC material. All designs yield S11 well below -10dB for all four D-band channels. In terms of feed network and excited modes, fundamental TE11 mode is assumed only, with no higher order modes to be propagated and excited. Additionally, the feed horns have been excited for circular polarization (LHCP).

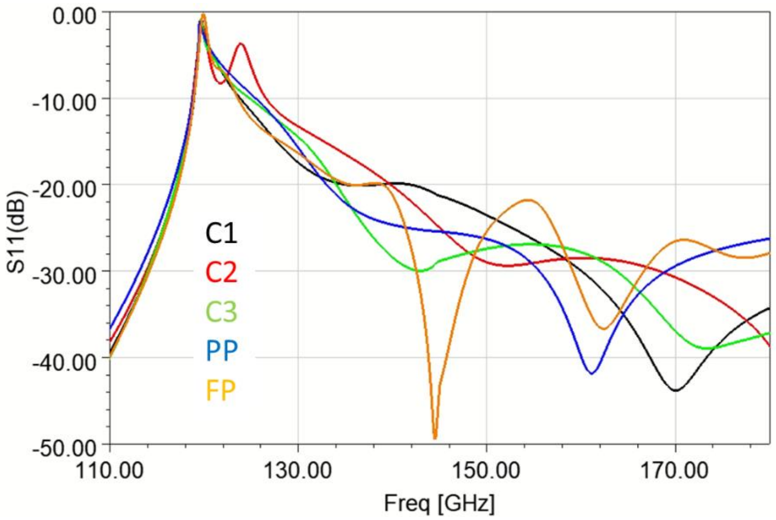

Figure 24: Reflection Coefficient (S11) simulation results of proposed feed horn antennas

The far field parameters, Gain, Cross-polar and Feed Taper (@42.27deg) are shown in Table 14, Table 15,Table 16, Table 17 and Table 18 for each one of the examined feed horn.

Table 14: C1 Horn Far Field Parameters

F (GHz)	Gain (dBi)	X-pol. (dB/MAX)	FT(dB) @-42.27deg	FT(dB) @+42.27deg
132.00	12.73	-18.38	-11.51	-11.51
144.75	12.78	-18.20	-11.84	-11.82
157.75	13.77	-19.61	-14.35	-14.17
170.90	14.55	-17.96	-14.98	-15.06

Table 15: C2 Horn Far Field Parameters

F (GHz)	Gain (dBi)	X-pol. (dB/MAX)	FT(dB) @-42.27deg	FT(dB) @+42.27deg
132.00	13.90	-18.17	-12.40	-12.43
144.75	14.11	-15.23	-11.08	-11.16
157.75	14.29	-16.42	-11.69	-12.00
170.90	15.11	-17.23	-13.81	-13.72

Table 16: C3 Horn Far Field Parameters

F (GHz)	Gain (dBi)	X-pol. (dB/MAX)	FT(dB) @-42.27deg	FT(dB) @+42.27deg
132.00	12.74	-17.86	-11.53	-11.57
144.75	13,34	-20.68	-13.25	-13.37
157.75	14.10	-18.61	-15.91	-15.78
170.90	14.75	-18.27	-16.38	-16.26

Table 17: PP Horn Far Field Parameters

F (GHz)	Gain (dBi)	X-pol. (dB/MAX)	FT(dB) @-42.27deg	FT(dB) @+42.27deg
132.00	12.61	-18.76	-11.23	-11.27
144.75	13.58	-21.3	-14.11	-14.11
157.75	14.03	-18.58	-15.56	-15.61
170.90	15.09	-21.85	-18.96	-19.02

Table 18: FP Horn Far Field Parameters

F (GHz)	Gain (dBi)	X-pol. (dB/MAX)	FT(dB) @-42.27deg	FT(dB) @+42.27deg
132.00	13.16	-27.00	-11.88	-11.84
144.75	13.93	-21.21	-15.13	-15.11
157.75	14.59	-18.52	-17.77	-17.80
170.90	15.36	-18.36	-18.31	-18.59

Trade-off analysis for feed horn selection

Based on far field performance and on criteria settled in (previous subsection) a trade-off analysis for selecting best feeders is carried out. The trade-off compares for each horn the achieved values for far-field parameter (e.g. Gain) with the required target values. The trade-off analysis scoring is depicted in Table 19. A description of the weights for each parameter scoring is the following:

- Gain: weight factor = 1 (as all cases yield similar values)
- X-pol: weight factor = 2 (as a main goal for improvement)
- FT: weight factor = 0.5 (the specific value applies for the similarity to reference design) as a reference one for F/D=0.55 (which after optimization will be changed as shown in following analysis)

Table 19: Horn Antennas Performance Trade-off analysis scoring table

Cases	Gain (x1)	X-pol. (x2)	FT (x0.5)	Total
C1	5	4	2	11
C2	2	2	2.5	6.5
C3	4	6	1.5	11.5
PP	3	8	1	12.0
FP	1	10	0.5	11.5

The horn antennas from highest to lower score are: PP, FP, C3, C1, C2 and for final designs three are selected: C3, PP, FP so as to have one of each type (conical, picket potter, and flare potter).

The radiation patterns of the selected feed hon designs are presented in Figure 25 and Figure 26.

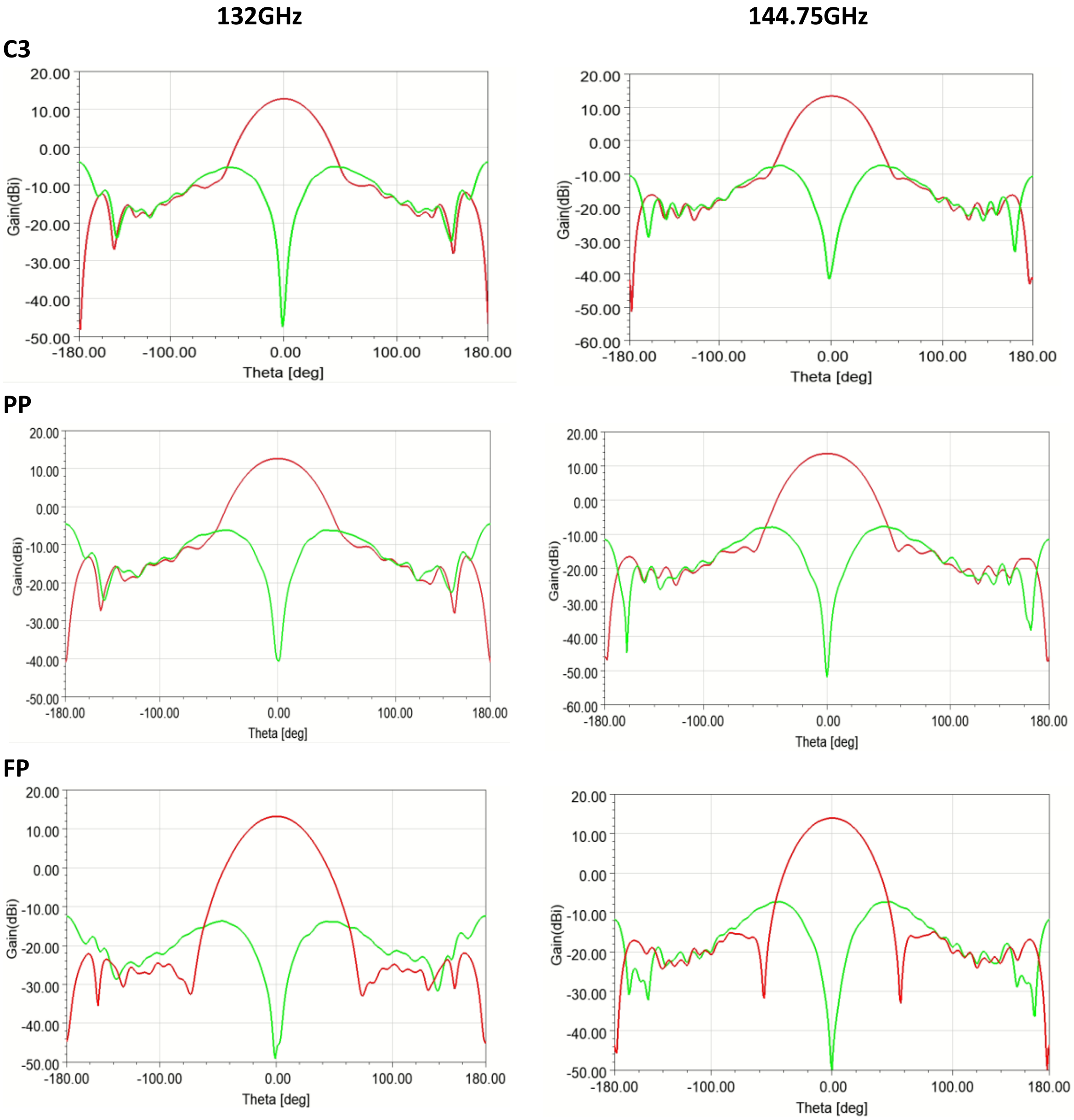

Figure 25: Radiation Patterns (LHCP and RHCP) @132GHz and 144.75GHz for: C3, PP, FP

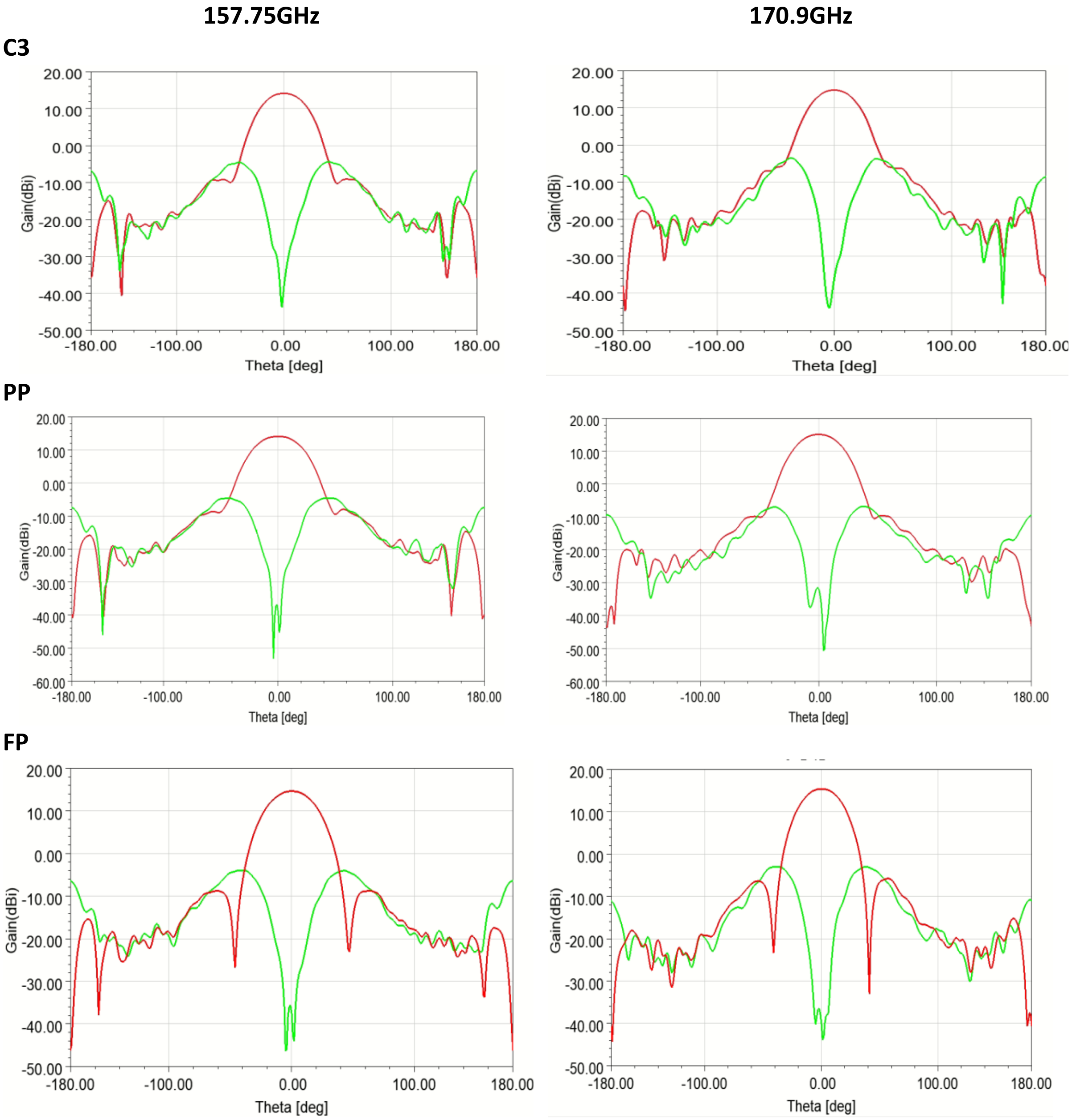

Figure 26: Radiation Patterns (LHCP and RHCP) @157.75GHz and 170.9GHz for: C3, PP, FP

<u>Pros and Cons of final selected designs</u>

The three selected feed horn antennas yield differences in terms of performance and implementation simplicity and size. More specifically:

C3 is quite compact in size and the easiest in terms of implementation as it is a simple conical horn antenna. In terms of performance it yields best target Gain and FT but highest X-polar (still acceptable). Hence in general terms of performance it is the worse antenna.

PP is quite compact as C3 and the most difficult in terms of implementation as it requires this short and delicate step transition from waveguide to flare, for which a small deviation could changes completely the performance results, making this design quite sensitive in this parameter. In general terms of performance this is the best antenna. More specifically it is in the middle of ranking out of three selected antennas.

FP is larger than other two feed horns in terms of length and same in terms of aperture. In terms of implementation it is harder than C3 and easier than PP. In general terms of performance it ranks second. More specifically it is the best in terms of cross polar and the worse in terms of target gain and FT.

It can be understood that a variety of requirements can be satisfied or not with the selection of each horn. All three feed horns are acceptable in terms of targeted performance. All of them have a weakness in terms of FT which is expected to yield slightly worse results for the reference offset front fed HGA reflector. Still an optimization procedure has been carried out for each horn to find best geometrical parameters of HGA design.

3.1.4 Optimization procedure of HGAs

After designing the feed horn antennas and selecting the best ones in terms of performance, these have been used for the design and optimize the HGAs (offset and Cassegrain). So the feed horns C3, PP and FP have been used as feed horns for the HGA design. In the following the design and optimization procedure in terms of performance, geometrical parameters effect is described. A main constant geometrical parameter which is defined and selected from initial theoretical approach and analysis and will not change throughout the whole design and optimization procedure is the diameter of the main reflector for both concepts (front fed offset and Cassegrain).

For both design concepts the criteria for designing, parametrizing and consequently selecting the final designs were: the performance, the size and implementation complexity of the HGAs. More specifically the criteria of performance include: Gain to be above 48dBi and possible to maximize up to 53-54dBi, X-pol. Settled to meet below -30dB so as to meet the 30dB XPIC requirement, SLL to be below 10dB and ideally close to 20dB-25dB to isolate possible interference. The size is mainly determined by the F/D and will results into larger or smaller antenna volume. Finally the ease of implementation firstly is linked with the selected feed horn and the HGA concept. It must be noted that the most important criteria are the related to the antenna performance.

For each concept the criteria and mainly the performance has been investigated and are affected by the variation of feed horns and geometrical parameters of the HGA concepts such as the focal length, the offset distance, the sub-reflector diameter.

3.1.5 Offset front fed reflector antenna design

Initial reference performance

As a first estimation of front fed offset HGA we simulated the selected three feed horns: C3, PP, FP embedded on reference HGA geometry. The results of these simulations are depicted in Table 20.

Table 20: Far Field results for reference HGA geometry for feed horns: C3, PP and FP

F (GHz)	Gain (dBi)			X-pol. (dB/MAX)			SLL-(dB/MAX) / SLL+(dB/MAX)		
	C3	PP	FP	C3	PP	FP	C3	PP	FP
132.00	50.47	50.61	51.16	-22.9	-23.79	-32.53	-28.79/ -31.74	-27.59/ -31.43	-27/ -24.38
144.75	51.56	51.61	51.56	-26.17	-26.7	-25.83	-30.1/ -32.6	-29.55/ -33.46	-29.27/ -35.91
157.75	51.69	51.69	51.45	-22.61	-22.39	-21.44	-30.69/ -34.2	-30.45/ -33.7	-36.98/ -35.54
170.90	51.92	52.34	51.27	-20.64	-24.41	-19.04	-29.45/ -32.31	-30.49/ -34.92	-36.75/ -35.96

All reference HGA feed horn cases yield very good Gain and SLL but their main disadvantage is the X-pol levels. Though optimization further has been done in terms of geometrical parameters (focal length, F and offset length, d) for each feed horn case. The optimization "goal" and trade-off would be to improve X-pol without degrade SLL below -20dB.

Optimization results

The results that have been concluded from optimization procedure (described in sub-section 3.1.4) are in total 6 (2 for each selected feed horn design). Out of two one design achieves significantly better X-pol and the other is more compact in terms of size/volume maintaining acceptable performance. The six designs geometrical characteristics are depicted in Table 21. The results for each case are shown below in Table 22 to Table 27 .

Table 21: Selected Optimized Offset Front Fed HGA designs

design	F(cm)	d(cm)
C3/1	26.86	25
C3/2	20.00	15
PP/1	26.86	25
PP/2	20.53	15
FP/1	26.86	25
FP/2	17.89	20.04

Table 22: C3/1 Far field results

F (GHz)	Gain (dBi)	X-pol. (dB/MAX)	SLL- (dB)	SLL+ (dB)
132.00	49.82	-30.28	-20.36	-19.42
144.75	51.18	-35.09	-20.5	-19.69
157.75	52.21	-33.74	-21.34	-20.37
170.90	52.98	-31.05	-22.57	-20.93

Table 23: C3/2 Far field results

F (GHz)	Gain (dBi)	X-pol. (dB/MAX)	SLL- (dB)	SLL+ (dB)
132.00	50.66	-25.12	-24.44	-21.72
144.75	51.85	-28.82	-25.3	-22.18
157.75	52.3	-25.73	-28.49	-23.2
170.90	52.67	-23.41	-32.23	-32.14

Table 24: PP/1 Far field results

F (GHz)	Gain (dBi)	X-pol. (dB/MAX)	SLL- (dB)	SLL+ (dB)
132.00	49.84	-31.04	-20	-19.22
144.75	51.31	-35.02	-20.58	-20.01
157.75	52.16	-33.37	-21.2	-20.25
170.90	53.29	-34.97	-22.19	-21.32

Table 25: PP/2 Far field results

F (GHz)	Gain (dBi)	X-pol. (dB/MAX)	SLL- (dB)	SLL+ (dB)
132.00	50.75	-26.14	-23.57	-21.08
144.75	51.94	-29.79	-25.14	-22.74
157.75	52.32	-25.77	-27.49	-23.21
170.90	53.13	-27.53	-30.03	-24.66

Table 26: FP/1 Far field results

F (GHz)	Gain (dBi)	X-pol. (dB/MAX)	SLL- (dB)	SLL+ (dB)
132.00	50.31	-39.69	-20.17	-19.99
144.75	51.44	-34.56	-20.8	-20.51
157.75	52.32	-32.09	-21.72	-21.22
170.90	53.14	-30.11	-22.85	-22.39

Table 27: FP/2 Far field results

F (GHz)	Gain (dBi)	X-pol. (dB/MAX)	SLL- (dB)	SLL+ (dB)
132.00	51.14	-34.81	-23.48	-22.33
144.75	51.85	-28.53	-25.4	-23.21
157.75	52.12	-24.86	-26.91	-23.84
170.90	52.43	-20.99	-26.59	-24.82

<u>Trade-off analysis for concluding to final optimum designs</u>

In order to select at least two out of six HGAs for final designs, a trade-off analysis based on previous presented performance results, including also other parameters such as size of the HGA and complexity of implementation are encountered. Initially a performance scoring was conducted as has been done for feed horn scoring selection. For the performance scoring, Gain and X-pol have the same weight factor (1 and 2 respectively) as for the feed horns in previous section for the similar reasons. SLL has weight factor 1. To fulfill trade-off analysis the size/volume of the antenna and the fabrication complexity have been also considered.

Based on this analysis, the first in the ranking is the antenna design C3/2 and the second one is PP/2. We have disqualified for further investigation PP/2 for the aim of this deliverable due to its difficulty in terms Picket Potter horn implementation and we have selected FP/1 (in third place of the ranking) due to its best performance scoring and not FP/2 which is very good in terms of size and implementation but third in terms of performance.

Concluding, the final selected Offset Front Fed HGA designs are: **C3/2** and **FP/1**.

<u>Note:</u> Hereinafter in this Derivable the offset design C3/2 is referred to as **OFFC3CS** (OFFset C3 Compact Size) and the offset design FP/1 is referred to as OFFFPXM (OFFset FP Xpd Minimized)

3.1.6 Cassegrain reflector antenna design

The initial reference design for Cassegrain antenna that has been used to start performance and optimization analysis had the following characteristics: F/D=0.55, D=30cm, F=16.5cm, Ds/D=0.20, Ds=6cm, ecc=2. Where **F** is the focal length of the main reflector, **D** is the diameter of the main reflector, **Ds** is the diameter of the subreflector, **c** is subreflector half focal length, **a** is subreflector half vertex distance and **ecc** is the corresponding eccentricity of subreflector (ecc=c/a). For each one of the selected 3 feed horns further optimizations have been carried out by parametrizing the focal length the diameter and eccentricity of subreflector. The diameter (D) of the main reflector is the same for all optimized results equal to 30cm and has not changed throughout the whole optimization procedure for all feed horn cases. Additionally, for all designs it has been assumed that the feed horn is mounted always on the base of the reflector, so as to decrease any extra losses (from required waveguide) and any feed horn shadow/blockage. This practically means that F=2c.

For each feed horn a trade-off performance analysis has been carried out for a number of optimized designs so as to select the best two of them. Finally, after selecting two designs for each feed horn we made a trade-off analysis, out of all 6 HGA designs, for concluding to two specific HGA designs in terms of performance, size (volume) and implementation simplicity (similar to offset front fed HGA procedure as presented in previous subsection).

<u>Optimization results</u>

The designs that have been derived from optimization procedure are in total 6 (2 for each selected feed horn design). Generally for each feed horn one design presents better performance especially regarding X-pol but the HGA has larger size comparing to the other that has a more compact design.

The geometrical characteristics of the six Cassegrain designs are depicted in Table 21. The results of each case is shown below in Table 22 to Table 34 .

Table 28: Selected Optimized Cassegrain HGA designs

design	F(cm)	c(cm)	a(cm)	Ds(cm)	ecc	Ds/D	F/D
C3/1	12.00	6.00	3.00	8.62	2.00	0.28	0.40
C3/3	8.00	4.00	2.30	7.50	1.74	0.25	0.27
PP/1	12.00	6.00	3.00	8.62	2.00	0.28	0.40
PP/3	8.00	4.00	2.30	7.90	1.74	0.26	0.27
FP/1	12.00	6.00	3.00	8.62	2.00	0.28	0.40
FP/3	8.00	4.00	2.30	7.50	1.74	0.25	0.27

Table 29: C3/1 Far field results

F (GHz)	Gain (dBi)	X-pol. (dB/MAX)	SLL- (dB)	SLL+ (dB)
132.00	48.16	-30.81	-14.19	-14.07
144.75	49.43	-35.51	-13.84	-13.73
157.75	50.63	-35.49	-14.08	-14.08
170.90	51.45	-32.52	-14.2	-14.1

Table 30: C3/3 Far field results

F (GHz)	Gain (dBi)	X-pol. (dB/MAX)	SLL- (dB)	SLL+ (dB)
132.00	48.47	-28.47	-14.67	-14.6
144.75	49.86	-33.07	-14.8	-14.8
157.75	50.82	-31.86	-14.97	-14.92
170.90	51.51	-29.07	-15.22	-15.2

Table 31: PP/1 Far field results

F (GHz)	Gain (dBi)	X-pol. (dB/MAX)	SLL- (dB)	SLL+ (dB)
132.00	48.18	-31.54	-14.08	-14.12
144.75	49.59	-36.43	-13.78	-13.76
157.75	50.59	-34.86	-14	-14.03
170.90	51.77	-36.36	-14.13	-14.19

Table 32: PP/3 Far field results

F (GHz)	Gain (dBi)	X-pol. (dB/MAX)	SLL- (dB)	SLL+ (dB)
132.00	48.87	-29.09	-14.85	-14.88
144.75	50.3	-33.85	-14.98	-14.94
157.75	51.04	-30.9	-15.08	-15.1
170.90	52.07	-32.62	-15.2	-15.25

Table 33: FP/1 Far field results

F (GHz)	Gain (dBi)	X-pol. (dB/MAX)	SLL- (dB)	SLL+ (dB)
132.00	48.69	-39.57	-14.21	-14.21
144.75	49.7	-35.17	-13.84	-13.87
157.75	50.79	-33.8	-14.15	-14.2
170.90	51.72	-32.12	-14.34	-14.29

Table 34: FP/3 Far field results

F (GHz)	Gain (dBi)	X-pol. (dB/MAX)	SLL- (dB)	SLL+ (dB)
132.00	49.03	-36.62	-14.83	-14.87
144.75	50.12	-32.69	-15.03	-15.05
157.75	50.89	-30.43	-15.2	-15.18
170.90	51.62	-28.58	-15.47	-15.32

<u>Trade-off analysis for concluding to final optimum designs</u>

In order to select two out of six Cassegrain HGAs final designs, a trade-off analysis similar to the one conducted for the selection of Offset front fed HGA has been performed. The analysis was based on previous presented performance results, including size/volume of the HGA and complexity of implementation.

Based on this analysis, PP/3 design is on top 3 but is not further qualified for final detailed design as it is hard to implement. So the best after this disqualification are FP/3, FP/1, C3/3. We would like to have two proposed feed horns at final designs so we select C3/3 as excels in terms of size and simplicity of manufacturing. Then between FP/3 and FP/1 we selected FP/1 as the best in terms of performance.

Concluding, the final selected designs are: **C3/3** (best in terms of size and very good in terms of implementation), **FP/1** (good in terms of implementation and best in terms of performance). Between two selected final designs for Cassegrain HGA there is a trade-off between them in terms of size and performance.

<u>Note:</u> Hereinafter in this Derivable the Cassegrain design C3/3 is referred to as **CAC3CS** (CAssgrain C3 Compact Size) and the Cassegrain design FP/1 is referred to as **CAFPXM** (CAssegraint FP Xpd Minimized)

3.1.7 Selection of final designs

Summarising the results of the optimization and trade-off analysis described in sections 3.1.5 and 3.1.6 the selected HGA designs per design concept are:
<u>Offset front fed:</u> OFFC3CS, OFFFPXM
<u>Cassegrain:</u> CAC3CS, CAFPXM

In Figure 27, Figure 28, Figure 29 and Figure 30 the details (geometry parameters, performance parameters and radiation patterns) for each design are presented. The derived results are based on developed models and electromagnetic simulation analysis using TICRA's GRASP software.

Comparing the <u>Offset designs</u> we can conclude that:
If the primary criteria of selection are the compact size and non-complicated implementation and we do not have strict restrictions on cross-polar performance requirements, then OFFC3CS (Figure 27) compact design should be selected. If emphasis should be given on cross-polar performance, then OFFFPXM design (Figure 28) should be the first selection. Both proposed HGA Offset designs can adequately serve the purpose of ARIADNE long range scenario.

Comparing the <u>Cassegrain designs</u> we can conclude that:
If the primary criteria of selection are the compact size and non-complicated implementation and we do not have strict restrictions on cross-polar performance requirements, then CAC3CS (Figure 29) compact design should be selected. If emphasis should be given on cross-polar performance, then CAFPXM design (Figure 30) should be the first selection. Both proposed HGA Offset designs can adequately serve the purpose of ARIADNE long range scenario.

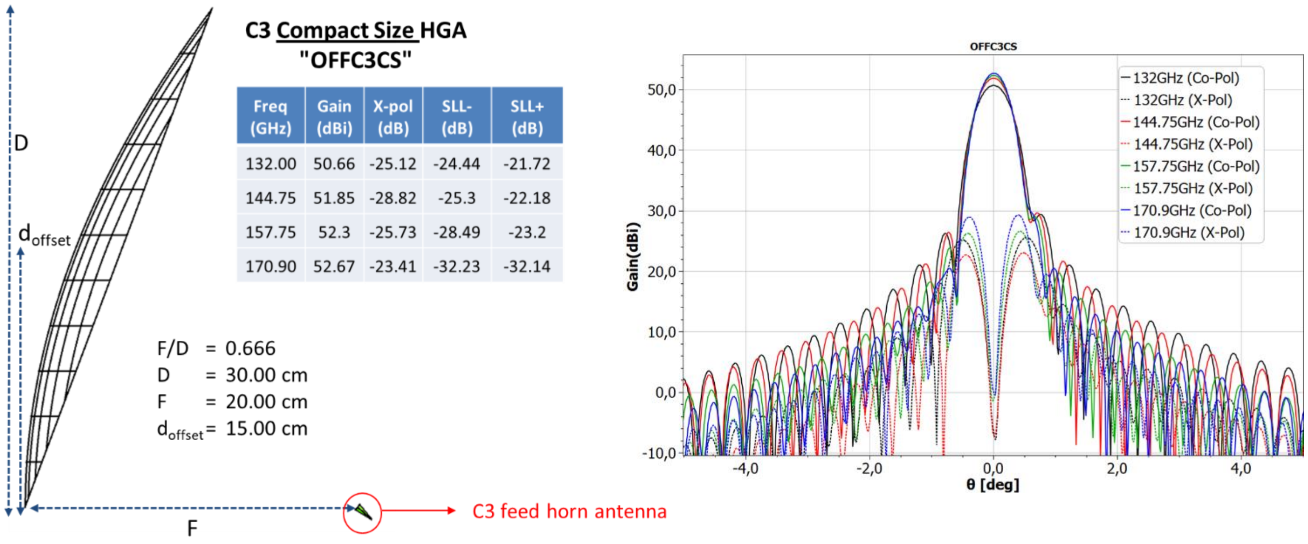

C3 Compact Size HGA
"OFFC3CS"

Freq (GHz)	Gain (dBi)	X-pol (dB)	SLL- (dB)	SLL+ (dB)
132.00	50.66	-25.12	-24.44	-21.72
144.75	51.85	-28.82	-25.3	-22.18
157.75	52.3	-25.73	-28.49	-23.2
170.90	52.67	-23.41	-32.23	-32.14

F/D = 0.666
D = 30.00 cm
F = 20.00 cm
d_{offset} = 15.00 cm

Figure 27: Offset front fed HGA design OFFC3CS, schematic (geometrical parameters), performance parameters and radiation diagrams Co/Cx at phi=0deg at the center frequency of each D-band channel

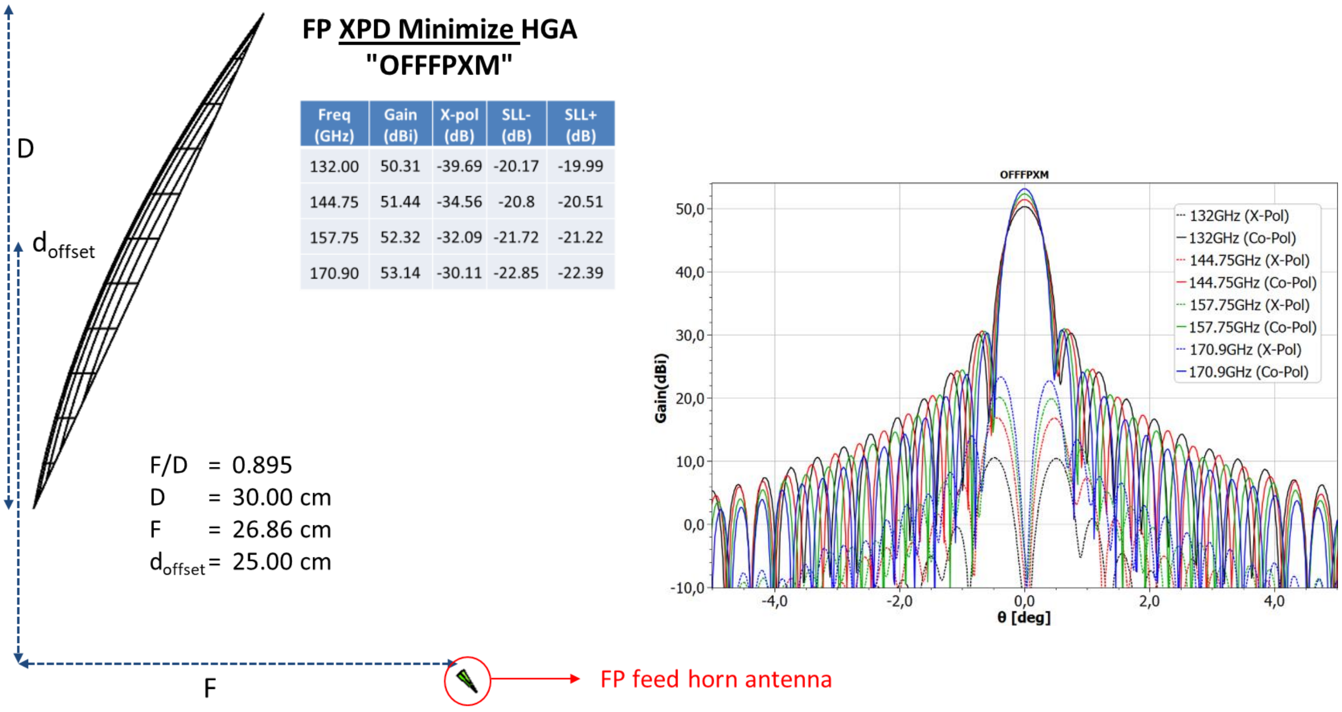

FP XPD Minimize HGA
"OFFFPXM"

Freq (GHz)	Gain (dBi)	X-pol (dB)	SLL- (dB)	SLL+ (dB)
132.00	50.31	-39.69	-20.17	-19.99
144.75	51.44	-34.56	-20.8	-20.51
157.75	52.32	-32.09	-21.72	-21.22
170.90	53.14	-30.11	-22.85	-22.39

F/D = 0.895
D = 30.00 cm
F = 26.86 cm
d_{offset} = 25.00 cm

Figure 28: Offset front fed HGA design OFFFPXM, schematic (geometrical parameters), performance parameters and radiation diagrams (Co/Cx at phi=0deg), at the center frequency of each D-band channel

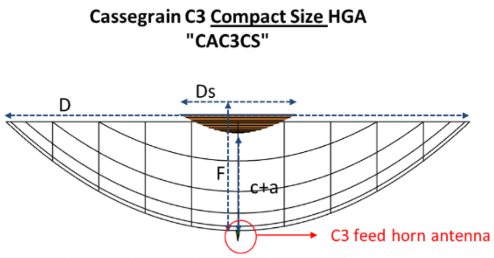

Freq (GHz)	Gain (dBi)	X-pol (dB)	SLL- (dB)	SLL+ (dB)
132	48.47	-28.47	-14.67	-14.6
144.75	49.86	-33.07	-14.8	-14.8
157.75	50.82	-31.86	-14.97	-14.92
170.9	51.51	-29.07	-15.22	-15.2

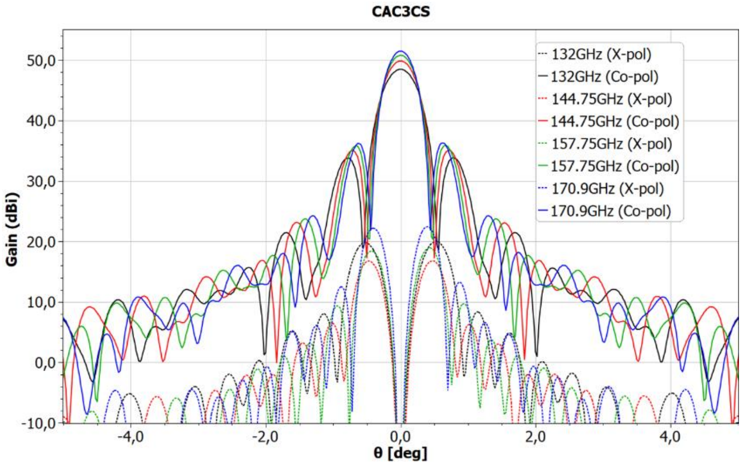

design	D (cm)	F/D	Ecc (c/a)	Ds/D	F (cm)	c (cm)	a (cm)	Ds (cm)
CAC3CS	30	0.266	1.736	0.25	8	4	2.304	7.5

Figure 29: Cassegrain HGA design CAC3CS, schematic (geometrical parameters), performance parameters and radiation diagrams (Co/Cx at phi=0deg), at the center frequency of each D-band channel

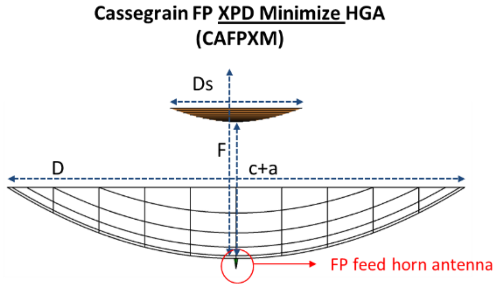

Freq (GHz)	Gain (dBi)	X-pol (dB)	SLL- (dB)	SLL+ (dB)
132.00	48.69	-39.57	-14.21	-14.21
144.75	49.7	-35.17	-13.84	-13.87
157.75	50.79	-33.8	-14.15	-14.2
170.90	51.72	-32.12	-14.34	-14.29

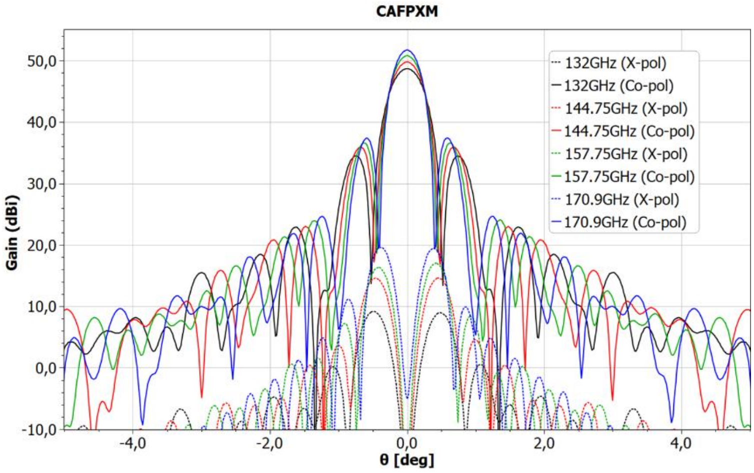

design	D (cm)	F/D	Ecc (c/a)	Ds/D	F (cm)	c (cm)	a (cm)	Ds (cm)
CAFPXM	30	0.4	2	0.29	12	6	3	8.62

Figure 30: Cassegrain HGA design CAFPXM, schematic (geometrical parameters), performance parameters and radiation diagrams (Co/Cx at phi=0deg), at the center frequency of each D-band channel

In order to choose between the four proposed HGA designs, a trade-off analysis needs to be carried out on a case-by-case basis regarding the required performance, implementation complexity, antenna size and weight. In Figure 31 and Table 35 the corresponding information about the size/weight and performance of the proposed antenna designs is included.

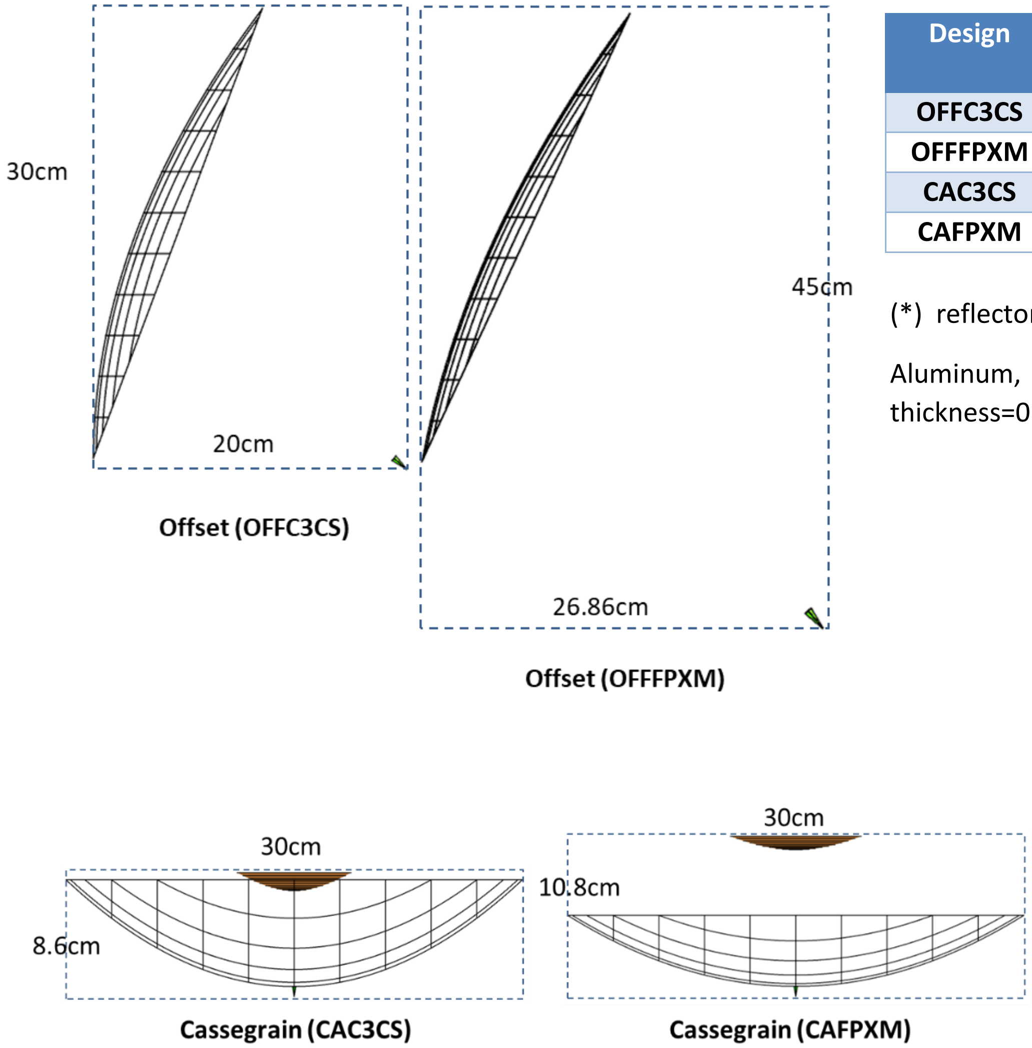

Design	Weight (kg)*
OFFC3CS	1.059
OFFFPXM	1.075
CAC3CS	1.225
CAFPXM	1.138

(*) reflector's material:

Aluminum, thickness=0.5cm

Figure 31: Size and weight comparison of the proposed HGA designs

Table 35: Performance comparison of the proposed HGA designs

Design	Gain (dBi)	XPD (-dB)	SLL- (-dB)	SLL+ (-dB)
OFFC3CS	50.66 - 52.67	23.41 - 28.82	24.44 - 42.23	21.72 - 32.14
OFFFPXM	50.31 - 53.14	30.11 - 39.69	20.17 - 22.85	19.99 - 22.39
CAC3CS	48.47 - 51.51	28.50 - 33.10	14.67 - 15.22	14.60 - 15.20
CAFPXM	48.69 - 51.72	32.10 - 39.60	13.84 - 14.34	13.87 - 14.29

Based on the above analysis, we conclude that all (four) the proposed HGA designs satisfy the requirements of ARIADNE long range scenario. Moreover the **OFFC3CS** design is the easier in manufacturing having also the lighter reflector, the **OFFFPXM** design presents the best performance and the **CAC3CS** has the most compact profile (volume).

3.1.8 Detailed realistic designs

In order to have more realistic analysis of the selected four HGA designs, at least two extra parameters should be examined. These are the influence on the antenna performance of the supporting structures or struts and the surface inaccuracy of the reflectors. In this subsection analysis and effect of these parameters into HGA performance is presented.

<u>Supporting structures / Struts</u>

The front fed offset and the Cassegrain designs require of different type of supporting structures and struts (Figure 32).

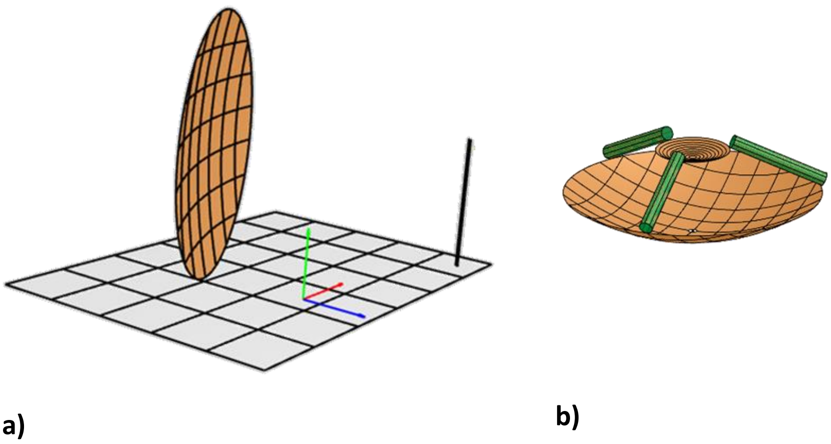

Figure 32: Front fed offset supporting structure (a) and Cassegrain struts concept (b)

For each type (front fed and Cassegrain) different parametric analysis have been carried out to conclude to the best designs with minimum effect comparing to the designs without the struts.

<u>Front Fed</u>

The supporting structure for front fed offset reflector has been shown in Figure 33. The supporting structure for each selected design (OFFC3CS, OFFFPXM) consists of two parts: a) base, b) horn support. Simulation analysis has been carried out to conclude to dimensions of these two parts that will effectively support the antenna and will have minimum effect to antenna performance (reflection, diffraction, blockage etc.). For base part a parametric analysis in terms dimensions has been carried out to examine base influence into gain through reflections and to select the appropriate dimensions. For horn support the height of the horn does not affect antenna performance in terms of blockage but the width can affect the blockage. The width has been selected equal to 6mm appropriate for all feed horn aperture cases (Figure 23). At this horn support dimensions, blockage is not increased compared with the initial non-supporting structure antenna. The material of both part of supporting structure is assumed PEC. For both antenna designs a parametric analysis in terms of base dimensions (x, z) has been carried out. It has been found that the most sensitive dimension parameter is the increment along +z axis (positive-z), which increases base effect on resulting gain. The resulted most appropriate dimensions of the base were 350X250 mm (for OFFC3CS) and 480X340 mm (for OFFFPXM). Indicatively we show in Figure 34 for frequency 157.75 GHz and various base dimensions the radiation diagrams representing electromagnetic field caused by reflections on base at phi=0 deg. Similar results and effect can be noticed in different phi angles.

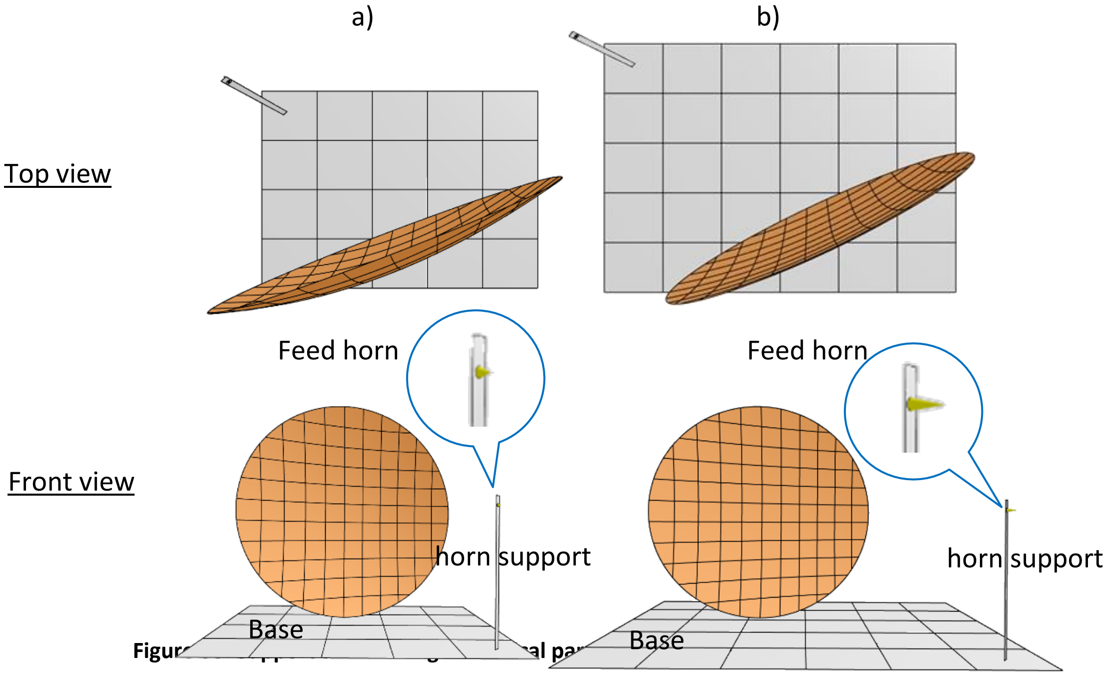

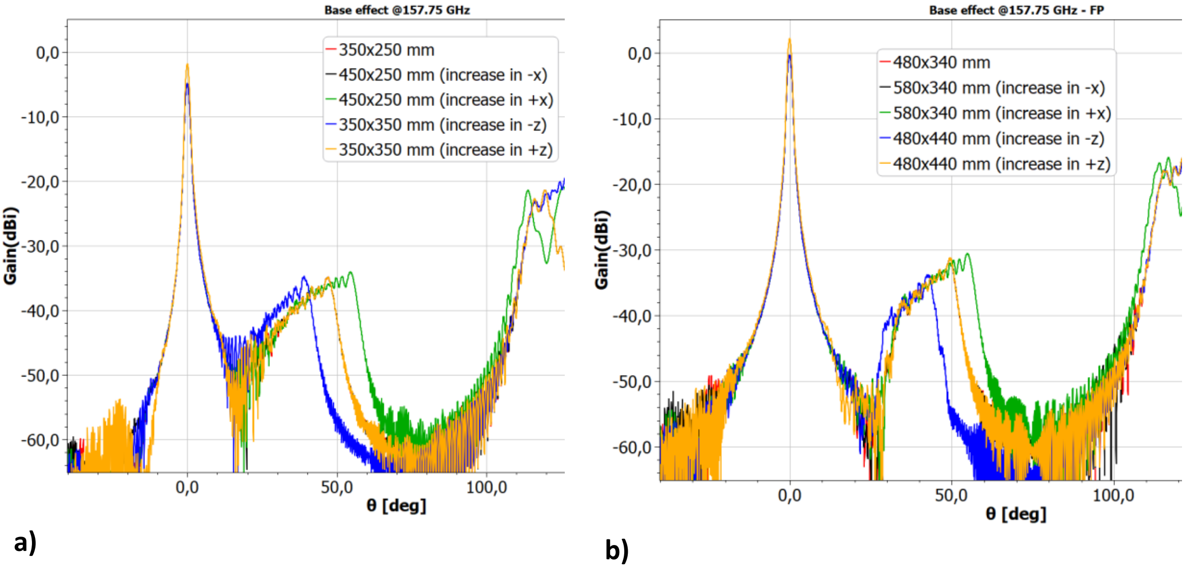

Figure 34: Effect on radiation diagram of OFFC3CS (a) and OFFFPXM (b) from reflections on Base at 157.75GHz and phi=0deg

The radiation patterns for both HGAs including all supporting structures effects can be seen in Figure 35. For both antennas at all frequencies, Gain remains as it was without the supporting structure (as designed). X-pol is slightly increased and SLL insignificantly differ. The supporting structure at both cases has insignificant effect into antenna performance. The far field performance has been examined in other phi angles as well and the main radiation characteristics slightly changed, but it must be noticed that especially in the phi=90 deg cross polar increased significantly not in terms of max-value but in terms of values per theta angle due to the reflections on base.

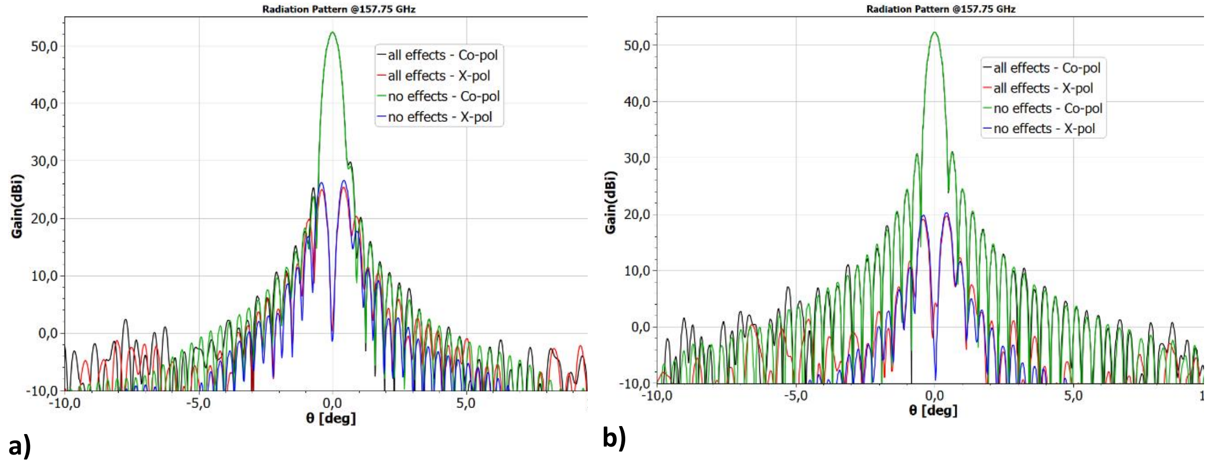

Figure 35: Radiation Patterns including supporting structure effects at 157.75GHz, phi=0deg of OFFC3CS (a) and OFFFPXM (b)

Cassegrain

The struts can be classified in terms of cross-section shape (circular, orthogonal) and in terms of materials (conductive, dielectric), more specifically we have examined circular cross-section struts.

The schematic of circular struts are shown in Figure 36. Firstly for conductive material (PEC) a parametric analysis in terms of strut diameter has been carried out. The antenna performance results (Gain, X-pol and SLL) for both designs CAFPXM and CAC3CS and for diameters: 4mm, 5mm, 8mm, 10mm, 15mm, 20mm, 25mm have been compared with the no-struts case (indicative results for CAC3CS gain are shown in Figure 37).

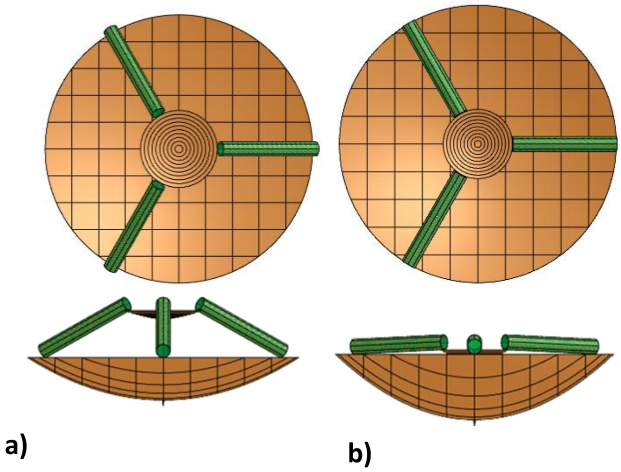

Figure 36: Struts schematics for a) CAFPXM, b) CAC3CS

Conclusions for PEC struts size analysis

For the CAFPXM design struts can degrade Gain by maximum 1.2dB for diameters starting from 4mm up to 25mm, X-pol values for diameters above 10mm (practical solution) is degraded, but not significantly (less than 1dB) and SLL are slightly affected (less than 0.7dB)

For the CAC3CS design struts can degrade Gain by maximum 1.36dB for diameters starting from 4mm up to 25mm, X-pol values for diameters above 10mm (practical solution) is degraded but not significantly (less than 1dB) and SLL is increased as struts diameter increased up to 1.4dB

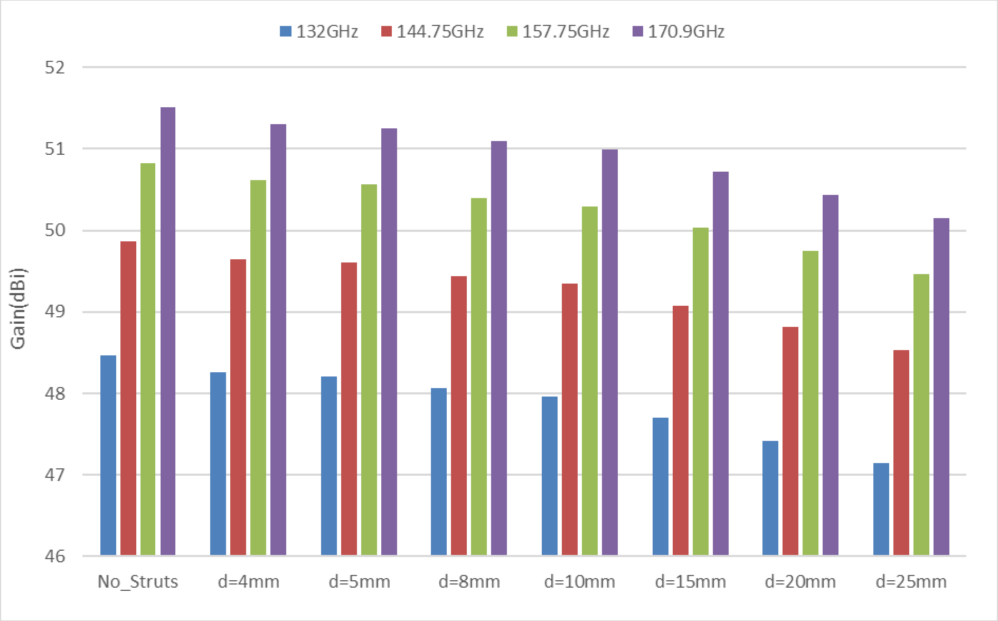

Figure 37: CAC3CS design, circular conductive struts analysis Gain results

The effect of dielectric strut material instead of conductive has been also examined. The dielectric material that has been selected as a realistic approach is the Polyamide (PA) (er=2.3, loss tangent=0.0033, values given in literature) similar material we plan to use in WP5 for the implementation of LENS antennas (section 3.2) with low dielectric permittivity. The simulations of dielectric struts have been carried out for the case of strut diameter 25mm (as a worst-case scenario) and it has been compared with the respective PEC strut and no-strut designs ((indicative results for CAC3CS are shown in Table 36)

Conclusions for struts materials analysis

A general conclusion is that PEC material is slightly better compared to the dielectric one especially in terms of Gain. More specifically, for CAC3CS antenna the Gain in the case of dielectric strut is slightly degraded compared with the PEC case at most frequencies from 0.05-0.33dB. In terms of X-pol and SLL similar performance with PEC case is noticed. Similar conclusions can be made for the case of CAFPXM antenna (though not presented here). More specifically the Gain is degraded for the case of dielectric struts compared to the PEC case by 0.16-0.28dB. The X-pol and SLL are of similar values for both struts materials cases.

Table 36: CAC3CS design strut material comparison results

F(GHz)	Gain (dBi)			X-Pol (-dB/MAX)			SLL- (-dB) / SLL+ (-dB)		
	No-struts	PEC	DIELECTRIC	No-struts	PEC	DIELECTRIC	No-struts	PEC	DIELECTRIC
132	48.47	47.14	46.81	-28.47	-27.74	-27.23	-14.67/ -14.6	-13.43/ -13.84	-12.47/-13.89
144.75	49.86	48.53	48.67	-33.07	-32.32	-32.35	-14.8/ -14.8	-13.62/ -13.89	-14.21/--13.66
157.75	50.82	49.46	49.30	-31.86	-31.1	-31.07	-14.97/ -14.92	-13.69/ -14.04	-12.69/--14.72
170.9	51.51	50.15	50.10	-29.07	-28.3	-28.31	-15.22/ -15.2	-13.86/ -14.37	-14.31/--13.65

Surface inaccuracy

Another critical parameter which needs to be considered and has fairly been analysed in past at reflectors antenna theory is the reflector's surface accuracy. Ruze has shown [8] that an RMS surface error δ, leads to a reduction of the antenna gain by a factor ε_{surf} given by:

$$\varepsilon_{surf} = e^{-(\frac{4\pi\delta}{\lambda})^2},$$

(6)

where λ is the wavelength of the incident radiation. Equivalently, the above equation expressed in dB (gain loss due to reflector surface accuracy) reads

$$\varepsilon_{surf}^{dB} = -685.81\left(\frac{\delta}{\lambda}\right)^2$$

(7)

The equation and the gain loss due to reflector surface accuracy is depicted in Figure 38. It can be seen that an RMS error of δ=λ/10 can significantly degrade Gain by almost 7dB. Even a slight surface error of λ/25 can degrade Gain by 1dB. This is the theoretical prediction of Gain loss due to surface error. Additionally surface error can affect cross polar and other far field parameters. These effects have been studied for the HGA OFFC3CS design. Various values of RMS surface error have been examined using TCRA GRASP simulations and the far field results have been recorded (see Figures 31-34). A wavelength of 2mm (as average wavelength for D-band) has been used. It can be seen that in order to have antenna gain close to the one given by the ideal reflector surface, the surface error needs to be equal (or less than) λ/100, any values higher degrade Gain performance. In terms of Cross-polar similar notification can be made. Also, for values of surface error λ/10 and higher the cross-polar is severely affected and the CP is becoming elliptical to linear. SLL are not affected by surface errors. Similar notifications can be made for the main reflector of the Cassegrain antennas.

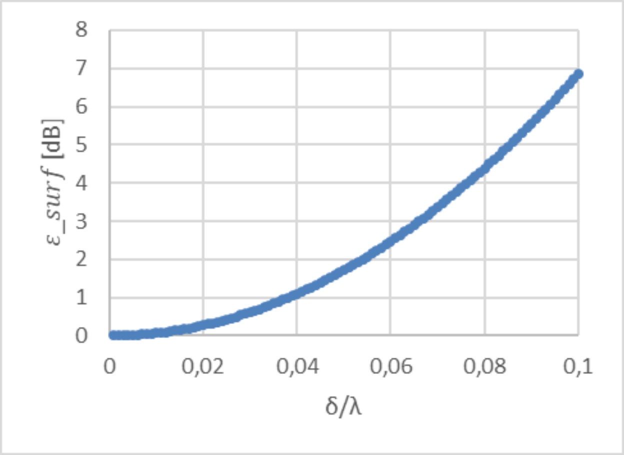

Figure 38: Gain loss (theoretical) due to reflector surface accuracy (δ/λ)

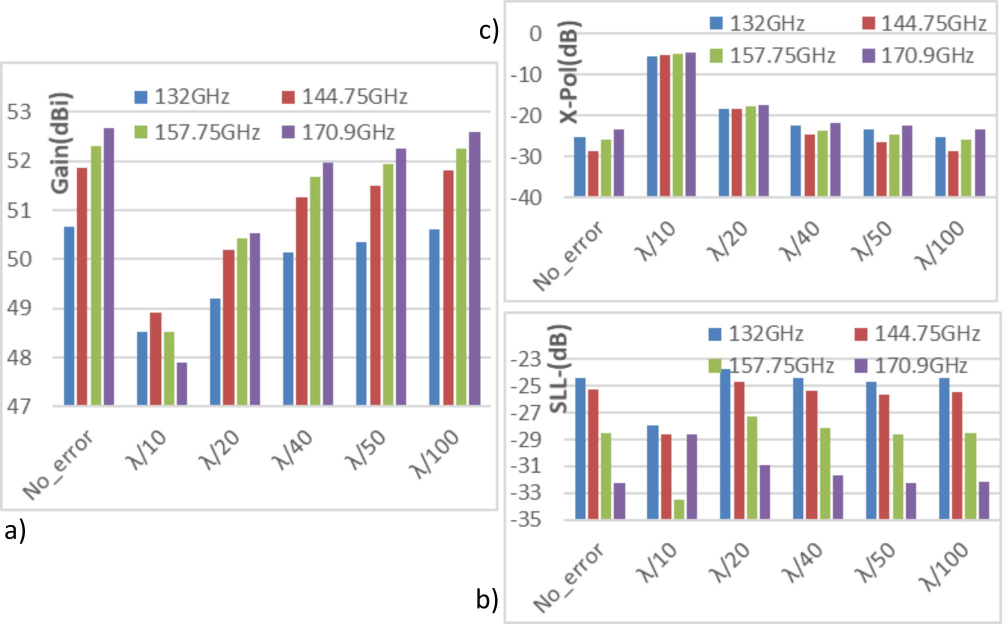

Figure 39: RMS surface error (in fraction of λ) effect on a) Gain, b) X-pol and c) SLL for OFFCECS design

3.2 Medium Gain Lens Antennas

3.2.1 Ellipsoid dielectric lens antenna design

In the framework of WP3 research on the design of D-band MGAs, the development of a dielectric lens antenna with beam steering functionality was studied. The aim is to utilize the technology of dielectric lens antennas in WP5, and in particular, in the indoor scenario (2nd demonstrator: “A metasurface point-to-point non-LOS demonstrator”) as described in D5.1.

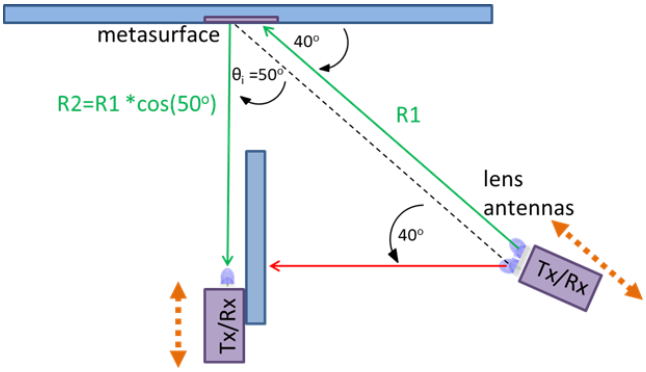

Figure 40: Topology of the indoor non-LOS demonstrator

In this Deliverable we describe the initial design and simulations aiming to prove the functionality of the proposed lens antenna regarding the requirements of the specific demonstration. The final detailed design and implementation will be carried out in WP5. The initial performance requirements are an antenna gain of about 26 dBi and the ability to cover an angle of about 40 deg by beam-switching. These requirements have been derived using the propagation loss equation (14) in Section 4.1 of this deliverable, assuming a total propagation path of 10 m, a metasurface efficiency of 90 % and an area of 10 x 10 cm^2.

The theoretical basis of the proposed ellipsoid dielectric lens antenna design was described in **[11]**. The approach is to tilt a collimated beam lens about its central focal point (feeder’s phase center) for beam-steering. The feed horn is chosen to be stationary, in order to dispense with expensive and error-prone millimeter-wave rotary joints. Based on this idea, we have introduced a system of two tilted lenses (dual-lens concept) each of which is fed by a separate feed-horn via an RF-switch included in the RF-front-end of the transceiver (Figure 41). The tilt angle was chosen to satisfy the requirement of beam-switching of 40 deg consistent with the NLOS demonstrator plan.

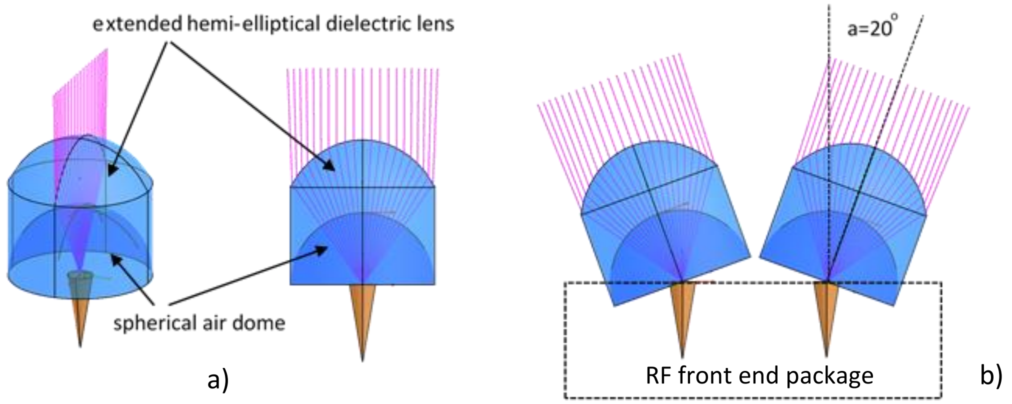

Figure 41: Dielectric lens antenna design concept a) Single lens non-tilted, b) Dual-lens concept

A series of parametric simulations have been conducted using the ANSYS HFSS electromagnetic simulation software. The lens material that has been used in the simulations is Teflon (Er = 2.08, tanδ = 0.001)

The initial lens design, D1, was closer to the theoretical geometry (Figure 42a). This model has been used to optimize the geometric parameters of the design to satisfy the antenna performance requirements. A modification of this model has been developed (D2) as shown in Figure 42b, which aims to simplify the manufacture of the lens prototypes.

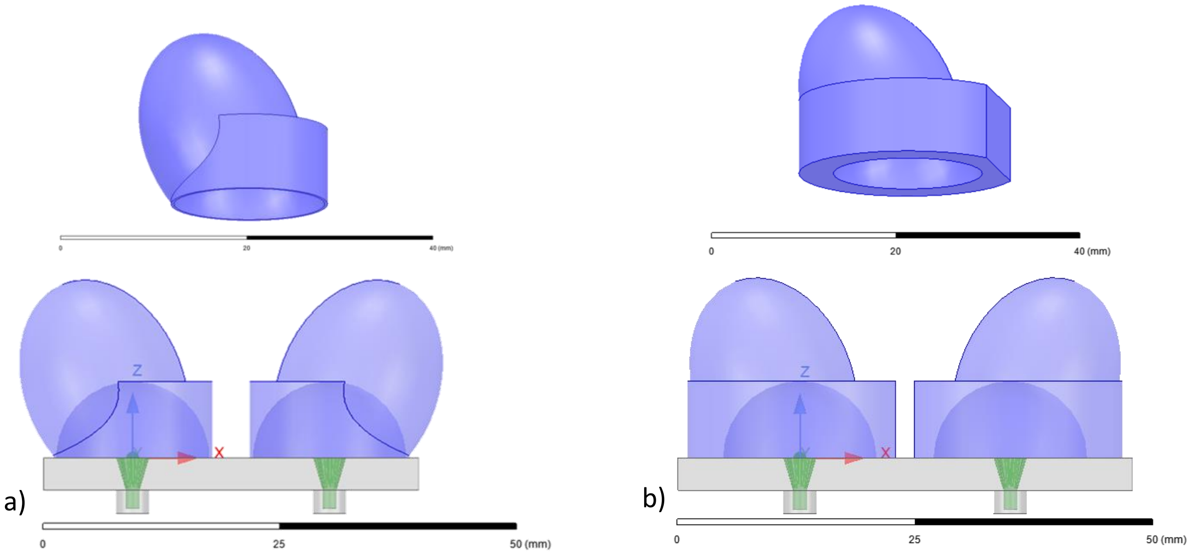

Figure 42: Dielectric lens models a) D1 (Ideal design) for EM performance optimization, b) D2 (Practical design) for prototyping optimization

A comparison of the simulated gain radiation patterns of the ideal (D1) and practical (D2) design for a physical tilt angle of 22 deg is shown in Figure 43. It shows that there are no significant differences between D1 and D2 in the main lobe. It indicates that D2 can be used instead of D1, maintaining expected performance but simplifying the fabrication.

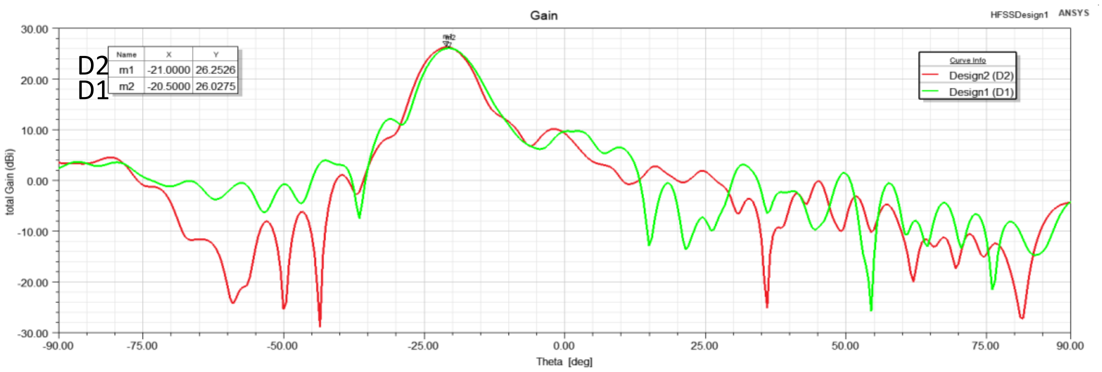

Figure 43: Comparison of radiation performance (Gain) between lens antenna designs D1 and D2

The conical horn C3 presented in section 3.1.3 has been used as the feeder of the lens antenna. Significant degradation of S11 was noticed (Figure 44) compared to the feed horn without the dielectric lens though it still yields acceptable matching performance (below -10dB) in the frequency bandwidth of interest.

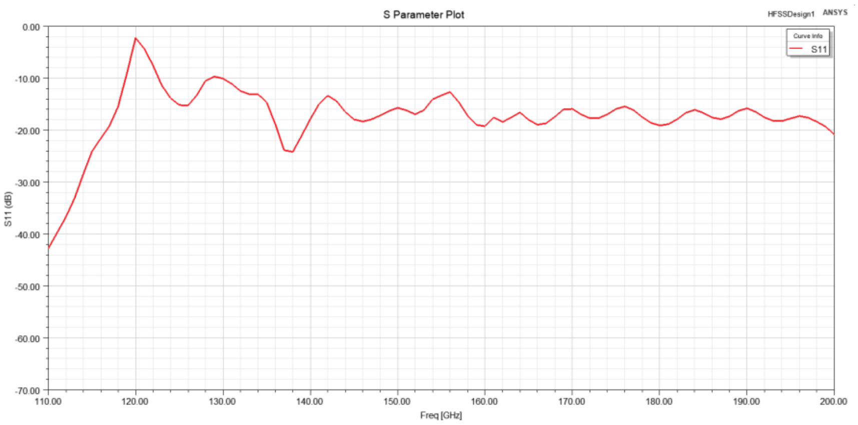

Figure 44: Reflection coefficient of D2 (S11 Simulations results)

A single ellipsoid lens antenna (D0) that was not tilted, has been also designed. This design has the same design parameter values as D2 except that the steering angle is 0 deg. In Figure 45, the radiation pattern of the feed horn C3 is presented with and without the use of the D0 lens on top. This resulted in an increase of the antenna gain by more than 14dB.

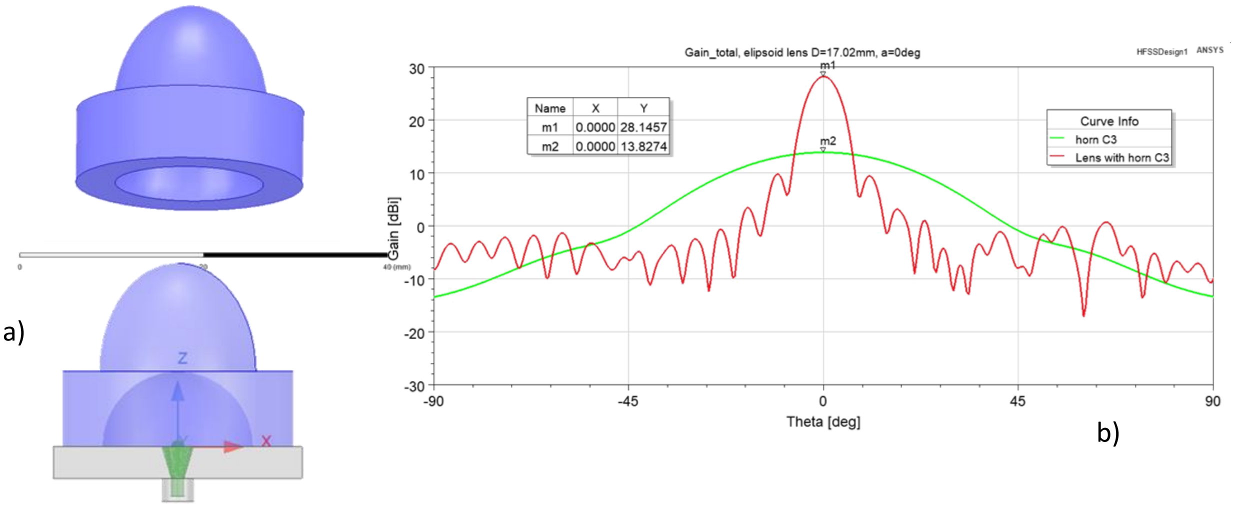

Figure 45: a) Tilt-0deg ellipsoid lens antenna design (D0), b) Radiation pattern of no-lens and lens case with C3 feed horn

Parametric analysis

The basic design parameters of the dual lens antenna system are presented in Figure 46. The values of these parameters for the D2 design have been derived through corresponding parametric analysis.

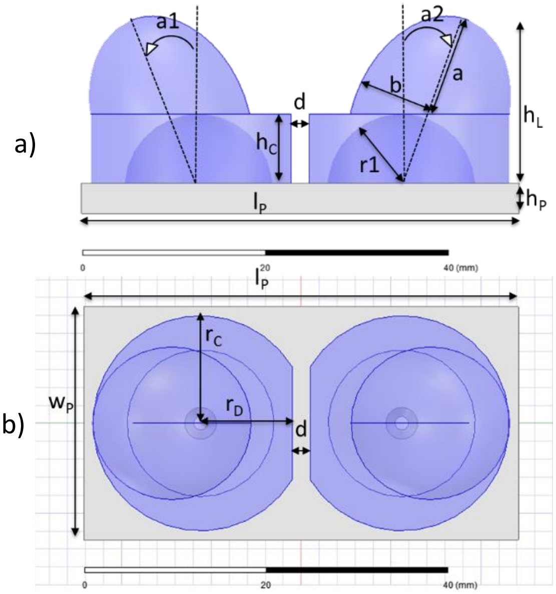

Param.	Value
a1	-22°
a2	-22°
a	11.81 mm
b	8.51 mm
d	2.00 mm
h_C	8.19 mm
h_L	18.54 mm
h_P	3.40 mm
r1	8.19 mm
l_P	48.33 mm
r_C	10.19 mm
r_D	11.97 mm
w_P	25.95 mm

Figure 46: Basic design parameters of the dual lens antenna system (D2), a) side and b) top view

The distance *d* between the lenses has been varied from 1λ up to 2λ to find an acceptable value. The antenna gain pattern results are depicted in Figure 47. The main lobe is similar for all cases, only the side lobes vary, though of no practical relevance. However, larger distances would yield higher side lobes especially towards the side of the neighboring lens. As a result, the distance of 2 mm was selected in order to achieve an acceptable performance and size reduction.

The mechanical steering angle vs. the electromagnetic angle are compared in the Figure 48. Mechanical angles from 20° to 22° lead to steering angles from 19.5° to 21°, hence, meeting the application requirements of the demonstrator of WP5. The gain remains nearly constant for all investigated angles at approximately 26dBi. The selected mechanical angle was 22° (steering angle 21°) but may be chosen to be smaller in the final design.

The comparison of three channels within the D-band for the selected mechanical steering angle of 22° is summarized in Figure 49. The angle of maximum antenna gain for all the three channels were selected between 20.5° and 21°. For this parameter set, the antenna gain increases with increasing frequency as expected.

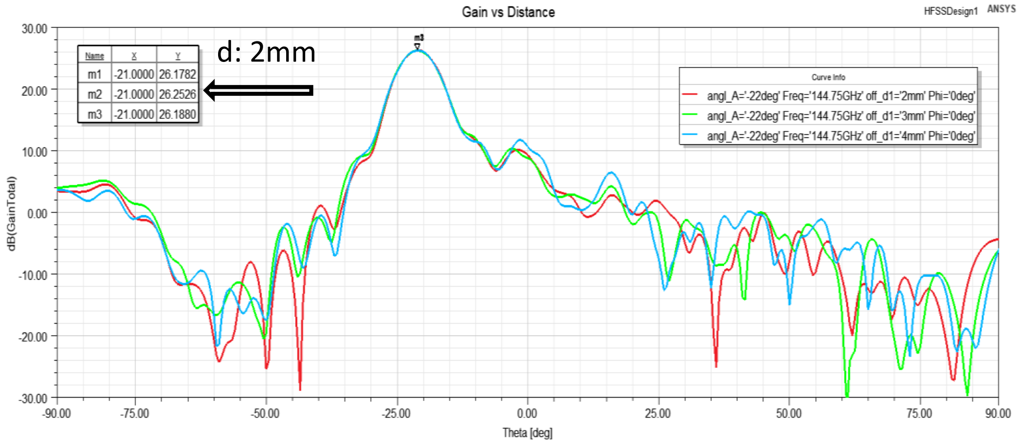

Figure 47: Parametric study of gain pattern vs lens distance

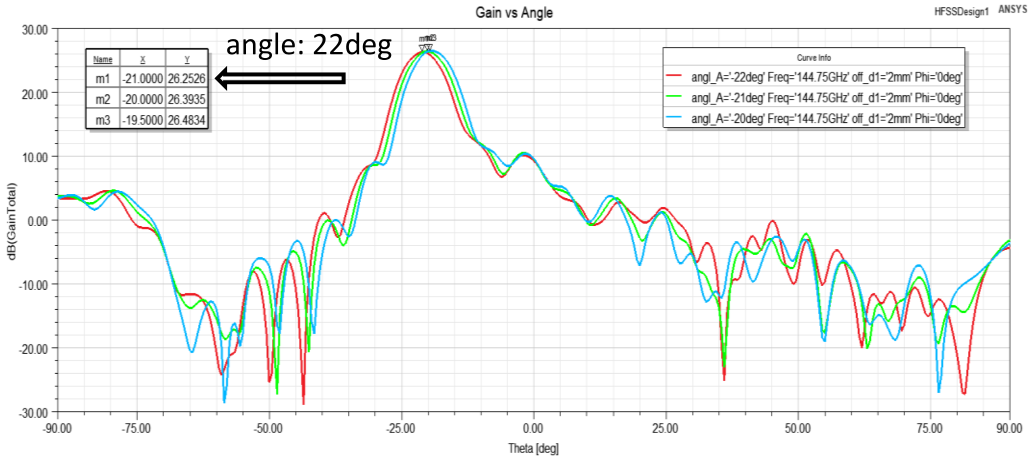

Figure 48: Comparison of mechanical vs. electromagnetic steering angle

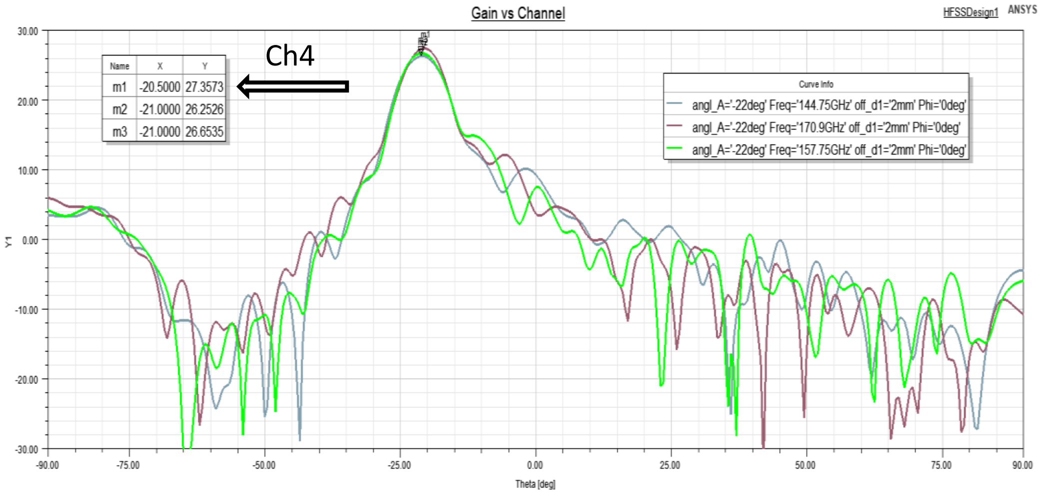

Figure 49: Analysis of radiation patterns for different D-band sub-bands.

Sensitivity analysis

A sensitivity analysis on the variation of the dielectric permittivity (εr) variations was examined. The results are depicted in **Figure 50**. For the D2 design, assuming εr = 2.08 (steering angle 21°), the antenna gain in the direction of interest rapidly decreases as εr increases.

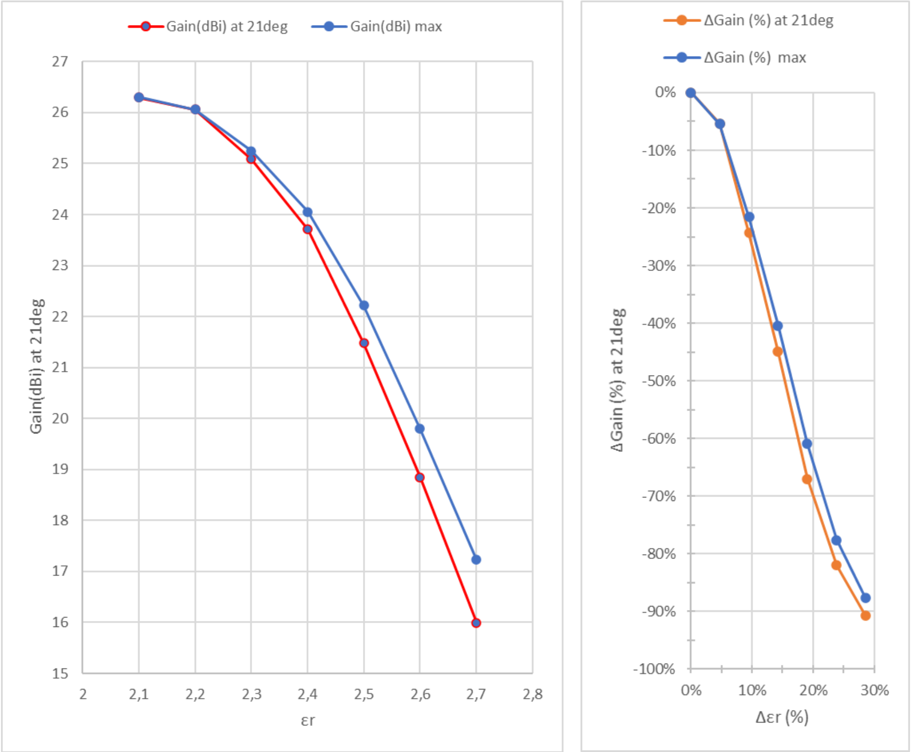

Figure 50: Sensitivity of the lens antenna gain vs. the permittivity (εr) of the lens material a) antenna gain vs εr, b) Δgain (%) vs Δεr (%)

3.3 Steered-beam reflectarray antennas based on liquid crystal technology

3.3.1 D-band prototype fabrication

As a proof-of-concept for demonstrating the liquid crystal technology in steered-beam antennas, the W-band antenna described in section 6 of Deliverable 3.1 has been manufactured. The fabricated antenna has 3 main components: (1) the feeder, (2) a mechanical structure, which includes a passive reflector emulating one state of the reflectarray, (3) a reflectarray with electronic control for dynamically adjusting the phase in reflection as a sub-reflector.

The feeder is a commercial horn from ERAVANT (17 dB of gain) with circular waveguide input. This input is connected to a WR-10 transition from Flann Microwave. The horn is fixed using a fine tuning mechanism in order to adjust the position along the axis of the horn, as can be seen in Figure 51(a). The antenna system comprises two parabolic reflectors that share a common focal point (the main reflector and a sub-reflector) and a tunable reflectarray antenna that feeds the sub-reflector with the appropriate and controllable wavefront.

To achieve the aim of validating the optics of the proposed structure, the reflectarray has been replaced in a first step by a third parabolic reflector which emulates a fixed state of the reflectarray. This reflector can be easily interchanged by the supporting structure of the reflectarray, as can be appreciated in Figure 51(b). The whole structure has been fabricated using aluminium in a high-precision external workshop. A dimensional certification has been done for both, the local dimensions of each component and the relative position between them. In all the cases the deviations are smaller than 17.1 micron, with an average error of 0.1 micron. In the case of the feeding angle, the error is smaller than 0.02 degree. Figure 52 shows some examples of the dimensional analysis.

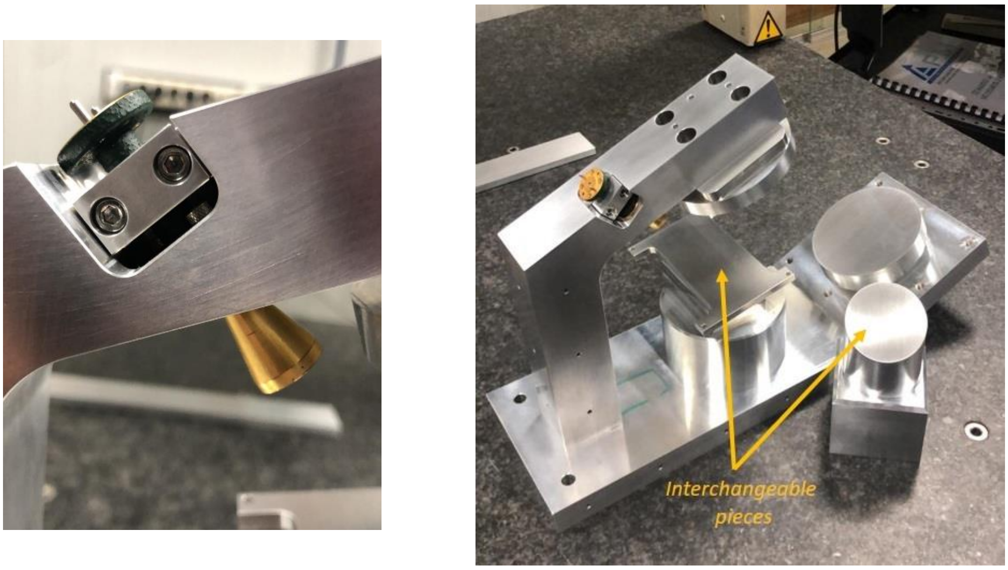

(a) (b)

Figure 51: Detail of the mechanical structure of the proposed confocal antenna (a) Feed horn positioning (b) Whole structure, including interchangeable passive reflector and reflectarray flat support.

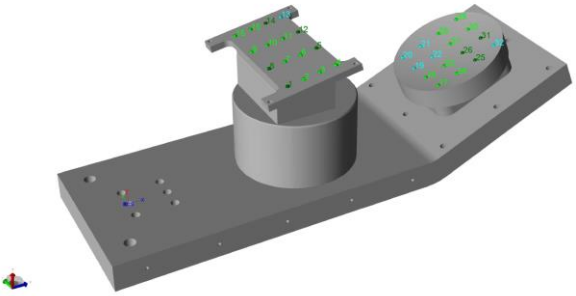

Verification Mode	Surface
Deviation Max	0.0131 mm
Deviation Mean	-0.0001 mm
Deviation Min	-0.0166 mm

(a)

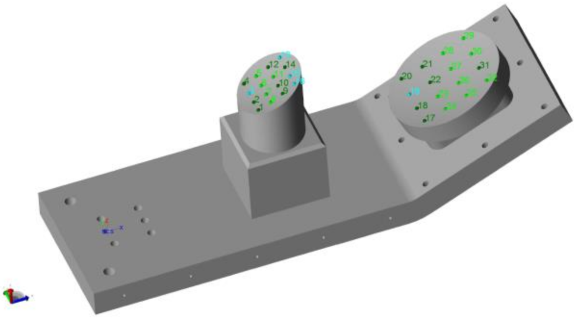

Verification Mode	Surface
Deviation Max	0.0172 mm
Deviation Mean	0.0000 mm
Deviation Min	-0.0168 mm

(b)

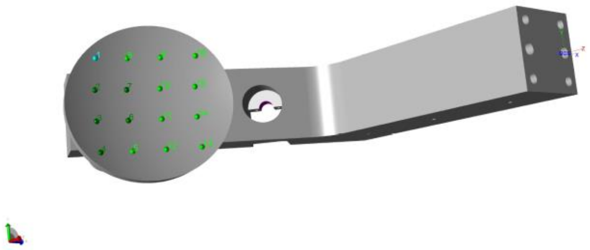

Verification Mode	Surface
Deviation Max	0.0162 mm
Deviation Mean	0.0001 mm
Deviation Min	-0.0125 mm

(c)

Figure 52: Example of the dimensional verification for the mechanical structure.

The reconfigurable part of the proposed antenna has been fabricated in-house using a photolithographic process. The segmented ground has been fabricated using conventional PCB technology on a FR4 substrate, instead of the conventional glass. Each patch forming the segmented ground has a via-hole which is connected to a back layer, which directs each connection to a socket. As detailed in previous deliverable, the reflectarray is controlled using 4 sockets, each one controlling one quarter of the antenna. The dipole array has been etched on a 40 micron quartz sheet and was allocated at a 45 micron distance from the segmented ground, forming the cavity in which the liquid crystal is injected, in this case the GT3-23001 from MERCK. All the dipoles are interconnected in order to have the same voltage reference, while the voltage is varied locally at each patch of the segmented ground. This strategy allows to independently controlling the voltage of each pixel, and therefore to steer the beam to any direction in the full 2D space. It is worth noting that both FR4 and direct addressing have been implemented for the first time in liquid crystal reflectarray antennas. Figure 53 and Figure 54 show the details of the fabricated reflectarray for front and back, respectively.

Figure 53: Detail of the LC-RA showing the pixels made of an array of four dipoles.

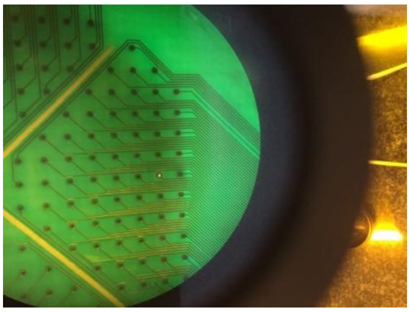

Figure 54: Detail of the back part of the LC-RA. The control lines and bias for direct addressing can be appreciated.

3.3.2 Preliminary measurements for W-band prototype

The first step for the experimental validation of the antenna consists in an accurate characterization of the fabricated reflectarray. It consists in extracting the effective permittivity of the LC for the frequency of interest, as well as the dependency of the phase in reflection towards the applied voltage. The measuring setup is shown in Figure 55(a). All the pixels forming the reflectarray are connected to the same voltage by short-circuiting the four sockets. Two horns are used to measure the antenna in transmission (S21) when the reflectarray is illuminated with a 3dB decay in the borders. For this reason two lenses have been included. The horns have the same polarization as the dipoles. Figure 55 shows the setup of the measuring system, as well as the measured phase in transmission as a function of the applied voltage (from 0 V to 26.5 V), which in the case of GT3-23001 corresponds to an effective permittivity variation from 2.43 to 3.2, with tanδ variation in the range from 0.013 to 0.006. The extracted information in terms of voltage and effective permittivity, which have a non-linear relation, is used to synthetize the voltage value at each pixel.

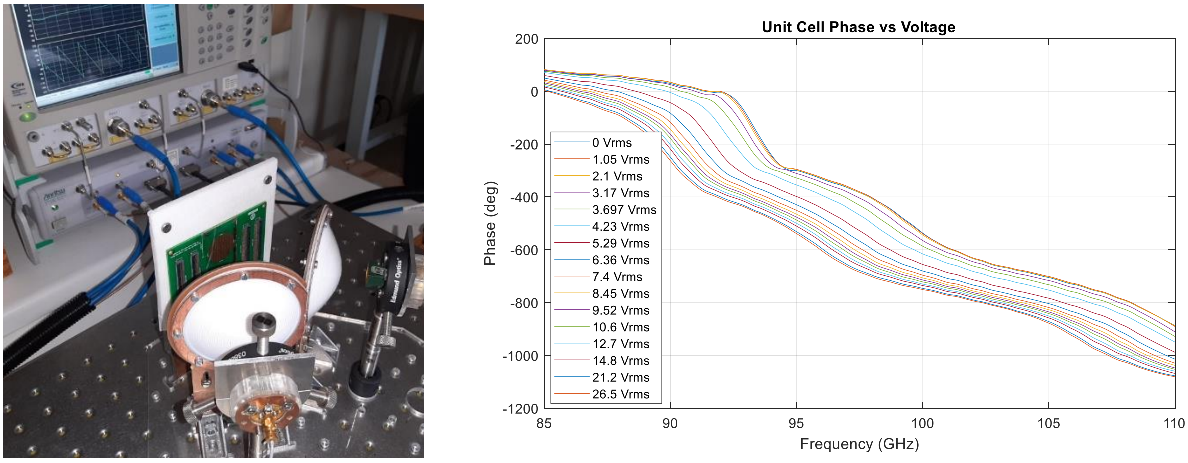

(a) (b)

Figure 55: Characterization of LC-RA in the quasi-optical bench. (a) Setup. (b) Measured phase as a function of applied voltage, in the frequency range from 85 GHz to 110 GHz.

Before measuring the antenna with the LC-RA, first measurements have been performed in the anechoic chamber by replacing the RA support by the passive sub-reflector. The main cuts of the antenna were measuring using the compact range system at UPM's anechoic chamber at 100 GHz, see Figure 56.

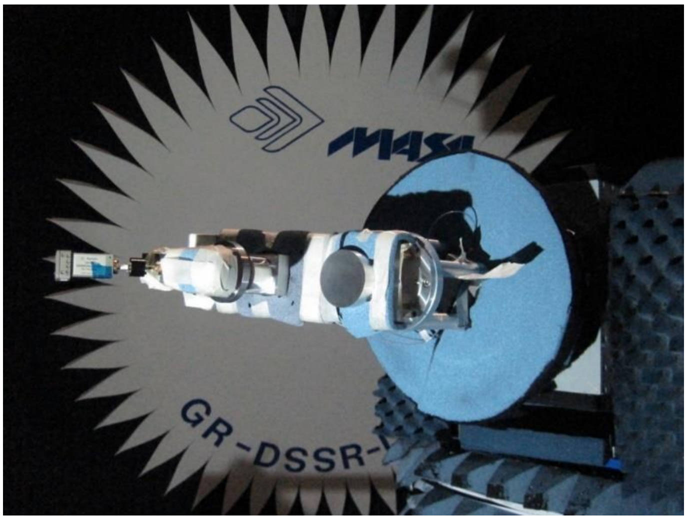

Figure 56: Antenna with passive sub-reflector in the anechoic chamber.

Figure 57 shows the main cuts of the measured radiation pattern compared to two simulations, one using GRASP and a second one using CST. The second simulator includes a detailed modeling of the feeding horn, while in the first simulator only the feeding aperture has been defined. The results are in agreement with the expectations from theoretical simulations (GRASP and CST softwares), although a small de-pointing in the 90 deg plane which can be easily compensated with the LC.

The next step was to integrate the characterized LC-RA into the confocal antenna. For this integration, the modular DC control circuits and associated software based in LabView has been already designed, manufactured and tested.

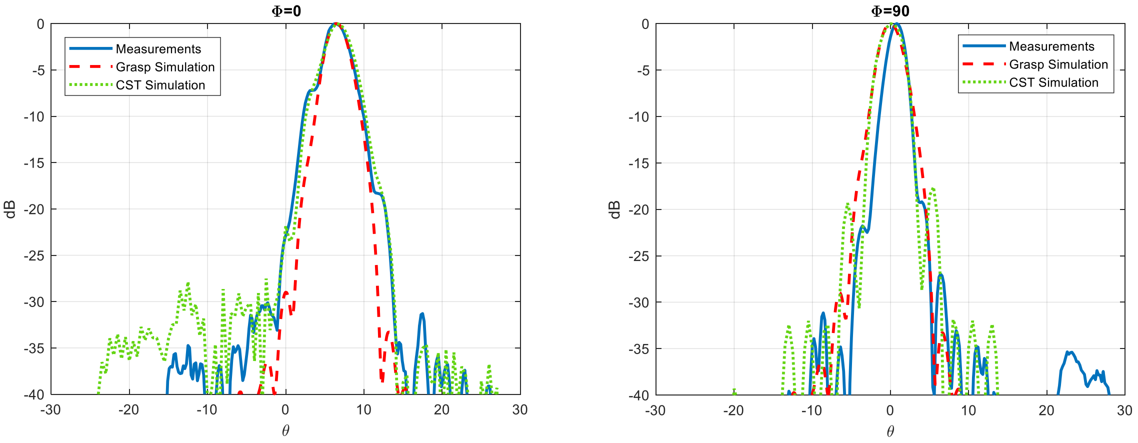

(a)

(b)

Figure 57: Measured radiation pattern for the passive sub-reflector configuration

(a) f=0º (b) f= 90º.

3.3.3 Dual-polarization extension

This section is focused on the design of a LC unit cell capable to reflect a dual linear polarization with an appropriate phase-shift, which can be part of a reconfigurable reflectarray. The wafer is an extension of the reflectarray cell with single linear polarization using multi-resonant dipoles geometry. This extension increases the complexity of the analysis, as the constrains to be satisfied are extended to dual polarization, where having an almost independent response for each polarization is very challenging. The reflection not only must minimize the losses as much as possible, but a proper phase range with smooth and linear variation, have to be carried out for two polarizations with different propagation characteristics, avoiding the coupling from one polarization to the other. These demanding constrains difficult the design process, especially when using a segmented ground plane. That is why this latter was not considered here, so that a 1-D beam steering capability will be finally performed.

The use of a segmented ground plane would allow to perform a 2D beam steering, while the proposed continuous ground plane and a voltage addressing by rows only allows the steering in one plane (1D). Thus, the gain will decrease for the same size of the array. Moreover, spurious resonances and a clear degradation of the linear behaviour is caused when the impinging wave arrives in oblique incidence, so the difficulty to manage these effects leads to the use of a continuous ground plane.

3.3.3.1 Unit Cell Design

To achieve a dual polarized unit cell, several reflectarray element topologies are proposed in the literature, for circular polarization, for instance squared or circular rings [12], [13] , omega-shaped elements [14], or more complex shapes such as the named cross-bowtie element [15]. Regarding linear polarization, the squared patch topology (as in [16]) has the disadvantage of the single resonance, which does not allow to properly shape the frequency response in a suitable bandwidth, being necessary a multi-stacked structure to achieve multiresonance. In [17] a single layer cell with crossed elements is used to achieve two resonances, however, the dimensions imposed by the topology, where one element has to be contained by the other one, introduces a dual band operation instead of enlarging the bandwidth. Therefore, the previously preferred option of a single layer multiresonant topology using parallel dipoles is then extended to its use for dual polarization, so a second orthogonal set of dipoles is introduced. In Figure 58 the structure of the unit cell is depicted. Two main differences are introduced with respect to the previous design, the continuous ground plane, that in this case covers the whole cell and the metallization structure, where a second set of dipoles are introduced to resonate with the orthogonal linear polarization. Once the resonant structure is achieved, the dimensions of each set of dipoles is adjusted to reach the desired response. In this case, the phase curves of both polarizations are adjusted to be as close as possible, with the initial objective of having the same response (and thus, the same beam pointing) for both polarizations.

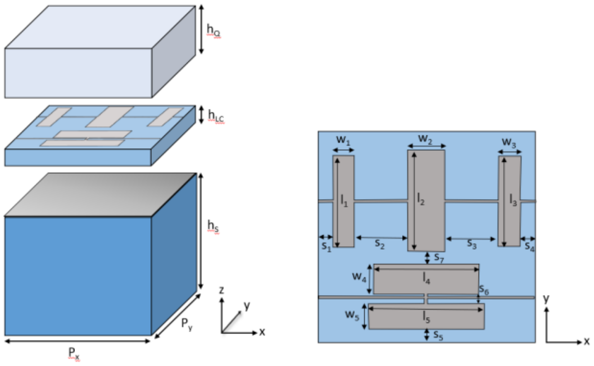

Figure 58: Unit cell for dual linear polarization. Left: Layer structure; Right: Top view

In Table 37 and Table 38 the dimensions of the resonant metallizations are collected, as well as the thickness of each layer. Table 39 summarize the tolerances of the design, having similar values to those exhibited in the single polarization cell.

Table 37: Design parameters. Dual linear polarization cell

Parameter	Dimension	Value(mm)
Px=Py	Unit Cell Period	1.5
l_1	Dipoles length	0.703
l_2		0.785
l_3		0.703
l_4		0.733
l_5		0.805
w_1	Dipoles width	0.22

w_2		0.26
w_3		0.22
w_4		0.265
w_5		0.12
s_1=s_4	Dipoles separation	0.07
s_2= s_3		0.33
s_5		0.065
s_6		0.13
s_7		0.06

Table 38: Layer structure parameters. Dual linear polarization cell

Layer	Thickness (mm)	Material	Properties
Liquid Crystal	0.073	GT3-23001	$\epsilon_{\perp} = 2.47;\ \ \delta_{\perp} = 0.02$ $\epsilon_{\parallel} = 3.27;\ \ \delta_{\parallel} = 0.015$
Superstrate	0.43	Quartz	$\epsilon = 3.38;\ \ \delta = 0.003$
Substrate	2	Silicon	$\epsilon = 4;\ \ \delta = 0.007$
Metallizations	-	Gold	$\sigma = 45.5\ x\ 10^{6} S/m$

Table 39: Dual polarized unit cell design tolerances (±30º)

Parameter	Dimension (mm)	Tolerance(µm)	Tolerance (%)
LC layer thickness (h_{lc})	0.073	4	5.5
Quartz layer thickness(h_Q)	0.43	30	7
Cell period (Px=Py)	1.5	120	8
Dipoles width (w)	0.12-0.26	20	8-16
Dipoles length (l)	0.703-0.805	5	0.7

3.3.3.2 Unit Cell Performance

After the optimization process, once again the cell must be evaluated. In this case, the cell is directly optimized for the central angle of incidence of a realistic reflectarray (θ=30º, φ=270º). In Figure 59 it is shown the reflection coefficient in amplitude and phase for both vertical and horizontal polarizations. It can be observed a smoother response than in the single polarization design, where the segmented ground plane causes the aforementioned spurious resonances and antiresonances. However, although the design is performed by controlling only two resonances for each frequency to have similar response for both polarizations (horizontal polarization presents two of three dipoles with equal length), we can find a third resonance out of the band at that angle of incidence, which is produced by the oblique incidence on the more complex metallizations layer. The operating frequency band can be defined from 95 GHz to 107 GHz, which implies approximately a 12% bandwidth, however, the preferred instantaneous bandwidth, where the design is optimized is from 95 GHz to 100 GHz being a 5% bandwidth.

The phase range obtained is around 300º, which is lower than the ideal 360º although it allows a correct operation of the unit cell. Higher phase range can be obtained by decreasing the thickness of the LC layer, but at the expense of sharper resonances and higher losses. Also, we can see a very good correspondence between vertical and horizontal polarization (in Figure 60 it can be seen in detail), which would be a requirement if the reflectarray has to point the beam equally for both polarizations. Although it could be unnecessary if both polarizations are controlled independently, it is also convenient to facilitate the voltage addressing process and to ensure similar performance between them.

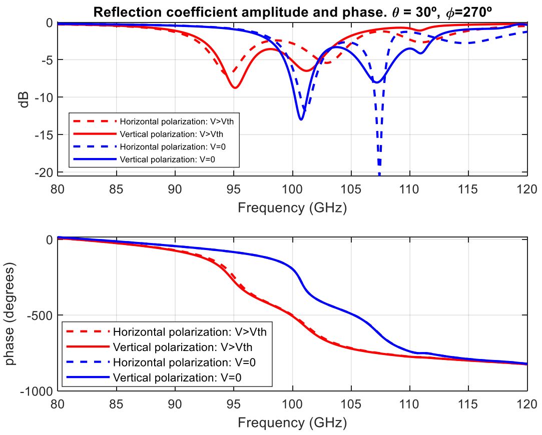

Figure 59: Reflection coefficient of the unit cell. Angle of incidence: Θ=30, ϕ=270.

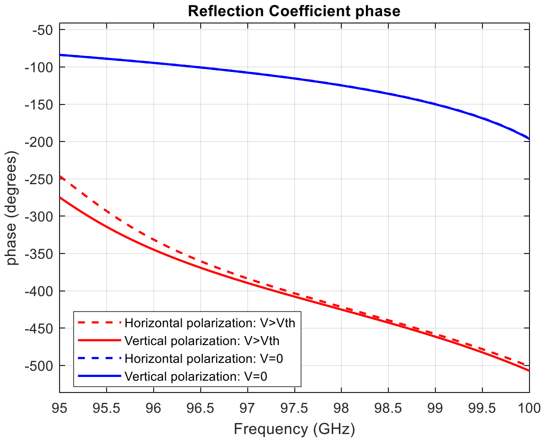

Figure 60: Zoom in reflection coefficient phase. 95GHz to 100 GHz. Angle of incidence: ϴ=30, ϕ=270.

Some of the intermediate states are shown only for vertical polarization in Figure 61 (horizontal polarization shows equal behavior), for a different angles of incidence, only to show the low degradation of the response contrarily to the behavior of the segmented ground plane cell. In Figure 62 the voltage dependence of the phase-shift is shown for different frequencies (shown each in red, blue and black-grey tones each), two angles of incidence (differentiated by a different tone and circle vs squared marker) and for both polarizations (differentiated by solid or dotted line).

We can see that the difference between polarizations is higher at the extreme frequencies of the optimum bandwidth (95 GHz and 100 GHz). However, the most important conclusion is that the angle of incidence changes significantly the phase shift (being the angle θ the most important variable that affect the electrical behavior at a certain angle).

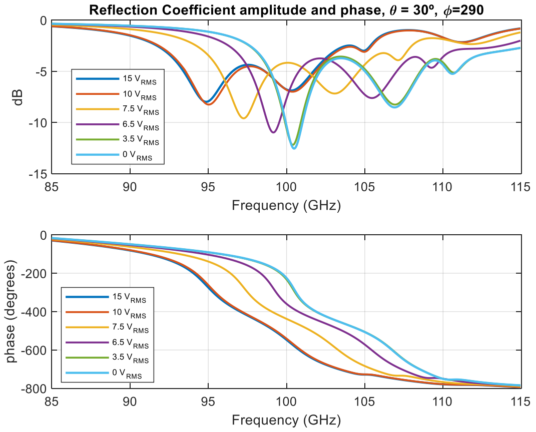

Figure 61: Reflection coefficient for vertical polarization of the unit cell. Amplitude and phase. Angle of incidence θ=30º, ϕ=290. Intermediate states.

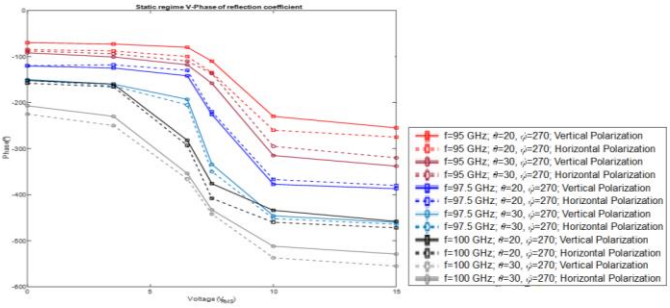

Figure 62: Simulated phase shift vs Voltage for different frequencies, angles of incidence and both polarizations

3.3.3.3 Unit Cell Modelling for Dual Polarization

The purpose of this section is to establish if the unit cell designed for dual polarization can be biased in such way that the cell introduces a different phase shift for each polarization. This demonstration enables the idea of a reflectarray capable of pointing two different beams with different polarizations, which is a novelty in the field of reconfigurable reflectarrays using LC. The analysis of the effect of the inhomogeneity of the cell is similar to that carried out in the linear polarized cell, so the space between the closer dipoles of both polarizations is analyzed in electrostatic simulation.

For this simulation, we have considered a case where one of the polarizations with a phase state of high bias voltage could affect the other polarization with a low bias voltage. As we can see in Figure 63 and Figure 64, the regions of the LC under each dipole are correctly biased (with the potential and field lines expected) but the region in between suffers from a non-homogeneous field, product of the interference between the biasing of both polarizations.

Consequently, in addition to the modelling of the effective biasing area considered in the previous analysis, it is necessary to consider an intermediate area whose biasing depends on the values of the voltages applied for each one of the two polarizations.

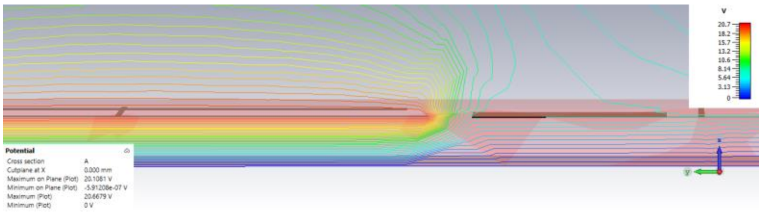

Potential
Cross section A
Cutplane at X 0.000 mm
Maximum on Plane (Plot) 20.1081 V
Minimum on Plane (Plot) -5.91208e-07 V
Maximum (Plot) 20.6679 V
Minimum (Plot) 0 V

Figure 63: Isolines of the potential in x constant cut in a reflectarray cell for 20V (left dipole) and 5V (right dipole) biasing

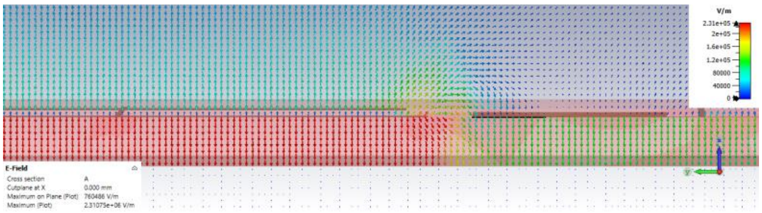

E-Field
Cross section A
Cutplane at X 0.000 mm
Maximum on Plane (Plot) 760486 V/m
Maximum (Plot) 2.31075e+06 V/m

Figure 64: E field lines in x constant cut in a reflectarray cell for 20V (left dipole) and 5V (right dipole) biasing

In Figure 65, we can see the realistic model that considers this situation. The region biased by the voltage applied to the vertical polarization dipoles is represented in orange, whereas that the equivalent area for horizontal polarization in plotted in red; the conflict region is represented in green. We can see that there is only a region of interference. The angles of rotation of the molecules in this region are considered as the mean of those for the independent polarizations.

On the other hand, the simplified model is shown in Figure 66, which just divides the LC in two regions independently controlled.

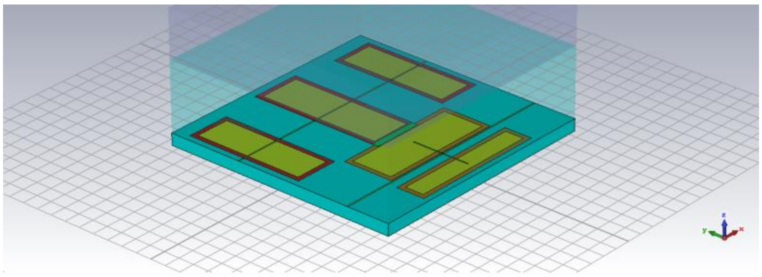

Figure 65: CST view of the unit cell LC regions: Realistic model

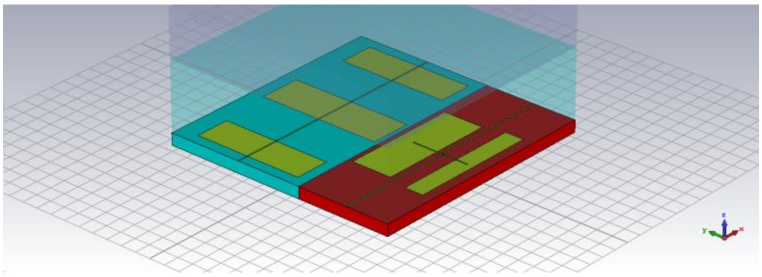

Figure 66: CST view of the unit cell LC regions: Simplified model

In Figure 67 and Figure 68 the comparisons between the results of both models for vertical and horizontal polarizations are shown. We can see a very good correspondence between models, having small differences in amplitude and lower phase difference than the design tolerances for both polarizations. Note that in this case, the extreme states of biasing are shown equally as in the previous case, however these states can be obtained independently for the two polarizations, having 4 possible combinations of phase response (only considering extreme states). As it has been observed that the influence of one polarization phase state over the opposite is negligible, and these curves have also less phase difference than the tolerance, only two-phase curves have been represented for each polarization.

Therefore, we can conclude that: (a) local biasing allows to independently control the reflection coefficient for each polarization, and (b) a simplified model is enough to represent the reflection coefficient of the unit cell in order to perform a reflectarray design.

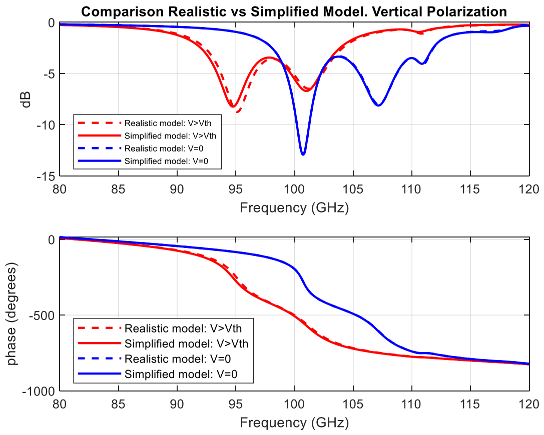

Figure 67: Comparison in obtained reflection coefficient between realistic model and simplified model for vertical polarization. Angle of incidence θ=30º, ϕ=270

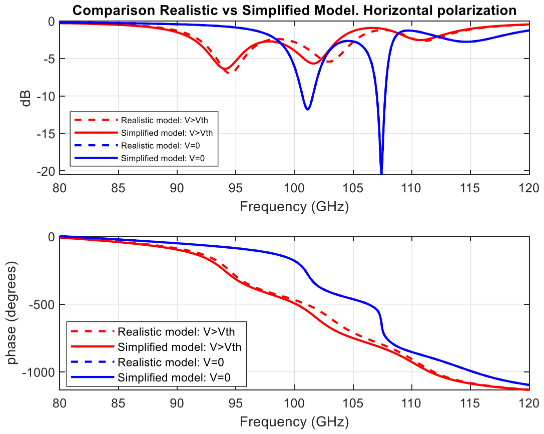

Figure 68: Comparison in obtained reflection coefficient between realistic model and simplified model for horizontal polarization. Angle of incidence θ=34º, ϕ=270

3.3.4 New strategies for improvement of steering time

The relatively large losses and the slow switching times between states are the main weaknesses of such LC-based devices. Even though LC manufacturers are starting to develop novel composites specifically designed to present low losses at microwave and mm-wave frequencies, current mm-wave LC devices provide reconfigurability times in the order of the seconds. However, to be fully implantable in future ultra-reliable low-latency communication networks, improving these times until they are at least comparable to the channel coherence time is of utmost importance due to the stringent dynamic requirements of upcoming communication protocols.

A number of strategies have been reported in optics to improve transition times, such as the use of polymerizable compounds or dual-frequency LC. Another strategy to reduce such times is to employ sophisticated excitation signals by leveraging LC dynamics [18]. In order to understand and completely control its dynamic behaviour during a state transition, which will ultimately impact on the switching time, its accurate temporal modelling is essential. Compared to optics, given the challenge of achieving a proper phase shift range in mm-wave bands, multi-resonant cells must be used. This makes modelling much more complex since resonators create phase shifts that cannot be modelled with a medium constant, and they are also used to locally bias the LC [19]. Previous models are capable of capturing these RF effects in static regime, that is, when enough time has passed after an external excitation so that molecules lie in a stationary state after rotating [20]. In the nematic LC characteristic equation, this translates in neglecting time-dependent terms. Consequently, there is no previous research in accurately characterizing the dynamics of LC-based mm-wave devices to reduce switching times.

In order to improve such steering times, we (i) accurately model for the first time the LC dynamics between transition states (Fréedericksz transition) in RF past the known approximations, in order to obtain a temporal design control capability of the LC, representing a contribution to the previous existing model; (ii) validate the model with experimental measures, implementing a novel measurement setup in a quasi-optical bench; (iii) use that model to design biasing signals intended capable of reducing reconfigurability times by a factor between 2X (decay transitions) - 100X (rise transitions); (iv) validate with experimental measures the temporal improvement. Even though the results have been validated with a reflective surface controlling the phase (metasurface, reflectarray or RIS), the model is extendable to transmissive structures (transmitarrays) or other planar structures capable of controlling other parameters than phase. The model results are validated at the cell (pixel) level for two different frequencies (97 GHz and 102 GHz), which in turn facilitates a tool for the analysis and synthesis of control signals at an arbitrary frequency and per each cell of the whole antenna, given that in a complete surface a plane wave with a different incident angle will arrive to each pixel. Therefore, this tool allows to synthesize overdriving control signals without depending on experimental measurements for each cell and angle of incidence in the array.

$$\overline{\overline{\varepsilon_r}}(\overline{r},t) = \varepsilon_{r\perp}\overline{\overline{I}} + \Delta\varepsilon_r\overline{\overline{N}}(\overline{r},t), \tag{8}$$

$$\begin{gathered}(k_{11}cos^2\theta + k_{33}sin^2\theta)\frac{\partial^2\theta}{\partial z^2} + (k_{33} - k_{11})\cdot \\ sin\theta \cdot cos\theta(\frac{\partial\theta}{\partial z})^2 + \varepsilon_0 E^2 \Delta\varepsilon_q \cdot sin\theta \cdot cos\theta = \gamma_1\frac{\partial\theta}{\partial t},\end{gathered} \tag{9}$$

Equation (8) relates the LC director with the tensorial permittivity of the LC. Equation (9) is the Ericksen–Leslie equation, which relates the electric field excitation with the tilt angle of the director. This equation is typically simplified, which allows to express the tilt angle as a sinusoidal. This way, the rise and decay times can be obtained analytically for low voltage excitations. However, those approximations are not useful in our attempt to improve the switching times, as our biasing signals will require high voltages, regime in which the error committed can be as large as 15%.

To improve that accuracy, we computationally solve Equation (9) using COMSOL Multiphysics [21]. Then, after obtaining the tilt angle along the LC cavity as a function of z and time, we compute the permittivity tensor for each region of the cell and each timestamp. The next step is to use that information in an electromagnetic simulator (CST [22]) to obtain the final phase of a certain transition. Figure 69: Stratified and averaged LC cavity dynamic modelling strategies. In the stratified strategy, εri(θi, t) is computed with Eq. (1) and considering as θi the average tilt within the layer i. In the averaged strategy, εr,avg(θavg, t) is computed considering as θi the average tilt across the entire cavity.. Figure 69 shows two different strategies of modelling the LC cavity (stratified media and averaged media). While the former is slightly more accurate, the latter is much more efficient. In order to choose among them, the convergence analysis shown in Figure 70 is carried out, concluding that an averaged effective permittivity tensor is enough in most of the cases.

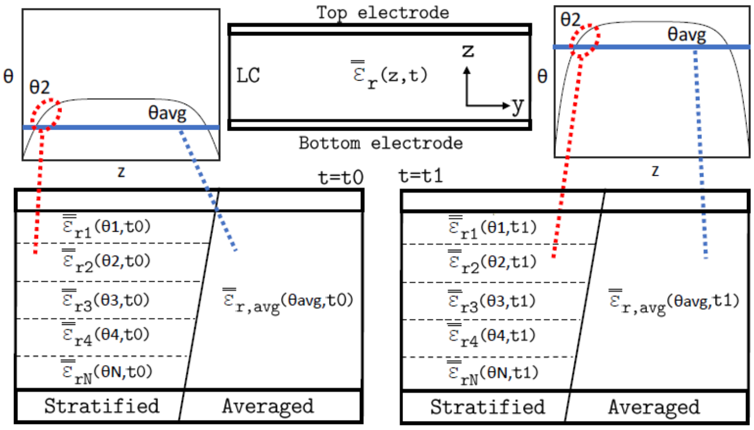

Figure 69: Stratified and averaged LC cavity dynamic modelling strategies. In the stratified strategy, εri(θi, t) is computed with Eq. (1) and considering as θi the average tilt within the layer i. In the averaged strategy, εr,avg(θavg, t) is computed considering as θi the average tilt across the entire cavity.

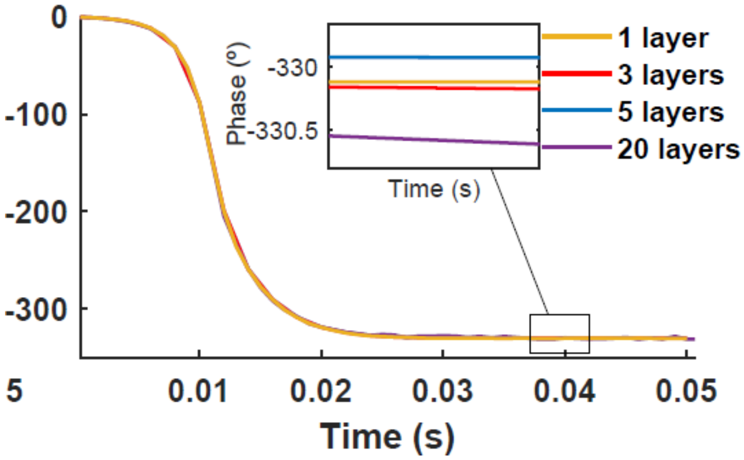

Figure 70: Stratified simulation convergence study at 97 GHz for a transition from 0V to 150V.

Figure 71 shows an illustration of the measured LC-based (GT3-23001) reflectarray antenna used for validation and the measurement setup. The model validation is shown in Figure 72(b), where simulations and measurements of the transient reflected field phase are compared at 102 GHz as a function of time for different voltage rise transitions starting from idle, verifying that the tool can predict relatively close the actual cell behavior. The model has been validated with relaxation measurements as well. Figure 72(c) shows simulation and measurement data of the reflected field phase evolution at 102 GHz for different decay transitions parting from varying voltages. Figure 72(a) shows the driving signals in each case.

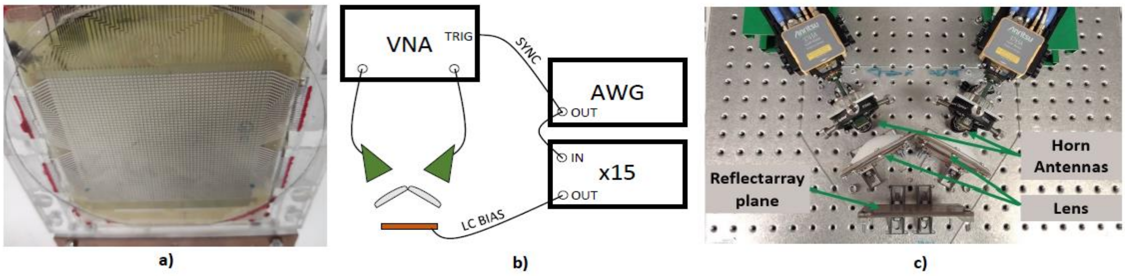

Figure 71: Measurement setup. a) Reflectarray picture b) Block diagram of the setup c) Quasi-optical bench picture

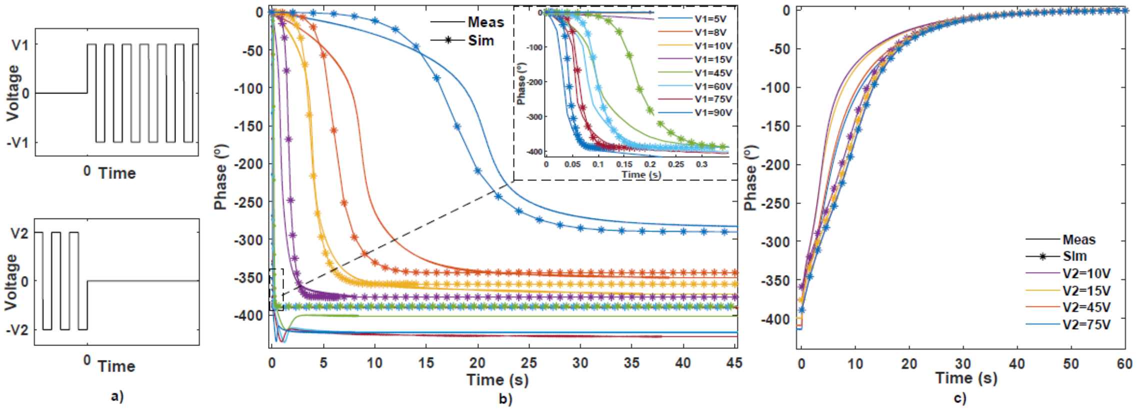

Figure 72: GT3-23001 phase transition dynamics at 102 GHz. a) 1 kHz biasing signal for excitation (top) and relaxation (bottom) dynamics b) Excitation transient phase for different V1 values c) Relaxation transient phase for different V2 values.

This validated dynamic model enables the development of bias voltage design techniques through simulations, which allow an improvement on the antenna reconfigurability times. By overdriving it in the rise transitions, the LC orientation time can be accelerated when the electric field is increased (i.e. rotating the molecules towards parallel to z). This is achieved by using during a short period of time a larger voltage than the nominal biasing voltage (i.e. the voltage in which the cell presents the desired phase shift in permanent regime, after the molecules stopped rotating). This can be seen in Figure 73. The design procedure of the LC overdriving signal for quickly achieving the desired phase of an array cell is the following: 1) Identify the nominal voltage that achieves the desired phase shift in stationary state. 2) Compute θ(z, t) for the rise transition towards the nominal voltage, by solving Equation (9) Find the phase-time curve of such transition by solving the structure electromagnetically, for each timestamp, after finding εr from Equation (8). 4) Repeat steps 2 and 3 for the rise transition towards the maximum voltage. 5) Pick, from the rise transition towards the maximum voltage, the timestamp in which the instantaneous phase matches the converged phase of the nominal transition. Then, the driving signal consists of modifying the amplitude of the nominal biasing signal to the maximum voltage between t = 0 and the obtained timestamp. Regarding the under-driving signal design, the procedure is dual by using a drop transition towards a zero voltage. In order to validate such technique, different temporal driving signals have been computed so as to reduce the switching times for different state transitions, and experimental measures have been obtained using those excitations. This can be seen in Figure 73 and Figure 74.

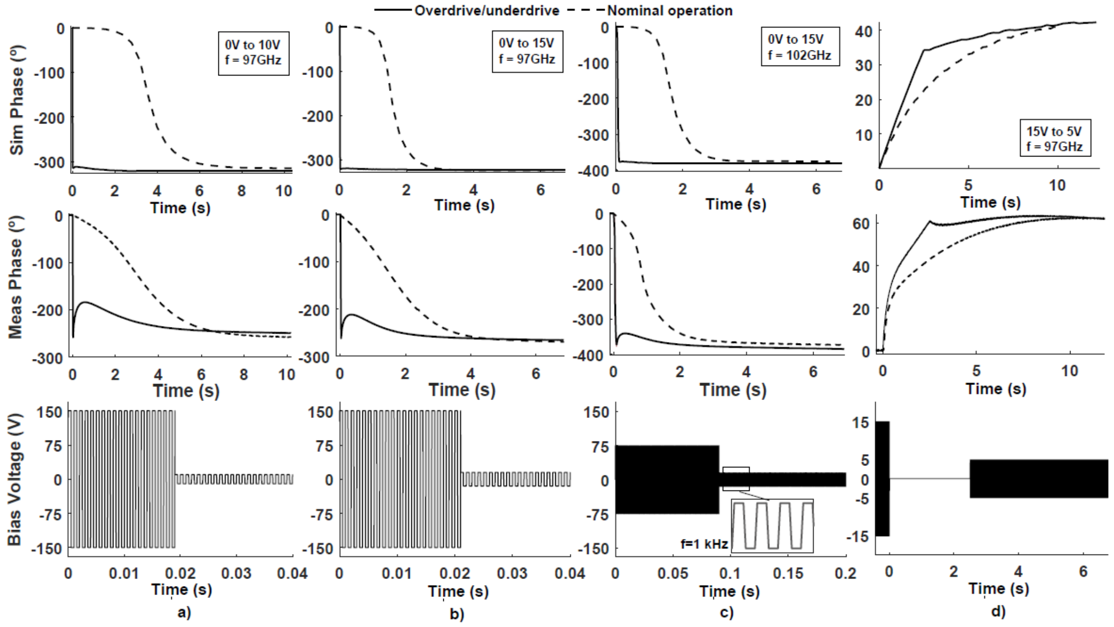

Figure 73: Phase transition between states using overdrive/underdrive and nominal excitations. Top row shows Simulations and middle row shows Measurements of a) 0V to 10V at 97 GHz, using a 150V overdrive for 19ms; b) 0V to 15V at 97 GHz, using a 150V overdrive for 21ms; c) 0V to 15V at 102 GHz, using a 75V overdrive for 90ms; d) 15V to 5V at 97 GHz, using 0V underdrive for 2.5s. Bottom row shows the applied overdrive/underdrive bias signal.

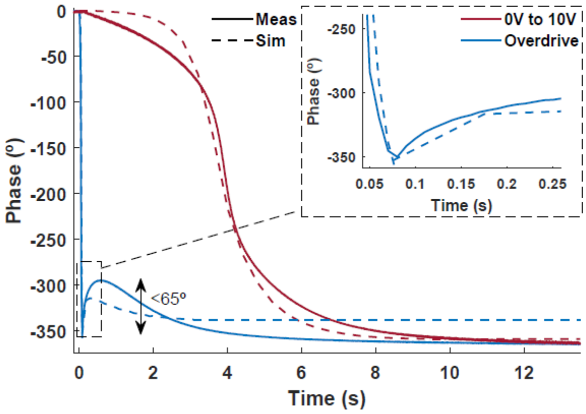

Figure 74: Measured and simulated phase of reflection coefficient at 102 GHz during a 0V to 10V transition.

Overall, the predicted and measured reflectarray cells transitioned a maximum of 250X and an average of 100X faster between phase shift states when using overdrive techniques, as compared to using nominal excitations. On the other hand, thunder-drive excitations shortened in average a 2X time factor to achieve 90% of the objective phase, as compared to the nominal excitations.

3.3.5 Conclusions

The proposed confocal antenna has been fabricated as a proof-of-concept in W-band. The optics of the antenna has been experimentally verified in anechoic chamber using a passive sub-reflector, emulating one state of the reconfigurable antenna, with promising results. Also the reconfigurable reflectarray antenna based in liquid crystal technology has been experimentally characterized, and the voltage dependence of the phase extracted in the quasi-optical bench system. The next step is the integration of the system together with the control circuits that have already been tested without and with loads.

The dynamic control of the phase in reflectarray antennas with dual-polarization using liquid crystal technology is a very challenging task. This concept has been also studied and a new element proposed. Despite the difference between each set of orthogonal dipoles in both dimension and number, the optimized element can produce the same response for each polarization. A trade-off between phase range and losses allows to have 300° of phase with average losses of 3 dB, at 100 GHz, which is a very promising value at such frequencies, for an element with electronic control and low cost. The results obtained are promising and opens the door to the implementation of a simple proof-of-concept.

Finally, in order to improve one of the main drawbacks of the proposed LC-RA technology, namely the large switching times between phase states, we proposed and validated a dynamical model of LC transitions for different excitations beyond the known approximations in order to achieve a temporal control of the unit cell phase, useful for both reflective and transmissive cells. Even though the effect of the different LC driving excitations on the phase change can be carried out through both measurements and simulations, a generalization in frequency, incident angle, cell designs and LC materials could be cumbersome to do by means of measures. Instead, a simulation tool like the one studied allows for a fast and precise estimation of control signals to introduce the temporal parameter in the design space of future antennas. In turn, this allowed us to use an overdriving technique capable of drastically reducing transition times by orders of magnitude in a simple way, as well as to experimentally prove it for the first time by using time controlled excitation signals in LC reflectarray cells.

4 Metasurfaces

4.1 Performance requirements and design principles

In this sub-section we describe the developed algorithm for the estimation of the necessary metasurface size that grants a desired level of electromagnetic field amplitude at the observation point behind a wall. Geometrical configuration is presented in **Figure 75**.

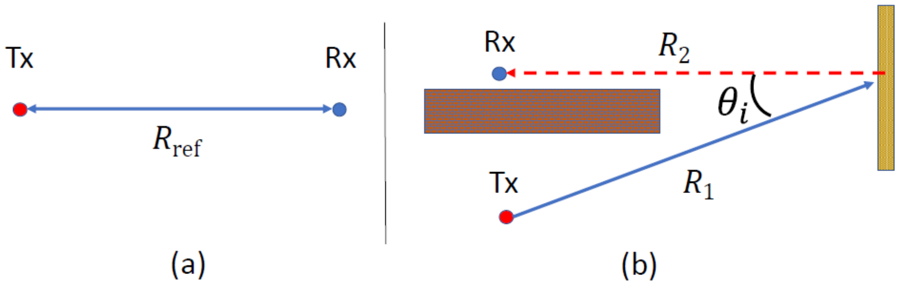

Figure 75: (a) - Reference free-space wave propagation; (b) - Metasurface scenario.

The approach is based on a comparison of the field anomalously reflected by the metasurface panel and the reference field created by the same transmitting antenna in free space, at a given distance R_{ref} from the antenna. In both calculations, we consider fields in the far zone of the antenna and the metasurface. The reference transmitting antenna can be arbitrary.

In **Figure 75**(a) we show an antenna located at point Tx and an observation point at Rx. In the far-field region, the field of any antenna is a spherical wave that decays inversely proportionally to the distance, and the field amplitude at the receiver position can be written as

$$|\boldsymbol{E}_{\mathbf{ref}}| = \boldsymbol{A}\,\frac{\mathbf{1}}{\boldsymbol{R}_{\mathbf{ref}}} \tag{10}$$

Here, A is the amplitude of the wave, which is not relevant for this study. Next, we describe the field, scattered from a metasurface, excited by the same antenna (rotated so that the metasurface is in the same direction as is the observation point in the reference problem), located at distance R_1 from the antenna. The observation point is located at distance R_2 from the metasurface, in accordance with the scheme, presented in **Figure 75**(b).

First, we consider the situation when the anomalously reflected metasurface has the size that is small when compared to the curvature radius of the illuminating spherical wave. In this case, we can approximate the incident field by a plane wave, whose amplitude (at the position of the metasurface) we denote as E_0.

The field, reflected by the metasurface located on the wall surface is

$$\boldsymbol{E}_{\mathrm{sc}\,z} = \frac{\boldsymbol{jk}}{\boldsymbol{4\pi}}\frac{\boldsymbol{e^{-jk|\mathrm{r}|}}}{|\mathbf{r}|}\boldsymbol{E}_0\left[\boldsymbol{a}_2^2\big((\mathbf{1}+\boldsymbol{R})\cos\boldsymbol{\theta} - (\mathbf{1}-\boldsymbol{R})\cos\boldsymbol{\theta}_i\big)\mathbf{sinc}(\boldsymbol{k}\boldsymbol{a}_{\mathrm{ef}}) \right. \\ \left. + \boldsymbol{a}_1^2\sum_{\boldsymbol{n}}(\boldsymbol{r}_{\boldsymbol{n}} - \boldsymbol{R}\boldsymbol{\delta}_{\boldsymbol{n}})(\cos\boldsymbol{\theta} + \cos\boldsymbol{\theta}_{\mathrm{r}\boldsymbol{n}})\mathbf{sinc}(\boldsymbol{k}\boldsymbol{a}_{\mathrm{ef}\,\boldsymbol{n}})\right]$$

(11)

Here, n is the number of the reflected Floquet harmonic, a_1^2 and a_2^2 define the metasurface and reflecting uniform surface areas, $\mathbf{r}$ is the position vector pointing to the observation point, $k = 2\,\pi/\lambda$ is the surrounding (free) space wavenumber, R is the reflection coefficient of the surrounding uniform surface wall, θ_i is the incidence angle, θ is the angle between the normal and the direction to the observation point, $a_{\mathrm{ef}} = (\sin\theta - \sin\theta_{\mathrm{i}})a$, $a_{\mathrm{ef}\,n} = (\sin\theta - \sin\theta_{\mathrm{r}\,n})a$, and δ_n is the delta function ($\delta_0 = 1$ and $\delta_{n\neq 0} = 0$). For the first reflected harmonic, if the metasurface operates perfectly, we have $r_1 = \sqrt{\frac{\cos\theta_{\mathrm{i}}}{\cos\theta_r}}$, and the other harmonics have zero amplitudes.

We are interested only in the second term inside the square brackets, defining the reflection from the metasurface, because reflections from the uniform wall go into the specular direction. For the observation point at $\theta_{\mathrm{r}} = 0°$, we have $a_{\mathrm{ef}\,n} = 0$, and the sinc function is unity. Delta function becomes zero for the first propagating reflected harmonic, and the result inside the brackets with cosine summation is simply 2 (the observation point is located exactly at the direction of propagation of the reflected wave, $\theta = \theta_{\mathrm{r}} = 0$). Using equation **(10)**, we can write for the excitation field at the metasurface plane $E_0 = \frac{A}{R_1}$, then we can simplify equation **(11)** as follows:

$$|E_{\mathrm{sc}z}| = \frac{E_0\, a_1^2\sqrt{\cos\theta_{\mathrm{i}}}}{\lambda\, R_2}$$

(12)

Finally, we require that the amplitude of the reflected field at the observation point is equal to that of the field at the reference distance R_{ref} in free space, namely, $|E_{\mathrm{sc}z}| = \frac{A}{R_{\mathrm{ref}}}$. Then the required size a_1 (area a_1^2) of the metasurface reflector can be expressed as

$$a_1 = \sqrt{\frac{R_1\, R_2\, \lambda}{R_{\mathrm{ref}}\sqrt{cos\ \theta_i}}}$$

(13)

As an example, we can set $R_1 = R_2 = \frac{R_{\mathrm{ref}}}{2} = 5$ m. For the frequency range of our interest (100 – 200 GHz), the required size of square metasurfaces is presented in **Figure 76**.

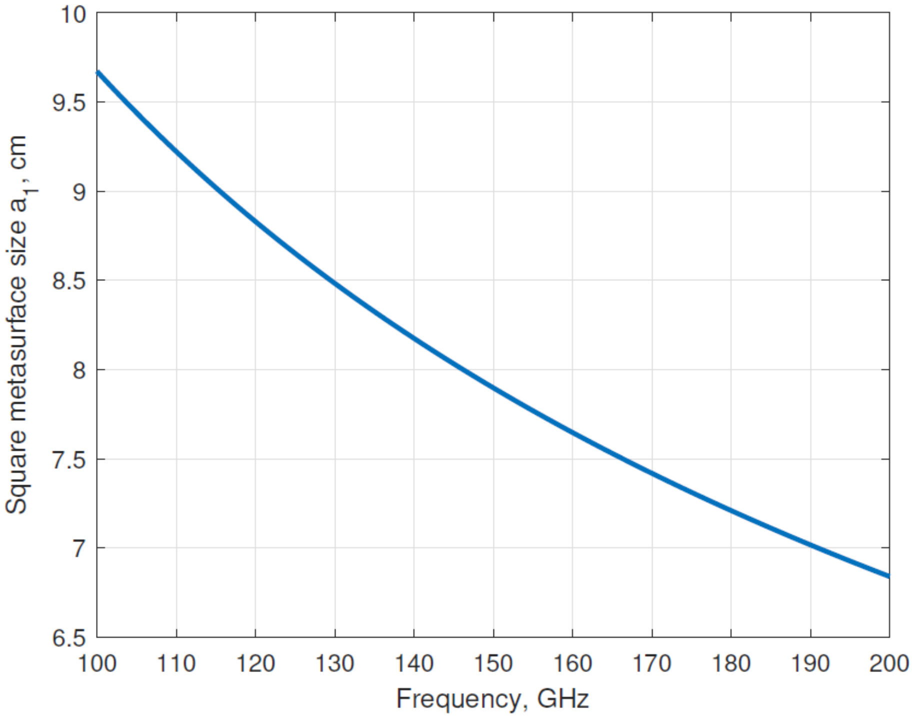

Figure 76: Required metasurface size calculated in accordance with Equation (13)

We have derived analytical expressions for a qualitative estimation of the link budget. The ratio between the transmitted and received powers can be found as

$$|S_{21}|^2 = \frac{P_r}{P_t} = G_t G_r \left(\frac{S_{\mathrm{MS}}}{4\pi R_1 R_2}\right)^2 |\cos\theta_i| \eta_{\mathrm{eff}}$$

(14)

The main parameters that define the metasurface-enabled channel are the gains G_t and G_r of the source and receiver antennas, positions of the source and receiver (R_1, R_2 and $\cos\theta_i$), the metasurface area (S_{MS}) and the power reflection efficiency (η_{eff}) of the metasurface. More details on workability and performance of the approximate model of equation **(14)** is presented in deliverable D5.1 of this project.

Description of the anomalous reflectors' implementation principles.

The Aalto group has introduced a general and efficient method for the independent control of port responses in multichannel multifunctional metasurfaces [23]. To implement the desired scattering matrix of the metasurface, the idea is to find a set of evanescent modes excited at each incidence scenario, which together with the defined propagating modes simultaneously satisfy the same impedance boundary condition at the metasurface. The method uses mathematical optimization tools to find the Fourier coefficients of the surface admittance expansion that realize the defined scattering matrix, taking into account the properties of the dielectric substrate.

The required period of the metasurface D can be expressed as $D = \frac{\lambda}{|\sin\theta_r - \sin\theta_i|}$, and simplified for our case of propagation directions between the normal incidence and the one under some particular angle of reflection to $D = \frac{\lambda}{\sin\theta_r}$. We have considered the angle of incidence to be 50 deg., in which case the required periods in the design are given by the following table:

Table 40: Periods of the metasurface for the desired central operational frequencies.

design number	frequency, GHz	period D, mm
1	144.75	2.705507
2	150.75	2.482549
3	170.9	2.291528

The prospective metasurfaces unit cells are characterized by discrete values of the sub-cells' impedances. The overall design procedure splits into the next general steps:

Taking into account computational resources (time consumption) and realistic limitations of available photolithography microfabrication processes (characteristic dimensions to be at least of the order of several micrometers), define the minimum number of sub-cells, where one can obtain a solution for the desired functionality. As a result, we obtain several values of the surface impedance (reactance) over the metasurface unit cell.

Using full-wave simulations check if the found solution satisfies the required functionality of an anomalous reflector with the obtained surface impedance sheet parameters model. In practice, this simulation should grant very close to 100% efficiency.

Using full-wave simulations define a realistic sub-cell topology and find geometrical parameters that provide the desired values of the surface impedances.

Using full-wave simulations check the performance of the designed structure. If needed, make numerical optimization of geometrical parameters, in order to obtain the best possible performance (depending on different factors this optimization can be not necessary, however, in some cases it is a very tough but important step to correct impedance mismatch and ensure high efficiency). At this step the design can be assumed as finalized, however, tolerance and other relevant analysis can be still required before manufacturing.

4.1.1 Design

Practical considerations and limitations.

In order to realize the desired functionality of anomalous reflection at a given frequency, the metasurface structure can be realized as a sub-millimeter metallic pattern at a thin low-loss dielectric substrate. Simple realizations of sub-cells with a given surface reactance can be found using capacitive gap and inductive strip topologies [24]. However, the presence of inductive strips usually leads to degradation of the metasurface performance due to ohmic losses and should be avoided if possible, or at least solutions should not contain any high values of positive reactance. At a first steps of our design work, we focused on thin Si substrates in order to achieve this goal, as a thin high-permittivity dielectric substrate provides more angularly stable solutions for the impedance of sub-units, comparing with quartz, for example. We assumed at that point that practical realization of the designs could be done with 4-inch wafers of Si material, compatible with Aalto University nanofabrication facility and in accordance with available consumables (Si wafers of 100um thickness) on the open market.

After a set of attempts we found that the optimum minimum number of sub-cells is 5. A theoretical solution for the incidence angle $\theta_r = 50^\circ$ based on mathematical optimization provided the following values for the surface reactance (Ohm) using Si wafer of 100 um thickness, permittivity $\varepsilon_r = 11.7$:

144.75 GHz: [-177, -101, -2000, -2000, -171]
157.75 GHz: [-102, -2000, -2000, -192, -230]
179.90 GHz: [-123, 50, -440, -400, -202]
Diffracted modes amplitudes for the found theoretical solutions of anomalous reflectors at 100um Si substrate, permittivity $\varepsilon_r = 11.7$ and the incidence angle $\theta_r = 50^\circ$ are presented in **Figure 77**.

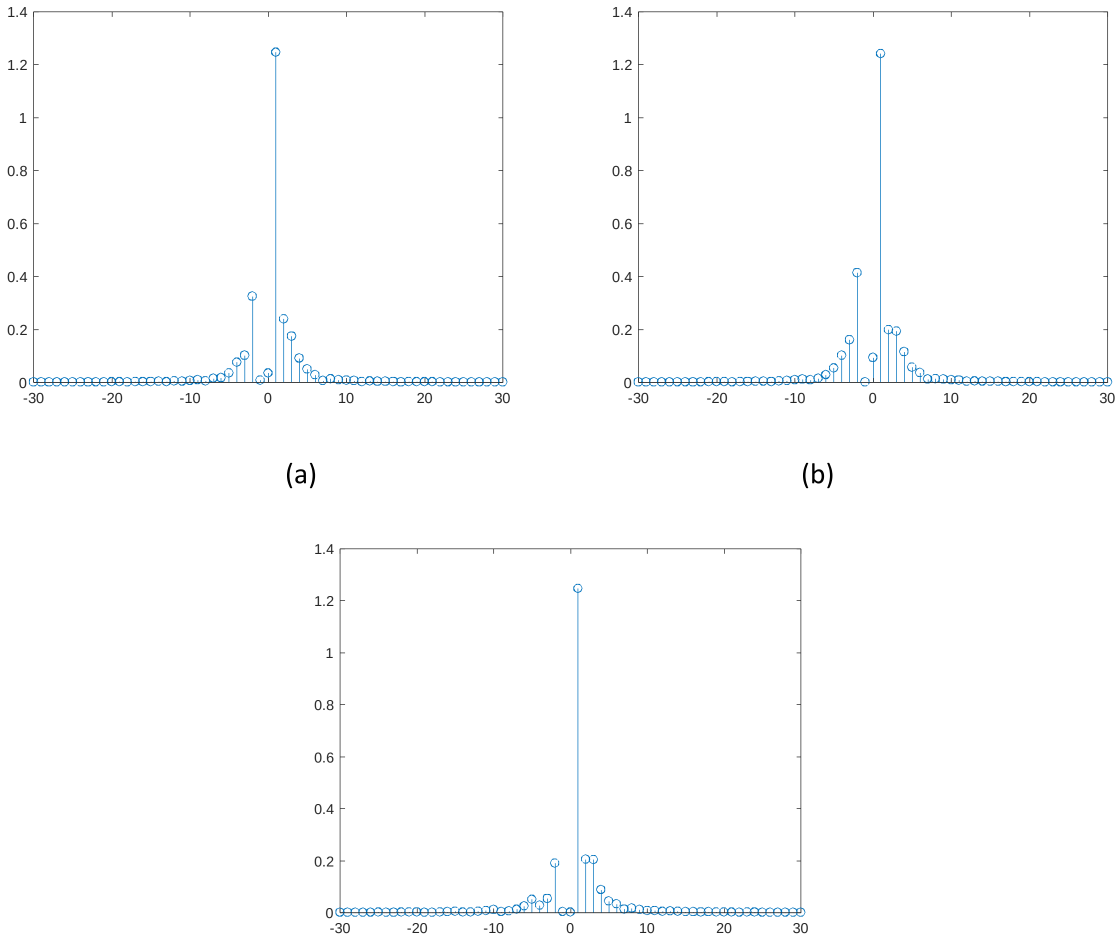

(a)

(b)

(c)

Figure 77: Diffracted modes amplitudes for the found theoretical solutions of anomalous reflectors at (a) – 144.75 GHz, (b) – 157.75 GHz, and (c) – 170.90 GHz with 100um Si substrate, permittivity $\varepsilon_r = 11.7$, and the incidence angle $\theta_r = 50^\circ$.

A possible implementation process for these solutions will be presented in the next subsections of this report. However, due to practical difficulties with realization of this type of structures – very thin layer of Si requires bonding above another thick supporting wafer, and also because the manufacturer provided unexpectedly ununiform wafers (the thickness variation was more 20 um), we adopted another, simpler way of realization of metasurfaces with the desired functionality based on thicker quartz wafers and another type of sub-cells. In particular, our analysis showed that it is possible to use the so-called dog-bone unit cells, and it can grant better angular stability. Thus, it may be possible to find solutions with thicker quartz substrate wafers. There are wafers with the average 209.5 um thickness available at our group now, thus we tried to find theoretical solutions with these parameters. Similarly, to the method explained above, we found 8 sub-cells unit as the optimum number for finding possible design impedance characteristics. The 209.5 um thickness quartz-based solution (Ohm) is as follows:

144.75 GHz: [-319, -1686, -346, -138, -991, -1721, 50, -1140]
157.75 GHz: [-993, -791, 40, -834, -591, -774, -1089, -138]
170.90 GHz: [-1034, -828, -145, 50, -317, 50, -1432, -990]

Diffracted modes amplitudes for the found theoretical solutions of anomalous reflectors at with 209.5 um quartz substrate, permittivity $\varepsilon_r = 4.2$, and the incidence angle $\theta_r = 50^\circ$ are presented in **Figure 78.**

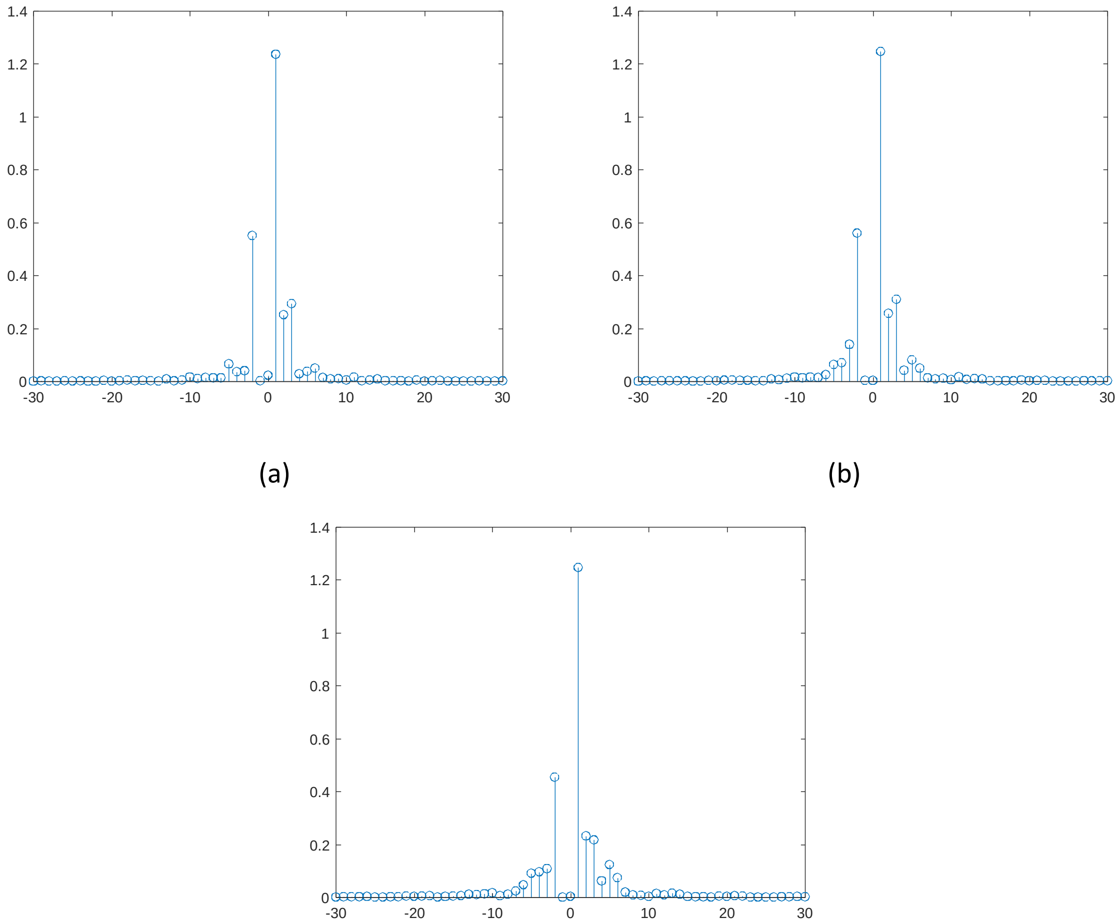

(a)

(b)

(c)

Figure 78: Diffracted modes amplitudes for the found theoretical solutions of anomalous reflectors at (a) – 144.75 GHz, (b) – 157.75 GHz, and (c) – 170.90 GHz with 100um Quartz substrate, permittivity $\boldsymbol{\varepsilon_r = 4.2}$, and the incidence angle $\boldsymbol{\theta_r = 50^\circ}$.

Below we present a description of the implementation design.

At this point we obtained a set of discrete surface impedance values for the metasurface of perfect functionality. Every theoretical solution is checked via full wave simulations using a periodical structure with a given set of surface impedances in each period. Next, in order to obtain the corresponding geometric parameters of sub-cells, we conduct an extraction procedure, matching particularly desired values of surface impedance to geometrical parameters of unit cells. In order to achieve negative values of surface reactance we used two different types of patterns: strips with capacitive gaps (for Si-based designs) and the so-called *dog-bone* structures (for the quartz-based designs). Positive values of surface reactance are obtained with inductive strip elements.

The sub-cell topology simulation model in Ansys HFSS of a capacitive gap for Si 100 um-based design at frequency 144.75 GHz is presented in **Figure 79**(a), and the extracted surface impedance as a function of the gap parameter is presented in **Figure 79**(b). Finally optimized implemented parameters of the sub-cells are presented in **Table 41**. This design requires only negative values, and this is the only topology used in the extraction procedure. Large values of impedance are substituted with empty areas, thus, these parameter values are inapplicable here (also relevant for designs 2 and 3)

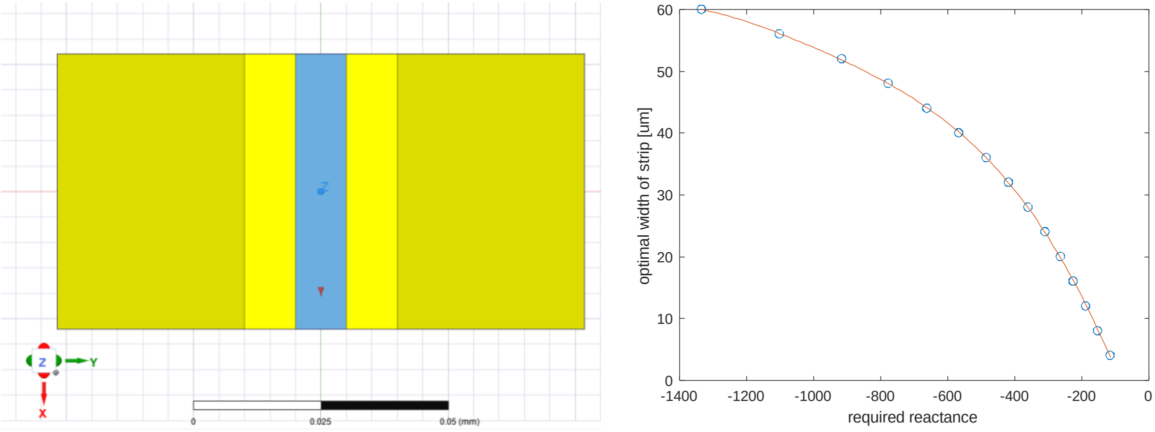

(a) (b)

Figure 79: Si 100 um-based design 1, frequency 144.75 GHz. (a) Sub-cell topology simulation model in Ansys HFSS of a capacitive gap design; (b) extracted surface impedance as a function of the gap parameter.

Table 41: Si 100 um-based design 1, frequency 144.75GHz implemented parameters of the sub-cells.

№	Im(Z), Ohm	g, um
1	-177	11.7
2	-101	3.6
3	-2000	-
4	-2000	-
5	-171	11.9

Extracted surface impedance as a function of the gap parameter for Si 100 um-based design 2 of the same topology as in **Figure 79**(a) at frequency 157.75 GHz is presented in **Figure 80**, and the finally optimized and implemented parameters of the sub-cells are presented in **Table 42**. This design requires only negative values, and this is the only topology used in the extraction procedure.

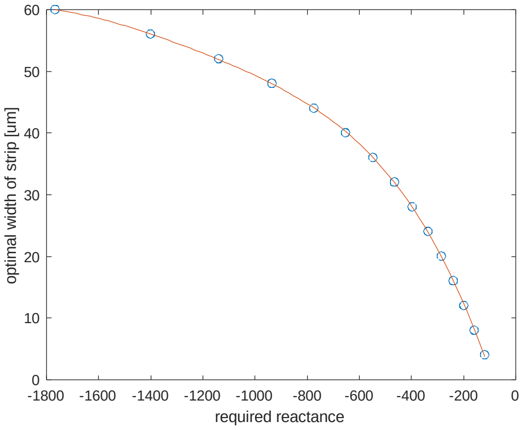

Figure 80: Si 100 um-based design 2, frequency 157.75 GHz. Extracted surface impedance as a function of the gap parameter. Unit cell topology of a capacitive gap is similar to the design 1 presented in Figure 79(a), thus it is not presented here.

Table 42: Si 100 um-based design 2, frequency 157.75 GHz. Implemented parameters of the sub-cells.

№	Im(Z), Ohm	*g*, um
1	-102	4
2	-2000	-
3	-2000	-
4	-192	15
5	-230	13.4

Extracted surface impedance as a function of the gap parameter for Si 100 um-based design 3 of the same topology as in **Figure 79** at frequency 170.90 GHz is presented in **Figure 81**(a). This design requires also positive values of surface impedance, therefore, the sub-cell topology simulation model in Ansys HFSS of an inductive strip design is presented in **Figure 81**(b), and the extracted surface impedance as a function of the strip width parameter is presented in **Figure 81**(c). The finally optimized and implemented parameters of the sub-cells are presented in **Table 43**.

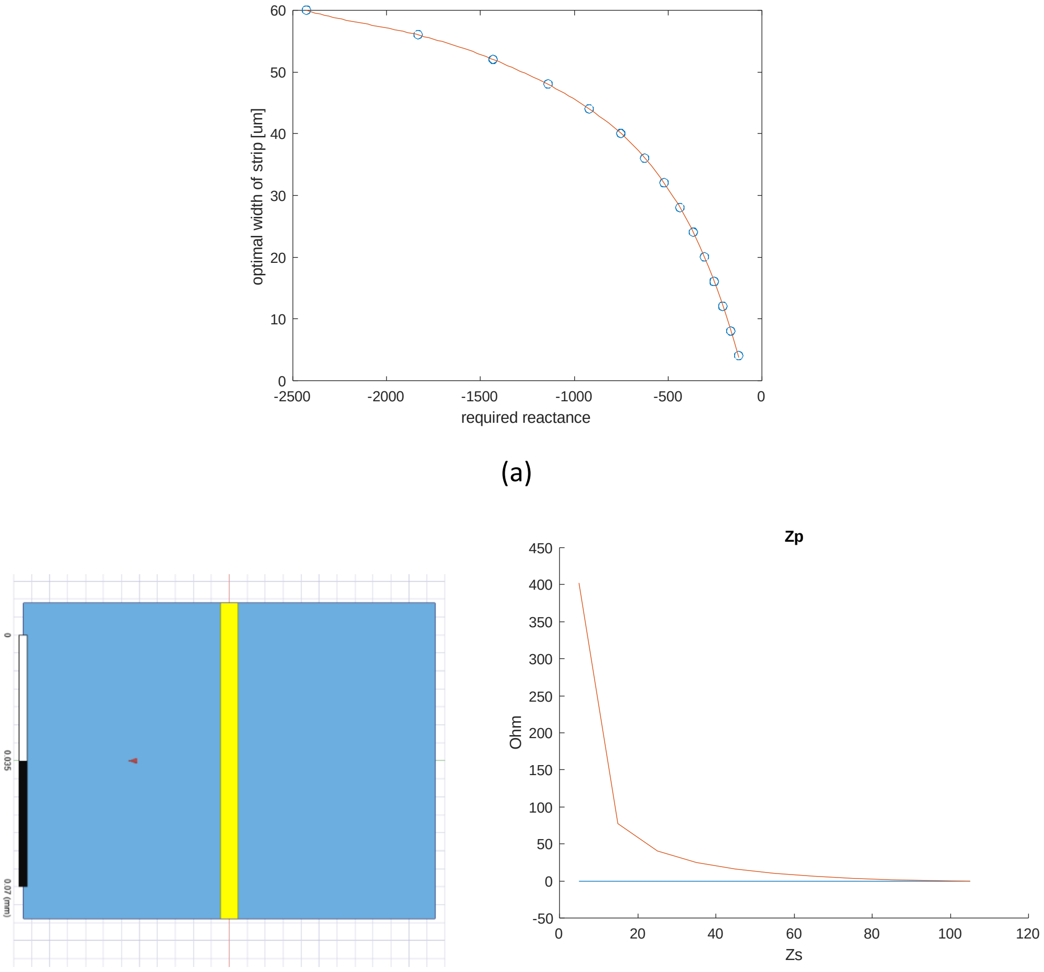

(a)

(b)

(c)

Figure 81: Si 100 um-based design 3, frequency 170.90 GHz. (a) Extracted surface impedance as a function of the gap parameter. The unit-cell topology of a capacitive gap is similar to design 1 presented in Figure 79(a), thus it is not presented here. (b) Sub-cell topology simulation model in Ansys HFSS of an inductive strip design. (c) Extracted surface impedance as a function of the strip width parameter.

Table 43: Si 100 um-based design 3, frequency 170.90 GHz. Implemented parameters of the sub-cells.

№	Im(Z), Ohm	*g*, um
1	-123	4.8
2	50	9
3	-440	35.2
4	-400	25.9
5	-202	11.7

The quartz-based design uses another topology of a sub-cell for negative impedance values. Here we have to consider a larger number of parameters for tuning. Sub-cell topology simulation model via Ansys HFSS of a capacitive dog bone design for the quartz 209.5 um-based design 1 at frequency 144.75 GHz is presented in **Figure 82**(a), and an example figure of extracted surface impedance as a function of dimensional parameters for incidence angles 0° and 50° is presented in **Figure 82**(b). We used particular cases for C_x, L_y, C_y, and L_x to achieve the desired values of the surface impedance, and the finally optimized parameters are presented in **Table 44**.

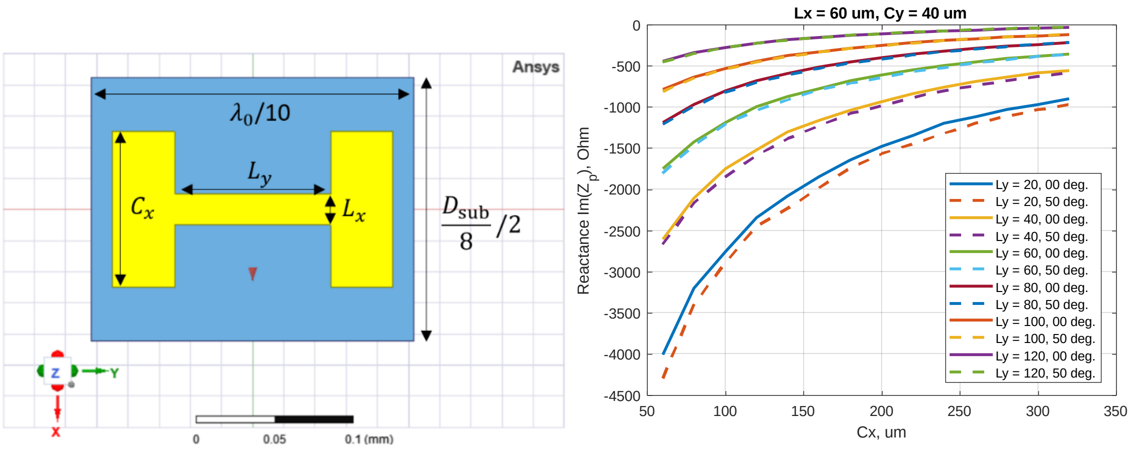

Figure 82: Quartz 209.5 um-based design 1, frequency 144.75 GHz. (a) Sub-cell topology simulation model via Ansys HFSS of a capacitive dog-bone design, (b) example figure of extracted surface impedance as a function of dimensional parameters for incidence angles 0° and 50°.

Table 44: Quartz 209.5 um-based design 1, frequency 144.75 GHz. Implemented parameters of the sub-cells.

el. N	Initial Z, Ohm	Cx	Ly	Cy	Lx
1	-319	156	100	40	60
2	-1686	64	60	Cy1	Lx1
3	-346	205	100	Cy1	Lx1
4	-138	286,5	100	Cy1	Lx1
5	-991	119,5	60	Cy1	Lx1
6	-1721	63,7	60	Cy1	Lx1
7	50	0	w	0	98
8	-1140	98	60	Cy1	Lx1

At the moment of this report compilation the Aalto group continues its work on implementation of the remaining 2 designs based on 209.5 um quartz substrates.

4.1.2 Simulations

Simulations of lossless and lossy metasurfaces performance.

In order to adequately describe performance degradation caused by ohmic losses in metal, below we present a table with calculations of typical values of sheet resistance for gold, aluminum, and copper sheets at different frequencies.

Table 45: Example of sheet resistance estimations for typical materials and thicknesses available in cleanroom facilities.

material	resistivity ρ, Ohm m	thickness t, nm	sheet resistance Rs=ρ/t, Ohm/sq
Gold Au	2,44E-08	50	0,4880
	2,44E-08	100	0,2440
	2,44E-08	150	0,1627
	2,44E-08	200	0,1220
Aluminum Al	2,82E-08	50	0,5642
	2,82E-08	100	0,2821
	2,82E-08	150	0,1881
	2,82E-08	200	0,1411
Copper Cu	1,68E-08	50	0,3360
	1,68E-08	100	0,1680
	1,68E-08	150	0,1120
	1,68E-08	200	0,0840

However, after consultation with the group members, nevertheless we found that copper is the most suitable candidate to be used in microfabrication. But we found that it can be oxidized, and this is harmful after some time, whereas gold has much less oxidation problems. Thus, at the moment of this report compilation we are focused on the fabrication process based on 200 nm gold layer. Therefore, we use 0.2 Ohm/sq as the nominal resistivity value for full-wave simulations of the implemented lossy designs.

Next, we provide full-wave simulations of the implemented designs as periodical unit-cell structures. General performance of the Si-based design for 144.75 GHz and other main parameters are presented in **Figure 83**. This structure has demonstrated efficiency of 93.2% if only losses in metal are considered and 91.59% efficiency when Si loss tangent 0.002 is considered.

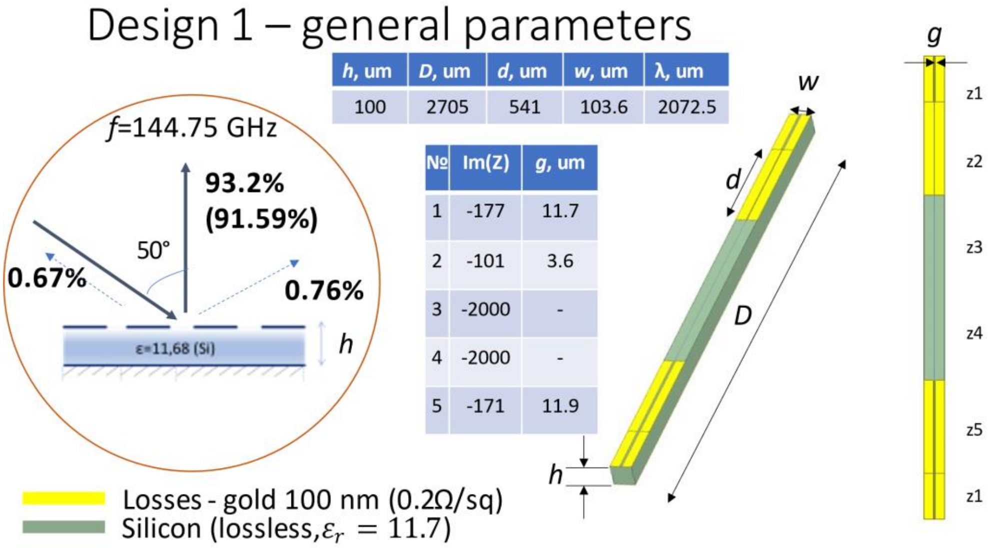

h, um	*D*, um	*d*, um	*w*, um	λ, um
100	2705	541	103.6	2072.5

№	Im(Z)	*g*, um
1	-177	11.7
2	-101	3.6
3	-2000	-
4	-2000	-
5	-171	11.9

Figure 83: Full-wave performance simulations for the implemented Si-based design for 144.75 GHz.

In the next set of simulations, we investigated tolerance of the structure for possible imperfections at manufacturing. Resulting efficiency curves for the case of lossy metal and lossless dielectric substrate as well as for varied parameter values are presented in **Figure 84**.

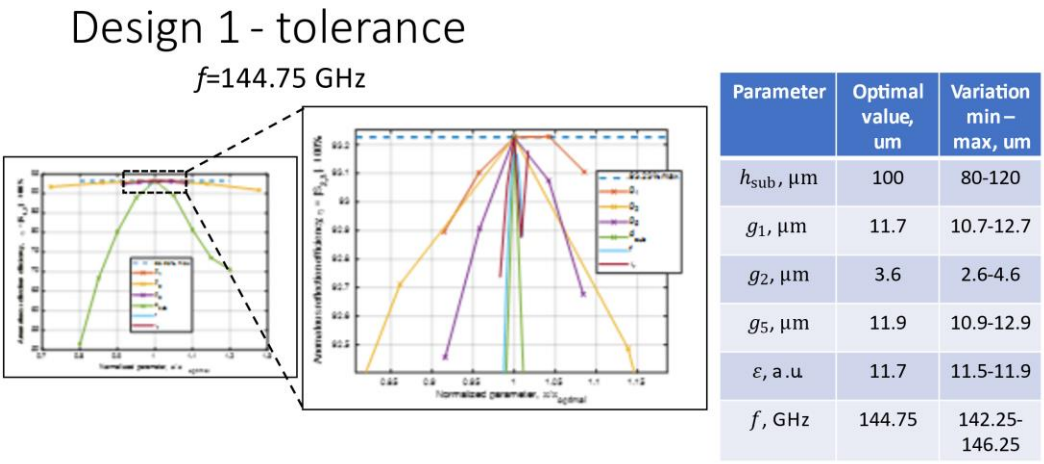

Parameter	Optimal value, um	Variation min – max, um
h_{sub}, μm	100	80-120
g_1, μm	11.7	10.7-12.7
g_2, μm	3.6	2.6-4.6
g_5, μm	11.9	10.9-12.9
ε, a.u	11.7	11.5-11.9
f, GHz	144.75	142.25-146.25

Figure 84: Tolerance simulations for the implemented Si-based design for 144.75 GHz.

General performance of the Si-based design for 157.75 GHz and other main parameters are presented in **Figure 85**. The structure demonstrated efficiency of 94.7% if only losses in metal are considered and 93.13% efficiency when Si loss tangent 0.002 is considered.

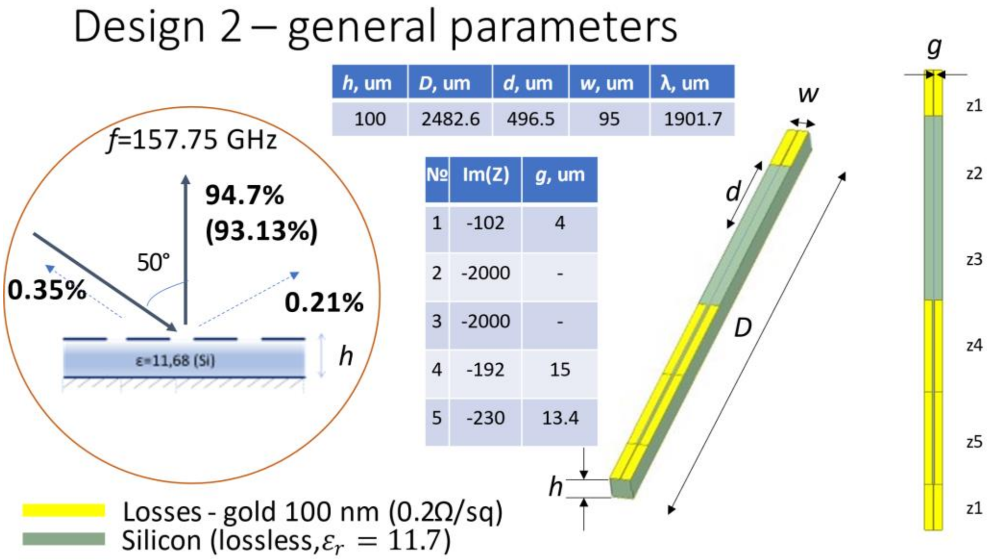

Design 2 – general parameters

h, um	*D*, um	*d*, um	*w*, um	λ, um
100	2482.6	496.5	95	1901.7

№	Im(Z)	*g*, um
1	-102	4
2	-2000	-
3	-2000	-
4	-192	15
5	-230	13.4

🟨 Losses - gold 100 nm (0.2Ω/sq)
🟩 Silicon (lossless,$\varepsilon_r = 11.7$)

Figure 85: Full-wave performance simulations for the implemented Si-based design for 144.75 GHz.

Resulting efficiency curves for the case of lossy metal and lossless dielectric substrate as well as for varied parameter values are presented in **Figure 86**.

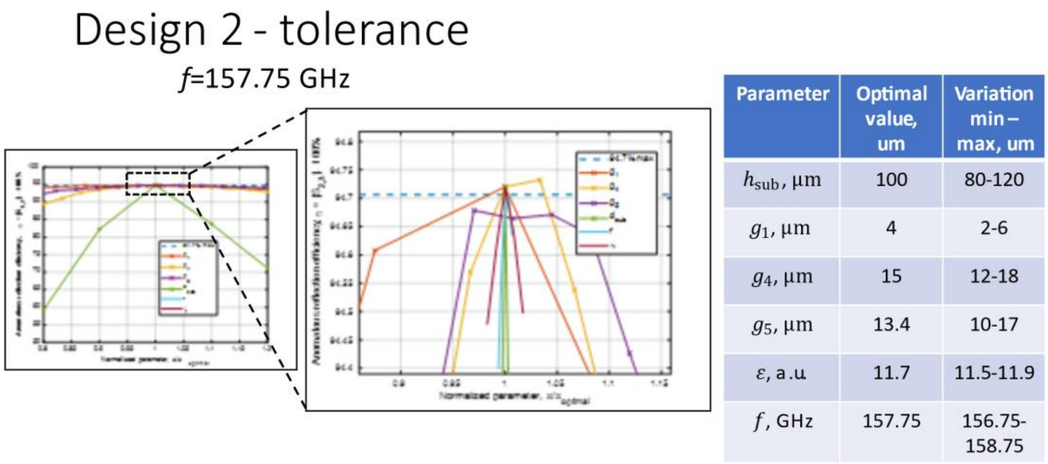

Design 2 - tolerance

Parameter	Optimal value, um	Variation min – max, um
h_{sub}, µm	100	80-120
g_1, µm	4	2-6
g_4, µm	15	12-18
g_5, µm	13.4	10-17
ε, a.u	11.7	11.5-11.9
f, GHz	157.75	156.75- 158.75

Figure 86: Full wave performance simulations for the implemented Si-based design for 144.75 GHz.

General performance of the Si-based design for 170.90 GHz and other main parameters are presented in **Figure 87**. The structure demonstrated efficiency of 93.79% if only losses in metal are considered and 92.57% efficiency when Si loss tangent 0.002 is considered.

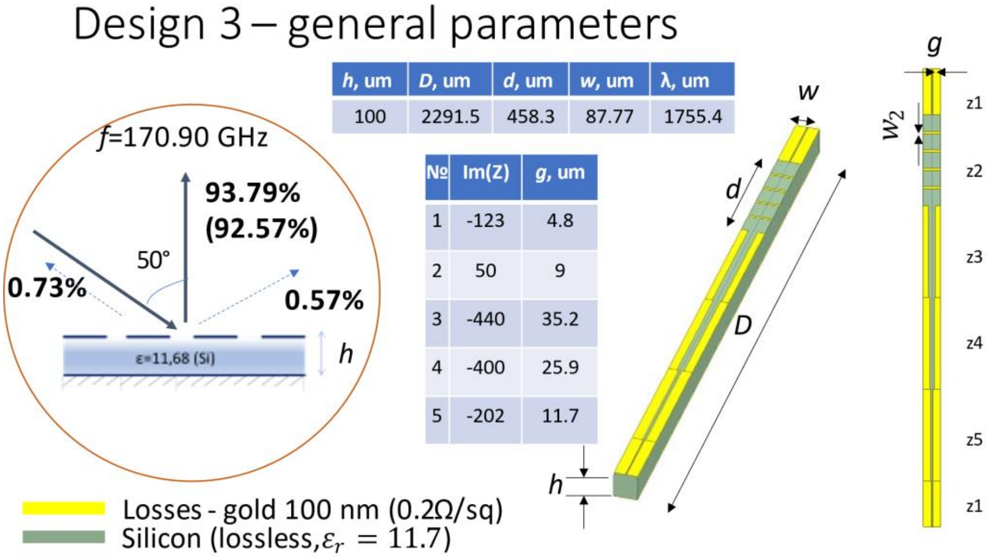

Design 3 – general parameters

h, um	*D*, um	*d*, um	*w*, um	λ, um
100	2291.5	458.3	87.77	1755.4

№	Im(Z)	*g*, um
1	-123	4.8
2	50	9
3	-440	35.2
4	-400	25.9
5	-202	11.7

🟨 Losses - gold 100 nm (0.2Ω/sq)
🟩 Silicon (lossless, $\varepsilon_r = 11.7$)

Figure 87: Full wave performance simulations for the implemented Si-based design for 144.75 GHz.

Resulting efficiency curves for the case of lossy metal and lossless dielectric substrate as well as for varied parameter values are presented in **Figure 88**.

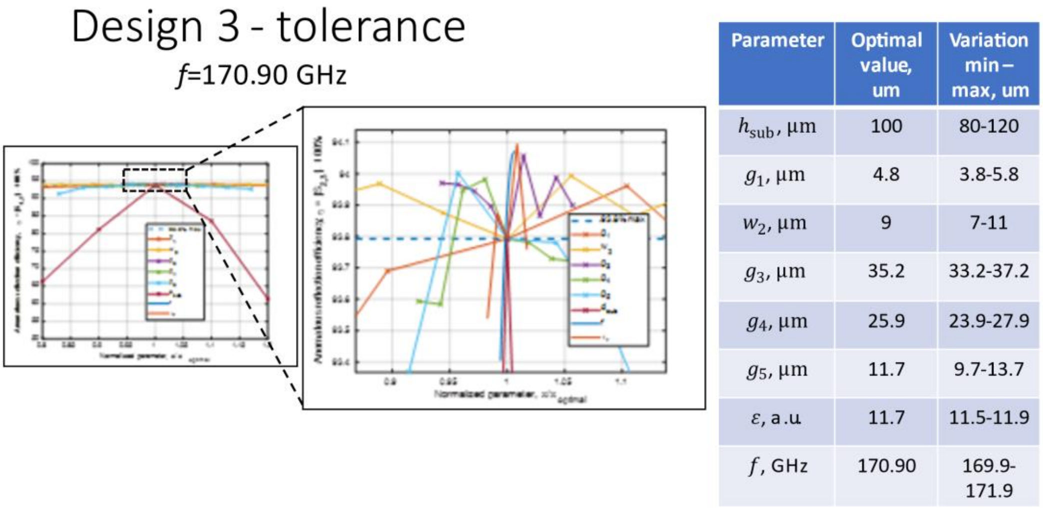

Design 3 - tolerance
f=170.90 GHz

Parameter	Optimal value, um	Variation min – max, um
h_{sub}, μm	100	80-120
g_1, μm	4.8	3.8-5.8
w_2, μm	9	7-11
g_3, μm	35.2	33.2-37.2
g_4, μm	25.9	23.9-27.9
g_5, μm	11.7	9.7-13.7
ε, a.u	11.7	11.5-11.9
f, GHz	170.90	169.9-171.9

Figure 88: Full-wave performance simulations for the implemented Si-based design for 144.75 GHz.

General performance of the quartz-based design for 144.75 GHz and other main parameters are presented in **Figure 89**. The structure demonstrated efficiency of 90.78% for both metal and dielectric losses consideration.

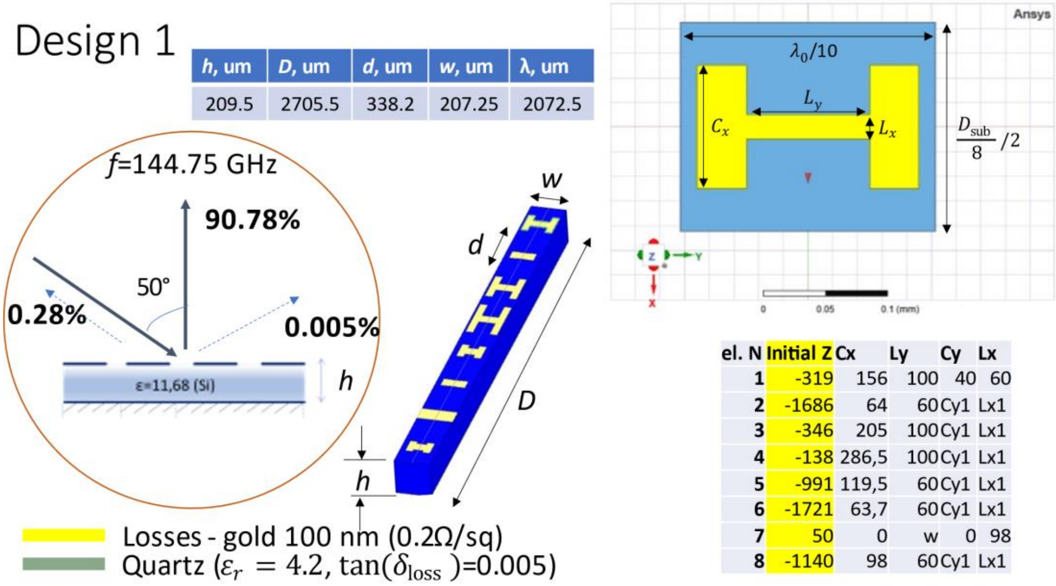

h, um	*D*, um	*d*, um	*w*, um	*λ*, um
209.5	2705.5	338.2	207.25	2072.5

el. N	Initial Z	Cx	Ly	Cy	Lx
1	-319	156	100	40	60
2	-1686	64	60	Cy1	Lx1
3	-346	205	100	Cy1	Lx1
4	-138	286,5	100	Cy1	Lx1
5	-991	119,5	60	Cy1	Lx1
6	-1721	63,7	60	Cy1	Lx1
7	50	0	w	0	98
8	-1140	98	60	Cy1	Lx1

Figure 89: Full-wave performance simulations for the implemented quartz-based design for 144.75 GHz.

Resulting efficiency tolerance curves as well as for varied parameter values are presented in **Figure 90**.

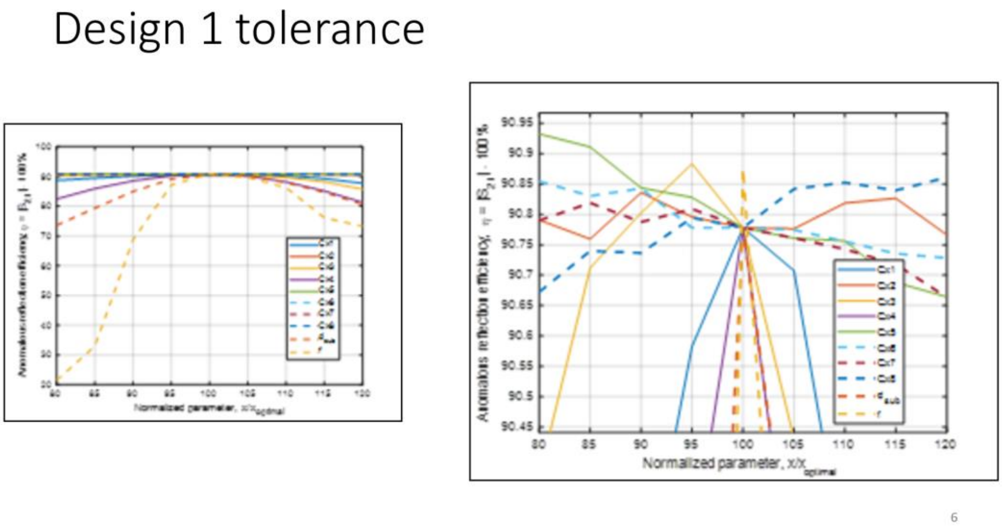

Figure 90: Full-wave performance simulations for the implemented quartz-based design for 144.75 GHz.

At the moment of this report compilation the Aalto group continues its work on implementation of the remaining two designs based on 209.5 um quartz substrates.

4.1.3 Prototyping

Fabrication technique description. Description of fabricated prototypes if ready.

For the realization of Si-based designs 100 um wafers were ordered from an external manufacturer. Due to strongly fragile nature of 100 um Si wafers, we had to consider a special manufacturing process. The general idea was to use supporting wafers in order to make the structure mechanically robust. For this purpose, photoresist can be used as a material for bonding two wafers. Two methods of manufacturing, based on AZ5214E photoresist and SU-8 photoresist were developed. Detailed fabrication plan for AZ5214E-based photoresist is presented in **Figure 91**.

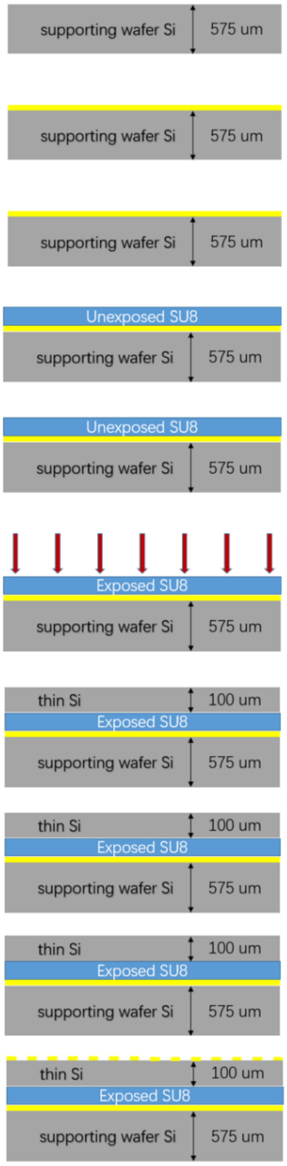

Step 1 – Prepare the thick supporting wafer

Step 2 - Deposit Au back plate, the thickness of metal is 50 nm (using MASA evaporation)

Step 3 – Measure the actual thickness of the structure from the highest point.

Step 4 – Spin coating SU8.

Step 5 – Soft bake at 95 °C for XX mins to remove solvent

Step 6 – UV-exposure for XX mins.

Step 7 – Transfer the thin Si wafer.

Step 8 – Hard (exposure) bake at XX °C for XX mins.

Step 9 – Measure the thickness of the sample to define the actual thickness of the top Si dielectric layer.

Step 10 – Using photolithography, deposit Au patch array (Mask aligner - Mauri Antero), the thickness of Au is 50 nm (using Evaporator MASA). We will order a mask. Resist is standard resist in cleanroom.

Figure 91: Si-based design. Fabrication method 1.

Fabrication plan using SU-8 photoresist is presented in Figure 92.

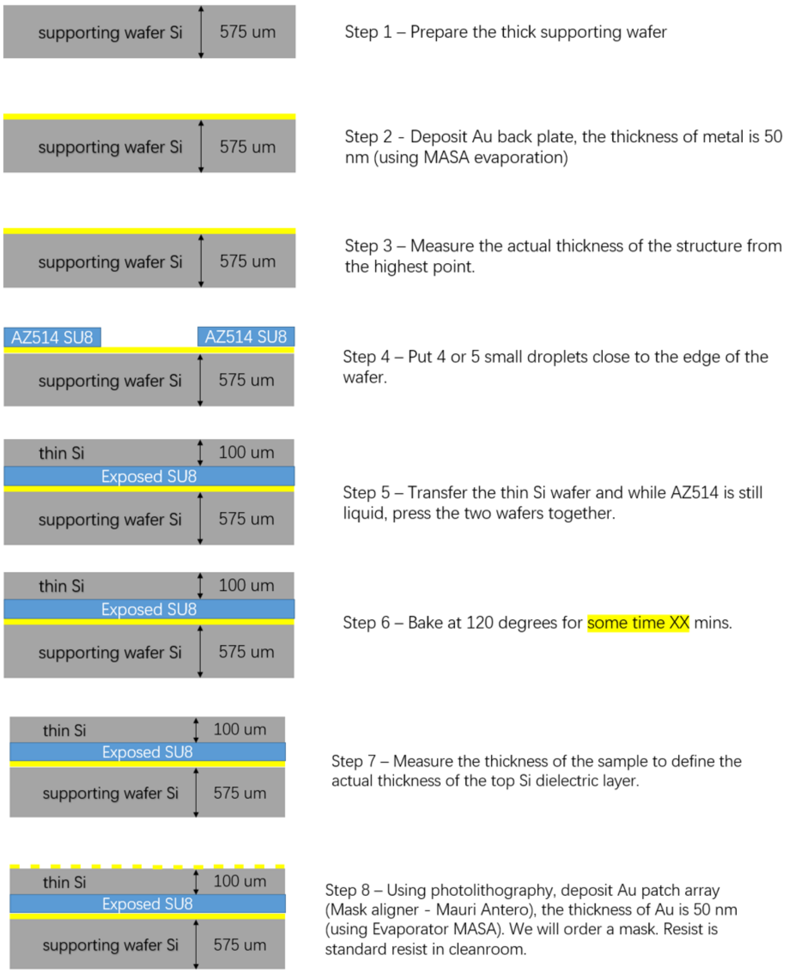

Step 1 – Prepare the thick supporting wafer

Step 2 - Deposit Au back plate, the thickness of metal is 50 nm (using MASA evaporation)

Step 3 – Measure the actual thickness of the structure from the highest point.

Step 4 – Put 4 or 5 small droplets close to the edge of the wafer.

Step 5 – Transfer the thin Si wafer and while AZ514 is still liquid, press the two wafers together.

Step 6 – Bake at 120 degrees for some time XX mins.

Step 7 – Measure the thickness of the sample to define the actual thickness of the top Si dielectric layer.

Step 8 – Using photolithography, deposit Au patch array (Mask aligner - Mauri Antero), the thickness of Au is 50 nm (using Evaporator MASA). We will order a mask. Resist is standard resist in cleanroom.

Figure 92: Si-based design. Fabrication method 2.

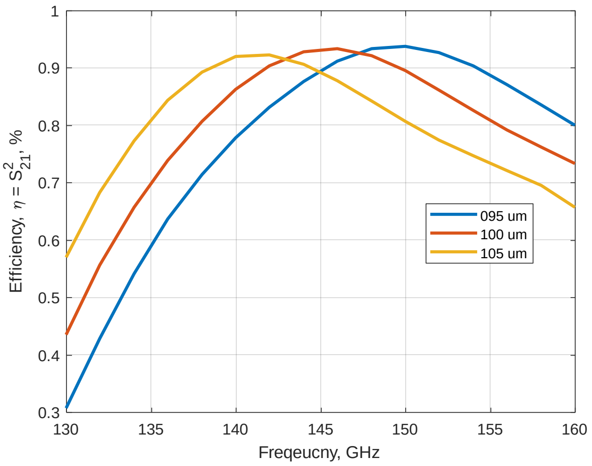

Figure 93: Si-based design for 144.75 GHz. Impact of substrate thickness variation in absolute values.

We have found that the total thickness variation of purchased wafers is more than 20%, and have made additional investigations for the impact of the thickness, on the resonance frequency due to possible mismatch of the structure parameters. Results of a broadband efficiency investigation of the metasurface performance for frequency 144.75 GHz are presented in Figure 93 for three different thicknesses. We found that for the used parameters our structure exhibits about 1 GHz shift of the resonance frequency for every 1 um change of the overall dielectric-layer thickness. Also, variation of the thickness over the wafer surface will cause additional degradation of performance. Thus, due to the poor quality of the purchased Si wafers and complicated manufacturing process we have decided to work on simpler, quartz wafer-based designs presented above in detail. Major benefits of quartz wafers are much stable total thickness variation (units of microns instead of dozens as in the case of Si) and much stronger body of the wafer itself – there is no need to bond it on a supporting wafer. Thus, we expect much simpler manufacturing processing.

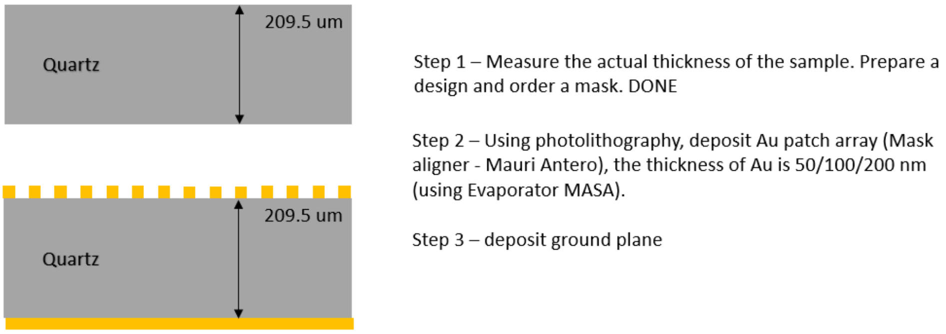

Step 1 – Measure the actual thickness of the sample. Prepare a design and order a mask. DONE

Step 2 – Using photolithography, deposit Au patch array (Mask aligner - Mauri Antero), the thickness of Au is 50/100/200 nm (using Evaporator MASA).

Step 3 – deposit ground plane

Figure 94: Quartz-based design. Fabrication method.

At the moment of this report compilation the Aalto group works on first prototype manufacturing based on the quartz design for 144.75 GHz. We have received a photolithography mask from the external manufacturer and are clarifying final processing steps with the cleanroom personnel.

After manufacturing we are going to measure the anomalous reflection characteristics in our mm-wave laboratory facility. Experiments will be based on the method described in Ref. [25]. Further, the same steps of manufacturing and validating will be made also for quartz-based designs for 157.75 GHz and 170.90 GHz.

4.1.4 Conclusions

- In summary, at this stage of the project work we have reached the following goals: We have developed a design and implementation procedure for anomalous reflectors suitable for the planned indoor demonstration
- For the target frequency bands, we have designed anomalous reflectors whose theoretically and numerically estimated performance goes well beyond the fundamental bound for conventional phase-gradient metasurfaces.
- We have considered different designs and discussed their benefits in view of various manufacturing difficulties. We have defined the optimum way for manufacturing. More results will be provided at later stages.

4.2 Propagation analysis of extremely large antenna arrays

Traditionally, phased arrays rely on linear phase shift beam steering (LPBS) [9] [26] [27]. This gives a straightforward way to maximize the antenna gain in the far-field (FF) of the array. In the near field (NF), the maximum gain is obtained with near field focusing (NFF) [28]. In this beam steering method, the antenna phases are calculated from the distances of the individual elements to the target location in order to achieve constructive summation of the electric fields and the maximum gain. However, this requires not only the beam steering direction, but also the distances from each antenna element to desired location and the exact path lengths.

In order to establish communications link, the channel is estimated first to calculate the optimal beamformers. However, there can be inaccuracy in the estimated beamformers, e.g., due to user movement. This requires constant updating of the channel estimates to adjust the beam steering directions. In this section, NFF and LPBS are analyzed in the NF of the antenna array. The main focus here is to analyze the impact of the user position uncertainty on the beamforming gain of extremely large antenna arrays in the NF at 140 GHz frequency, that is, in the middle of the D band. Above 100 GHz frequencies very high antenna gains lead to very large antenna arrays and higher probability of user being in the near field of the transmitter. By utilizing NFF, significant gain can be achieved over LPBS, but the NFF is also far more sensitive to the inaccuracy of the exact user position, as it will be shown later in the numerical results and illustrated in Figure 95.

There are several papers on the NFF for various applications. For instance, to give few examples, authors in [29] provided an idea for the wireless power transfer in the radiative NF. High resolution imaging using NFF was shown in [30]. Radio frequency identification with NFF has been considered, e.g., in [26]. NFF behavior of intelligent reflecting surfaces (IRS) was studied in [31]. Non-contact sensing was presented in [32]. Also, authors in [33] present focused beam array implementation for a planar array with two focal distances at 10 GHz center frequency. A detailed analysis of channel measurement as well as analysis for number of user positions was done in [34]. Therefore, the NFF has been shown to be very promising for NF applications. In this study, we append to the existing works by analyzing the NFF with imperfect user position to analyze the communications performance in NF.

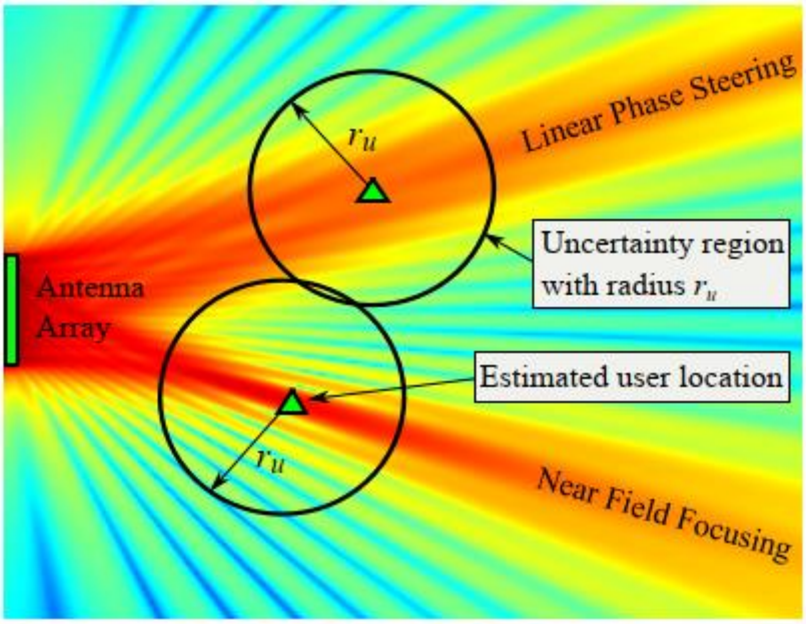

Figure 95: The system model considered here with the user locations, uncertainty regions, and antenna patterns by linear phase beam steering and near field focusing.

4.2.1 System model

The general system model considered herein is given in Figure 95. Furthermore, the detailed system geometry with LPBS and NFF is given in Figure 96. An electrically large antenna array is composed of large numbers of small antenna elements. The array can be considered as a single antenna structure when studying the signal propagation. Antenna array designing plays a vital role in the system performance, as the resulting signal strength depends on superimposed waves propagated from individual antenna elements. In LPBS, the beam is steered at a desired steering angle by calculating linear phase shift between the antenna elements, whereas in NFF, the idea is to control the phase of antenna array in such a way that the electric field sum constructively at the focus point. Plane wave and spherical wave concept arises from the distance between antenna array and user location. When the size of antenna array is very large in comparison with the wavelength, it is likely for a user to be in the NF of the array. Two approaches, namely NFF and LPBS are analyzed by generalizing propagation to two-dimensional (2D) geometry. Thus, we assume linear array in this study instead of planar array. It allows to study physically very large antennas. In the future work, we will extend the analysis to three-dimensional (3D) space, although, the fundamental operation principle is the same as in 2D space. However, the path loss model is assumed to be 3D by applying spherical expansion of the waves in the space, but the antennas and user drop spaces are 2D in this work.

The NFF gives the maximum gain in the NF due to perfect alignment of the incoming signal phases(in ideal setting). This requires knowledge of the user position, i.e., one extra degree of freedom compared to the LPBS which only requires the directions (azimuth and elevation). Both methods give the same gain in the far field due to planar wave propagation. However, and as it can be intuitively deduced based on Figure 95 and Figure 96, the NFF is far more sensitive to the exact user position, where imperfect position information impairs the achievable gain. This will be shown in the numerical results with implications it gives. In Figure 95 two circle represents uncertainty region with radius r_u.

4.2.1.1 Propagation modeling

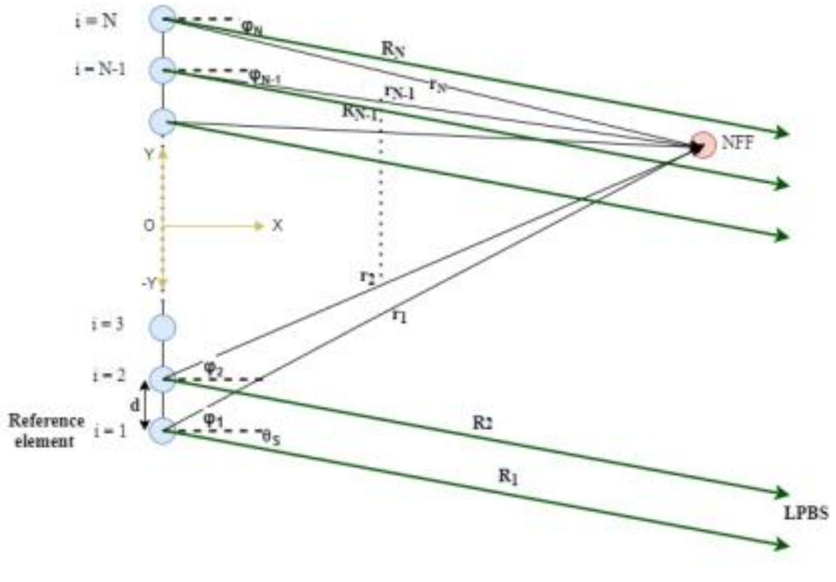

Figure 96: System geometry for NFF and LPBS with N element linear antenna array.

The wave is propagating in 2D plane based on the steering angle or focus point as shown in **Figure 96**. The NF and FF regions of antenna array can be given as [9] [35]

$$F_n < \frac{2D^2}{\lambda} \leq F_f,$$

(15)

where F_n and F_f are the NF and FF, respectively, *D* is the maximum dimension of antenna, and λ is the wavelength of the electromagnetic (EM) wave. In the close proximity of the antenna, the electric field changes rapidly with spatial position due to spherical signal propagation.

A linear array with *N* identical antenna element is placed on y-axis and centered at the origin of coordinate system as shown in Figure 96. The size of linear array antenna is *D* = (*N* – 1)*d*, where *d* is the antenna element spacing. The phases of the antenna elements are given in the next two section for the LPBS and NFF.

1. *Linear Phase Beam Steering:* The LPBS is a conventional beam steering approach which is based on steering angle (θ_s) obtained by element-wise linear phase shifts [27]. This phase shift (Δ) between two successive elements is calculated as

$$\Delta = \frac{2\pi}{\lambda} d \sin(\theta_s)\,.$$

(16)

2. *Near Field Focusing:* The NFF produces a focused beam at focus point. The exact phase of an antenna element depends on its distance to the focus point and the EM wavelength, as the NFF requires aligning the phases at the focus point. The overall electric field at any given point in space is a summation of signal contributions from individual antenna elements. Thus, the phase required to focus spherical wave at defined focus point can be computed as [26], [33]

$$\phi_i = \frac{2\pi}{\lambda} r_i,$$

(17)

where r_u is the distance between the focus point and the antenna element, and it can be expressed as

$$r_i = \sqrt{(x - x_i)^2 + (y - y_i)^2}$$

(18)

where *x* and *y* represent the position of focus point, and x_i and y_i gives the position of the *i*th antenna element.

3. *Array Factor:* The array factor A_f gives the radiation pattern of the antenna at some observation point. It is based on geometry and the excitation phase of antenna array [9] [28] [35]. For a uniform linear array with *N* elements, A_f can be expressed as

$$A_f = \frac{1}{\sqrt{N}} \sum_{i=1}^{N} a_i e^{-j\psi_i}\,,$$

(19)

where a_i is the weight factor, ψ_i= (i – 1)Δ for LPBS, and ψ_i= $2\pi d_i/\lambda - \phi_i$ for NFF, where d_i is the vector length from the *i*th antenna element to the spatial coordinates of the observation point.

4.2.1.2 Signal Model

We consider free space path loss (FSPL) channel model in line-of-sight path between the antenna array and user location. Path loss is given by $(4\pi r)^2/\lambda^2$ [36], where r is a distance between the transmitter and the receiver. Utilizing the above array factor, the total received power P_{Rx} in general case can be calculated as

$$P_{Rx} = \frac{P_{Tx}G_{Rx}}{N}\left|\sum_{i=1}^{N}\frac{a_i}{\sqrt{P_L(d_i)}}e^{j\left(\frac{2\pi d_i}{\lambda}-\Psi_i\right)}\right|^2 , \tag{20}$$

where exp($j2\pi d_i/\lambda$) accounts for the linear phase shift due to propagation, Ψ_i are the antenna phases and are taken as (i–1)Δ for the LPBS and ϕ_i for the NFF, and G_{Rx} is the receiving antenna gain. This expression is generally valid for NF and FF, but per-antenna path losses and linear phase shifts are required in the NF due to spherical signal propagation close to the antenna array. Then the above becomes

$$P_{Rx} = \frac{P_{Tx}G_{Rx}}{P_L(r)}\left|A_f(\overline{r})\right|^2, \tag{21}$$

where r is the distance to the observation point and $\overline{r}$ is the observation point about which the array factor has been calculated given perfect alignment of the Rx antennas.

4.2.1.3 SNR

In order to calculate the signal-to-noise ratio (SNR), we need to calculate the noise power. Based on the receiver noise figure (RNF) information, the noise floor N_{floor} is calculated as $N_{floor}(dB) = 10\log_{10}(k_B TB) + R_{NF}$, where k_B is the Boltzmann constant, T is the temperature, and B is the signal bandwidth. The SNR is then calculated as $SNR = P_{Rx}/N_{floor}$.

Based on above, the received power with LPBS and NFF approach are shown in Figure 97 and Figure 98, respectively, for 2048 element antenna array with element spacing $d = \lambda/2$. The NFF is formed directly in front of the antenna 25 meters away from the array. These figures show a significant difference between two approaches in terms of power distribution. A clear maximum is formed at the focus point with NFF whereas LPBS forms more uniform radiation pattern. It can be concluded that the transmitted power can be concentrated to a limited region utilizing NFF approach. For more details on the power profiles, authors in [26] provide design curves and performance data for NFF planar array, and for comparison unfocused array is taken into consideration. In [30], performance comparison of focused and unfocused antenna array is presented as well.

Figure 99 shows the received power as a function of distance for NFF and LPBS. In the NF region, the received power by NFF approach is superior to that of the LPBS, but both methods converge to the same gain in the FF. In the NF, at user positions, 10 m, 30 m and 50 m, NFF has 24 dB, 18 dB, and 15 dB more received power, respectively, when compared to LPBS. This is very promising gain in the ideal case. Next, we consider breaking the ideal response with uncertainty in the user position.

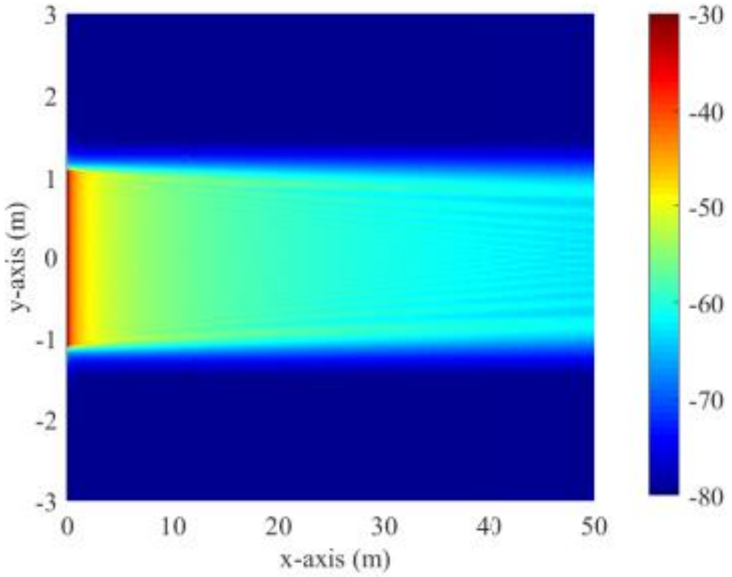

Figure 97: Received power (dBm) radiated by a Linear Phase Beam Steering (LPBS) array (θ_s=0).

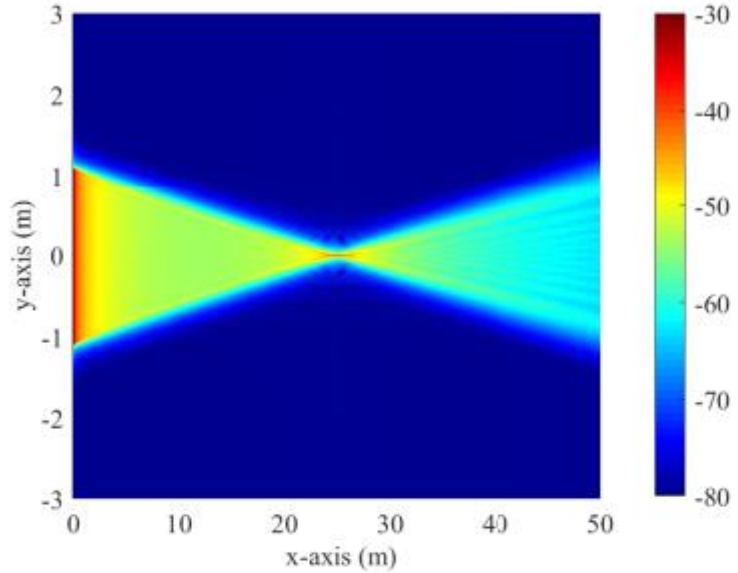

Figure 98: Received power (dBm) radiated by a Near Field focused (NFF) linear array (focus: x = 25 m, y = 0 m)

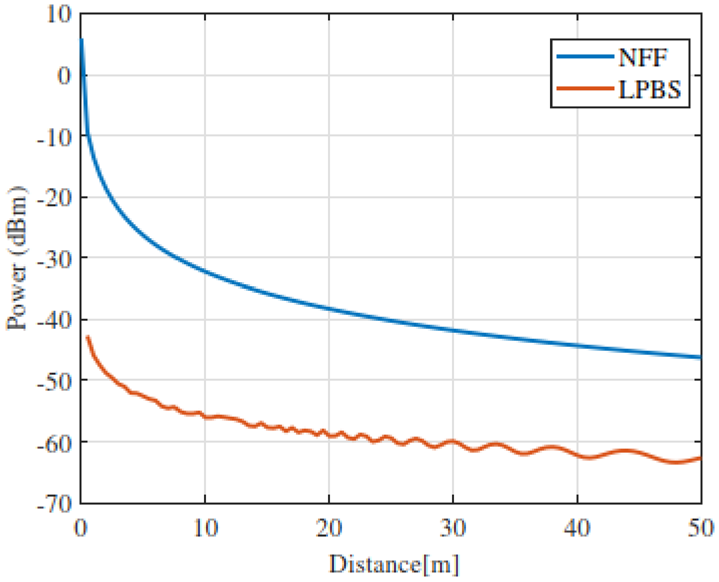

Figure 99: Received power comparison between NFF and LPBS as a function of the user location on x-axis. Focus equals the user location, θ_s = 0, and y = 0 m.

4.2.1.4 User Position Model

When designing a high frequency wireless system, it is crucial to think on localization and user tracking. In this work, we analyze the impact of the imperfect user position information on the achievable gain for NFF and LPBS. We analyze the user position uncertainty by assuming uniform distribution for user position inside a disk of radius r_u as shown in Figure 95. This can be done by using disk point picking principle [37]. In the simulation model, for a certain user location, M number of points are defined inside a disk over which the average received power can be calculated. Based on angle and random distance from center of the disk, x and y components for the M points inside the disk can be calculated as

$$X_k = \sqrt{r_k}\cos(\theta_k)\,, \tag{22}$$

where θ_k and r_k are drawn from uniform distributions, radius r_k from zero to r_u^2 and the angle is from zero to 2π. In this work we assume uniform distribution for the radius, but in the future work we will also consider other statistics for the user position error, such as Gaussian distribution. The position (r_{ik}) from each antenna array element *i* to the *k*th possible user position inside the disk can be calculated as

$$r_{ik} = \sqrt{(X_k - x_i)^2 + (Y_k - y_i)^2}, \tag{23}$$

where x_i and y_i give the *i*th antenna element position and X_k and Y_k represent *k*th possible user position inside disk. These give the tools to analyze the impact of the uncertainty on the receiver power levels.

4.2.2 Numerical Results

The parameters used in the numerical results have been listed in Table 46. In all results, the antenna array is fixed on the y-axis. In the results herein, we focus on SNR vs. user distance, SNR vs. uncertainty, and power distribution with different user position uncertainty for conventional beam steering and NFF techniques.

4.2.2.1 SNR vs. Link Distance

First, we investigate the SNR performance comparison of the NFF and LPBS as a function of user position along parallel (y-axis) and perpendicular (x-axis) paths with respect to the array position are shown in Figure 100 and Figure 101. In these figures, blue line represents NFF while red line represents LPBS. SNR performance as a function of uncertainty is shown. Three different uncertainties are considered: 0, 10 cm, and 50 cm. As uncertainty increases the received power decreases.

As expected, SNR performance with zero uncertainty is better as compared to increased uncertainty in any case. Figure 101 shows achieved SNR are substantially degraded with increased uncertainty when NFF is used. With NFF, at 25 meters away from the antenna, for 0 cm, 10 cm and 50 cm uncertainty regions produce SNRs of around 39, 25, and 22 dB respectively. For LPBS, the received powers at 25 m distance are around 19 dB for all these uncertainty regions. Hence, similar SNR performance is seen among these three uncertainty cases, while NFF is very sensitive to uncertainty in the user position. Note that this is partially attributed to the short wavelength at 140 GHz center frequency. This concludes that NFF allow improvement in achievable performance with low user uncertainty, but as uncertainty increases, LPBS performs very well when compared to NFF.

Table 46: Parameters used in the numerical results

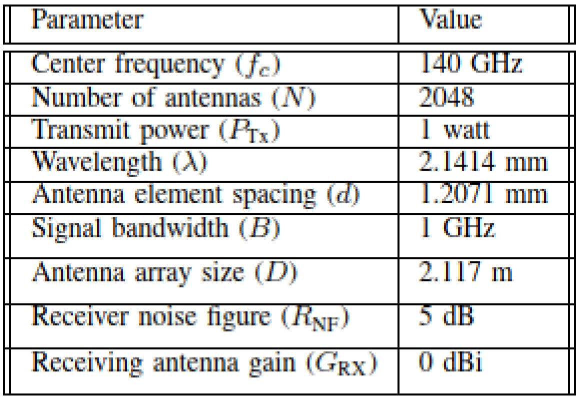

Parameter	Value
Center frequency (f_c)	140 GHz
Number of antennas (N)	2048
Transmit power (P_{Tx})	1 watt
Wavelength (λ)	2.1414 mm
Antenna element spacing (d)	1.2071 mm
Signal bandwidth (B)	1 GHz
Antenna array size (D)	2.117 m
Receiver noise figure (R_{NF})	5 dB
Receiving antenna gain (G_{RX})	0 dBi

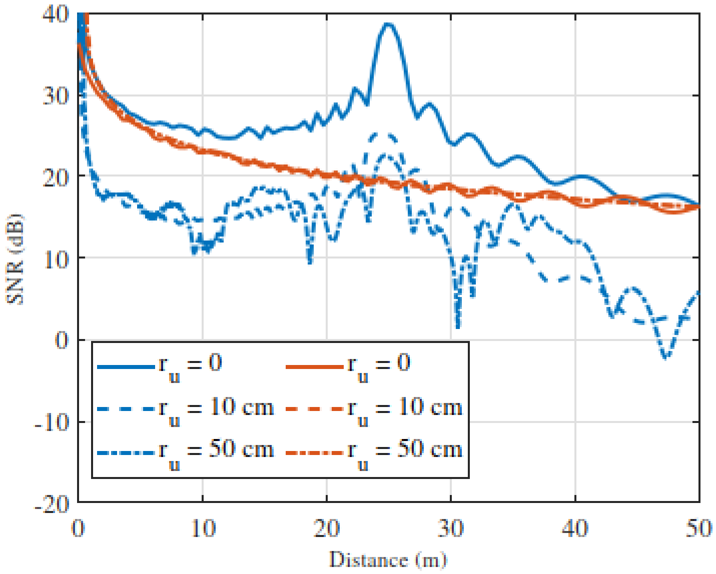

Figure 100: Calculated SNR as a function of user location on the x-axis for different uncertainty radii r_u when y = 25 m. Blue curves represent NFF (focus: x = 25 m, y = 0 m) and orange curves represent LPBS (θ_s = 0).

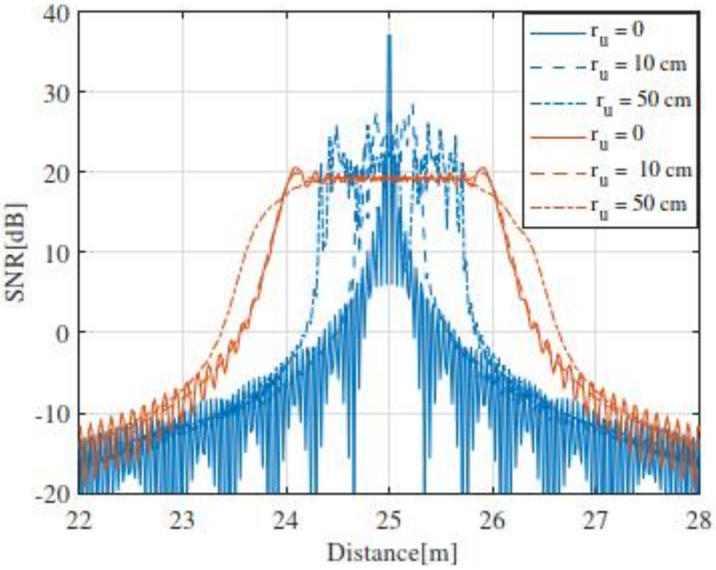

Figure 101: Calculated SNR as a function of user location on the y-axis for different uncertainty radii r_u when y = 25 m. Blue curves represent NFF (focus: x = 25 m, y = 0 m) and orange curves represent LPBS (θ_s = 0).

4.2.2.2 SNR vs. Uncertainty

The simulated SNR figures for NFF and LPBS as a function of uncertainty radius r_u is given in Figure 102. The average SNR is given as the average over M possible user positions inside the disk of radius r_u. For this figure, the NFF is focused on (x, y) position (25 m, 0 m). In general, if user is at the focus point, for lower user uncertainty (r_u) < 10cm, NFF is better as compared to LPBS. At zero uncertainty, the NFF gives the maximum SNR, which reads 38.76 dB. The same for LPBS is 19.56 dB. As the uncertainty increases, the SNR performance is decreasing for both the NFF and LPBS. The SNR level of LPBS antenna array gradually decreases as uncertainty increases, whereas NFF experience a sharp SNR degradation up to about 1 m of uncertainty, then decreases gradually. At 5 m uncertainty the power received by user is 24 dB less in NFF and 6 dB less in LPBS as compared to user at uncertainty 0 m. As compared to

LPBS, NFF antenna array has diminishing gain over the LPBS as uncertainty increases. Power distributions for various uncertainties are further studied below.

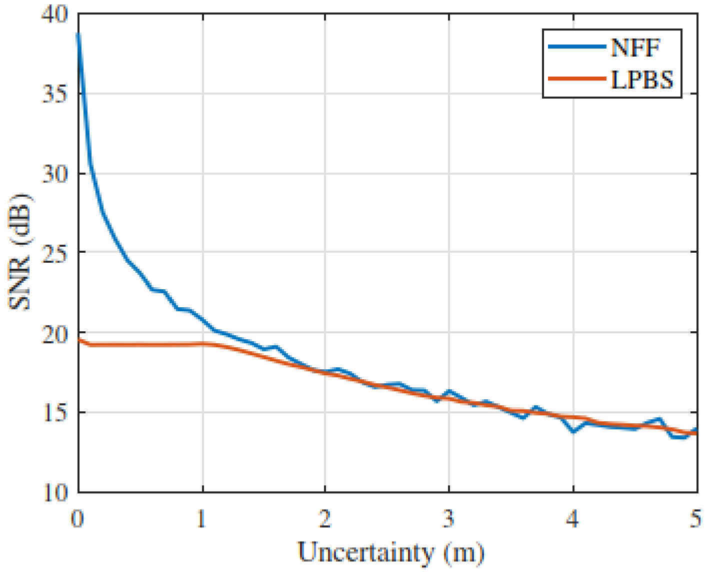

Figure 102: SNR as a function of uncertainty r_u for a single user. Focus equals the observation point (x = 25 m, y = 0 m).

4.2.2.3 Power Distribution with User Position Uncertainty

Figure 103 Figure 104 show the probability density functions (PDFs) of the received power for a user positioned at focus point (25 m, 0 m). Specifically, we consider position uncertainty radii 5 cm, 10 cm, 20 cm, 50 cm, and 1 meter. The distributions are calculated over 50,000 data points. As expected, the NFF outperforms LPBS when there is no uncertainty in the user position. Power distribution of LPBS is spread across relatively close set of received powers. Thus, the variance of the received power is small. As compared to LPBS, NFF power distribution is more spread out. Notice that uncertainty impacts heavily on the performance of NFF antenna array. Here uniform distribution of user position uncertainties is considered, but in many real scenarios user position error is not uniformly distributed. The statistics of the user position are extremely important as NFF suffers from increased losses if there is uncertainty in the exact user position. Indeed, the greater the uncertainty the less there will be gain. As shown in Figure 99, NFF performs excellent when the system is ideal, but if uncertainties are introduced to the system, the traditional linear phase beamforming may be an appealing option. This is also due to simplified channel estimation because of less degrees of freedom required in linear phase beam steering. Therefore, the choice of the beam steering depends on application and amount and accuracy of the information we have for beamforming.

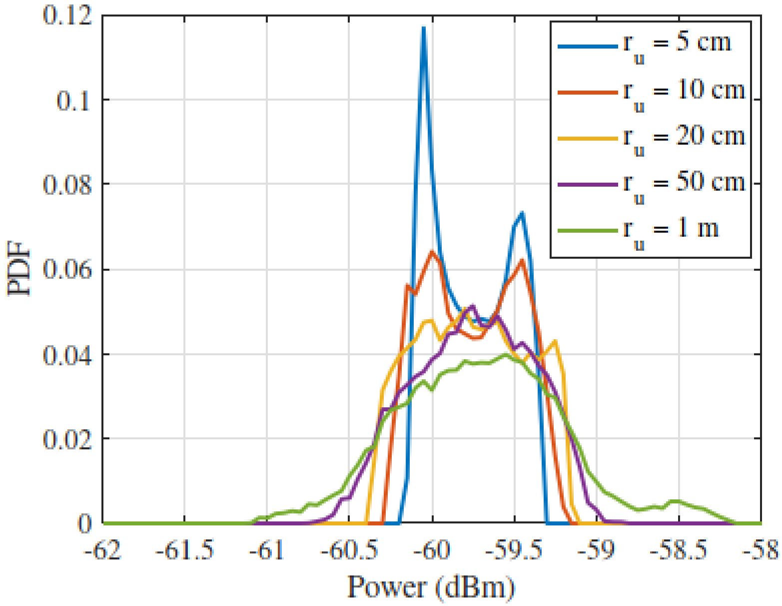

Figure 103: LPBS power distributions for different r_u.

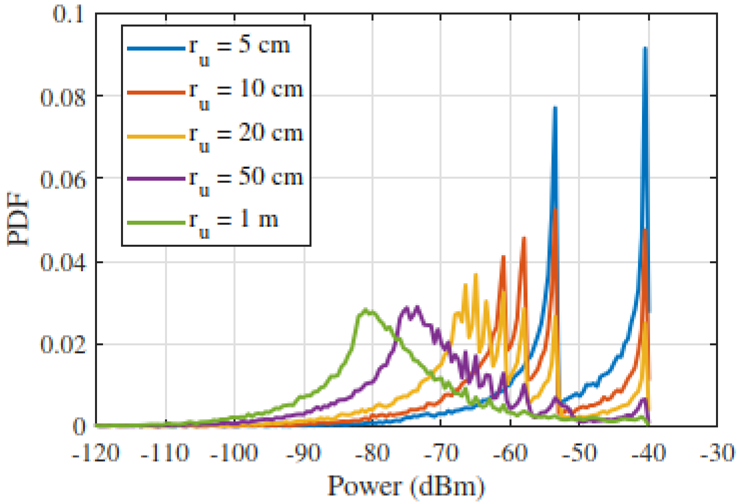

Figure 104: NFF power distributions for different r_u.

4.2.3 Conclusions

We analysed the performance of communications in the near field of a large array in this section. We further analysed the impact of the user position uncertainty on the link performance. We compared two beamsteering methods, LPBS and NFF. The former is usually used in the FF where the relative path lengths from different antenna elements to the Rx are comparable. In the NF, these path lengths vary based on the user position. The NFF aligns the phases at the Rx and gives the maximum achievable antenna gain. Thus, the NF focusing gives superior performance in the NF of the antenna array. Due to focusing, the spot where the maximum gain is at, is very small. This leads to increased losses if there is uncertainty in the user position. This uncertainty may be caused, e.g., by user movement causing the channel estimate to become inaccurate before obtaining the next channel estimate, or by the inaccuracy of the estimate itself. Depending on the depth of the position uncertainty, whereas superior in the ideal case, the NFF can lead to worse performance than the LPBS. However, with moderate uncertainty, the NFF still gives very good performance. The results herein clearly show that the optimal beamforming method is dependent on the accuracy of the position information. Sometimes it may be worth to lose some gain in favour of more robust and consistent beamforming.

Future works continue the work in WP3 by adding RISs into analysis and placing those in the real environments. Potential locations where near field consideration may be highly relevant are indoor locations. The impact of the users being in the NF of a RIS are reported D1.3 of ARIADNE project.

5 Conclusions

The main results derived by the research work presented in this deliverable are summarised for each chapter of the deliverable as follows.

Baseband and RF design and prototypes

The baseband unit (BBU) and the DAC/ADC boards supporting the PtP LOS demonstrator has been presented in detail. The BBU was enhanced to compensate the specific D-band impairments and offers increased spectral efficiency through the introduced polarization multiplexing. The baseband receiver unit was capable of mitigating the D-band specific depolarization effects through a developed XPIC architecture in digital loopback tests. The reported results showcase the high performance of ICOM's DSP-enhanced BBU in the digital loopback regarding the XPI and other impairments.

The practical implementation of frequency-switching at D-band was discussed with respect to the generation of the carrier signal and the needed reference oscillator's signal, e.g., to exploit frequency diversity for reliable and secure transmission at the physical layer. The work must be considered in the context of the overall radio front-end design as reported in D3.1 and D3.2. For proof-of-concept, the hardware was tested by prototype designs that will be employed and further modified for the use in the final outdoor unit of the PtP demonstrator. It was shown, that switching times as low as 5.4 ns can be achieved with the dual-PLL approach with an isolation of close to 50 dB between the individual carriers. All this can be achieved with high spectral purity, low phase noise and low thermal drift after a warm-up time of 5 minutes without oven-control. The bus protocol of the control interface was defined and tested, which will be extended or embedded in the radio control unit of the outdoor unit as part of WP5.

D-band antennas design and prototypes

Detailed design of high gain reflector antennas (HGAs) appropriate for the outdoor long range PtP scenario have been presented. Various horn antennas have been designed as feeders of the proposed HGAs. Optimization of HGAs and detailed realistic designs have been presented that result in a more practical antenna. Additionally, designs of dielectric lens MGAs, appropriate for an indoor scenario which includes NLOS propagation through RIS reflection, have been presented. Sensitivity analysis of the antenna performance on the dielectric lens properties has been conducted as well.

The proposed confocal antenna has been fabricated for proof-of-concept in W-band. The optics of the antenna has been experimentally verified in an anechoic chamber using a passive sub-reflector, emulating one state of the reconfigurable antenna, with promising results. The reconfigurable reflectarray antenna based on liquid crystal materials has been experimentally characterized, and the voltage dependence of the phase extracted in a quasi-optical lab bench setup. The next step will be the integration of the system together with the control circuits that have already been tested without and with loads.

The dynamic control of the phase in reflectarray antennas with dual-polarization using the investigated liquid crystal technology is a very challenging task. The dual-pol concept has been also studied which resulted in the proposition of a novel antenna element. Despite the difference between each set of orthogonal dipoles in both dimension and number, the optimized antenna element can produce the same response for each polarization. A trade-off between phase range and losses allows to have 300° of phase with average losses of 3 dB, at 100 GHz, which is a very promising result at such frequencies, for an element with electronic control and low cost. The obtained results are promising and enables the implementation of a simple proof-of-concept demonstrator.

Finally, in order to improve one of the main drawbacks of the proposed LC-RA technology, namely the large switching times between phase states, we proposed and validated a dynamical model of LC transitions for different excitations beyond the known approximations. This enables a temporal phase control of the unit cell, useful for both reflective and transmissive cells. Even though the effect of the different LC driving excitations on the phase change can be carried out through both measurements and simulations, a generalization in frequency, incident angle, cell designs and LC materials could be cumbersome to do by experimental means. Instead, a simulation tool like the one developed, allows for a fast and precise estimation of control signals to introduce the temporal parameter in the design space of future antennas. For example, this tool allowed us to use an overdriving technique capable of drastically reducing the transition times by orders of magnitude in a simple way, as well as to experimentally prove it for the first time, by using time-controlled excitation signals in LC reflectarray cells.

Metasurfaces design, analysis, and prototypes

In terms of the RIS design and prototyping, we have achieved the goal to develop a design and implementation procedure for anomalous reflectors suitable for the planned indoor demonstrator. For the target frequency bands, we have designed anomalous reflectors, of which theoretically and numerically estimated performance goes well beyond the fundamental bound for conventional phase-gradient metasurfaces. We have considered different designs and discussed their benefits in view of various manufacturing challenges, and finally, found an optimum way for manufacturing. More results will be provided at later stages as part of WP5.

Additionally, we analysed the performance of communications in the near field of a large array. We further analysed the impact of the user position uncertainty on the link performance and compared two beam steering methods, LPBS and NFF. The former is usually used in the far field (FF) where the relative path lengths from different antenna elements to the Rx are comparable. In the near field (NF), these path lengths vary based on the user position. The NFF methods aligns the phases at the Rx and gives the maximum achievable antenna gain. Thus, the NF focusing gives superior performance in the NF of the antenna array. Due to focusing, the spot where the maximum gain found, is very low. This leads to increased losses if there is uncertainty in the user position. This uncertainty may be caused, e.g., by user movement causing the channel estimate to become inaccurate before obtaining the next channel estimate, or by the inaccuracy of the estimate itself. Depending on the depth of the position uncertainty, whereas the NFF is superior in the ideal case, the NFF can lead to worse performance than the LPBS. However, if the uncertainty is moderate, the NFF still gives very good performance. The results herein clearly show that the optimal beamforming method is dependent on the accuracy of the position information. Sometimes it may be worth to lose some gain in favour of more robust and consistent beamforming. Future work will continue the research in WP3 by adding RISs into analysis and placing those in the real environments. Potential locations where near field consideration may be highly relevant are indoor locations. The impact of the users being in the NF of a RIS were reported in D1.3 of ARIADNE project.

6 Bibliography

[1] A. Project, "Deliverable 3.1 - "Report on Baseband and Antenna Concepts," 2020.

[2] F. Zhiming, Z. Fei, X. Liang, S. Yuqiu, W. Lingling and J. Le, "A Method to Shorten the Frequency Hopping Time of Fractional-N Phase-locked Loop," *IEICE Electronics Express,* vol. 18.20210514, 2021.

[3] L. J., F. Tang and H. T., "Development of High Isolation Ping-Pong DDS-PLL Based Frequency Synthesizer for Fast Frequency Hopping Applications," in *Asia-Pacific Microwave Conference (APMC)*, 2018.

[4] D. D. Nicola and S. Ali, Understanding Jitter and Phase Noise: A Circuits and Systems Perspective, Cambridge: Cambridge University Press, 2018.

[5] Y. Fan and Z. Zilic, "Accelerating jitter tolerance qualification for high speed serial interfaces," in *10th International Symposium on Quality Electronic Design*, 2009.

[6] [Online]. Available: https://www.analog.com/media/en/technical-documentation/data-sheets/adrf5020.pdf. [Accessed April 2022].

[7] I. Maestrojuan, M. Goñi and e. a. A. Martinez, "High gain reflector antenna for MBtera H2020 project," in *42nd International Conference on Infrared, Millimeter, and Terahertz Waves (IRMMW-THz)*, Cancun, Mexico, 2017.

[8] K. S. Satish, R. Sudhakar and S. Lotfollah, Handbook of Reflector Antennas and Feed Systems: Volume 1 - Theory and Design of Reflectors, Boston/London: Artach House, 2013.

[9] C. A. Balanis, Antenna theory: analysis and design, John wiley & sons, 2016.

[10] J. L. Volakis, Antenna Engineering Handbook, 4th, Ed., McGraw-Hill, 2007.

[11] R. C. Jorge, B. L. Eduardo and A. F. Carlos, "Compact Beam-Steerable Lens Antenna for 60-GHz Wireless Communications," *IEEE TRANSACTIONS ON ANTENNAS AND PROPAGATION,* vol. 57, no. 10, pp. 2926 - 2933, October 2009.

[12] F. Yang, C. Wu, Y. Zhang, Z. Tian, J. Ouyang and P. Yang, "Dual-band dual-polarization reflectarray design with a large offset feed angle," in *International Conference on Electromagnetics in Advanced Applications (ICEAA)*, Palm Beach, Aruba, 2014.

[13] M.-Y. Zhao, G.-Q. Zhang, X. Lei, J.-M. Wu and J.-Y. Shang, "Design of New Single-Layer Multiple-Resonance Broadband Circularly Polarized Reflectarrays," *IEEE Antennas and Wireless Propagation Letters,* vol. 12, pp. 356-359, 2013.

[14] S. Sasaki, T. Murayama, D. Higashi, H. Deguchi and M. Tsuji, "Reflectarray antenna constructed by arranging double omega-shaped resonant elements with mirror image for circular-polarization conversion," in *International Symposium on Antennas and Propagation (ISAP)*, Phuket, Thailand, 2017.

[15] M. M. Tahseen and A. A. Kishk, "Bandwidth enhancement in Ka-Band circularly polarized reflectarray using stacked cross-bowtie elements," in *17th International Symposium on Antenna Technology and Applied Electromagnetics (ANTEM)*, Montreal, QC, Canada, 2016.

[16] A. Zornoza, J. Encinar and M. Bialkowski, "A double-layer microstrip reflectarray design to obtain Australia and New Zealand footprint," in *IEEE Antennas and Propagation Society International Symposium. Digest. Held in conjunction with: USNC/CNC/URSI North American Radio Sci. Meeting (Cat. No.03CH37450)*, Columbus, OH, USA, 2003.

[17] A. A., "Dual-band single layer microstrip reflectarray using multiresonance double cross elements," in *Asia-Pacific Microwave Conference (APMC)*, New York, USA, 2008.

[18] T. Gregor, W. B. Richard, D. L. Gordon, J. P. Miles and R.-M. Monika, "Speeding up liquid crystal SLMs using overdrive with phase change reduction," *Otpics Express,* vol. 21, no. 2, pp. 1779-1797, 2013.

[19] R. James, F. A. Fernandez, S. E. Day, S. Bulja and D. Mirshekar-Syahkal, "Accurate Modeling for Wideband Characterization of Nematic Liquid Crystals for Microwave Applications," *IEEE Transactions on Microwave Theory and Techniques,* vol. 57, no. 12, pp. 3293-3297, 2009.

[20] P.-P. Gerardo, R. Florencio, J. A. Encinar, M. Barba and e. a. Raymond Dickie, "Accurate and Efficient Modeling to Calculate the Voltage Dependence of Liquid Crystal-Based Reflectarray Cells," *IEEE Transactions on Antennas and Propagation,* vol. 62, no. 5, pp. 2659-2668, 2014.

[21] [Online]. Available: www.comsol.com. [Accessed 30 April 2022].

[22] [Online]. Available: www.cst.com.. [Accessed 30 April 2022].

[23] W. Xuchen, D.-R. Ana and A. T. Sergei, "Independent Control of Multiple Channels in Metasurface Devices," *Physical Review Applied,* vol. 14, no. 2, 2020.

[24] X. Wang, "Surface-impedance engineering for advanced wave transformations," Aalto University, 2020.

[25] W. X., D.-R. Ana, S. A. Viktar and e. al, "Extreme Asymmetry in Metasurfaces via Evanescent Fields Engineering: Angular-Asymmetric Absorption," *Physical Review Letters,* vol. 121, no. 25, 2018.

[26] A. Buffi, P. Nepa and G. Manara, "Design Criteria for Near-Field-Focused Planar Arrays," *IEEE Antennas and Propagation Magazine,* vol. 54, pp. 40-50, 2012.

[27] R. J. Mailloux, Phased array antenna handbook, Artech house, 2017.

[28] J. Sherman, "Properties of focused apertures in the fresnel region," *IRE Transactions on Antennas and Propagation,* vol. 10, pp. 399-408, 1962.

[29] V. R. Gowda, O. Yurduseven, G. Lipworth, T. Zupan, M. S. Reynolds and D. R. Smith, "Wireless Power Transfer in the Radiative Near Field," *IEEE Antennas and Wireless Propagation Letters,* vol. 15, pp. 1865-1868, 2016.

[30] A. Badawi, A. Sebak and L. Shafai, "Array near field focusing," in *IEEE WESCANEX 97 Communications, Power and Computing. Conference Proceedings*, 1997.

[31] H. Kamoda, T. Iwasaki, J. Tsumochi, T. Kuki and O. Hashimoto, "60-GHz Electronically Reconfigurable Large Reflectarray Using Single-Bit Phase Shifters," *IEEE Transactions on Antennas and Propagation,* vol. 59, pp. 2524-2531, 2011.

[32] S. Karimkashi and A. A. Kishk, "Focusing Properties of Fresnel Zone Plate Lens Antennas in the Near-Field Region," *IEEE Transactions on Antennas and Propagation,* vol. 59, pp. 1481-1487, 2011.

[33] M. Bogosanovic and A. G. Williamson, "Microstrip Antenna Array With a Beam Focused in the Near-Field Zone for Application in Noncontact Microwave Industrial Inspection," *IEEE Transactions on Instrumentation and Measurement,* vol. 56, pp. 2186-2195, 2007.

[34] S. Payami and F. Tufvesson, "Channel measurements and analysis for very large array systems at 2.6 GHz," in *2012 6th European Conference on Antennas and Propagation (EUCAP)*, 2012.

[35] R. C. Hansen, "Aperture theory," in *Apertures*, Elsevier, 1964, p. 1–105.

[36] A. F. Molisch, Wireless communications, vol. 34, John Wiley & Sons, 2012.

[37] E. W. Weisstein, "Disk point picking," *[Online] Available : \url https://mathworld.wolfram.com/DiskPointPicking.html,* 2002.